AD-A268 009

ATION PAGE

Form Approved
OMB No 0704-0188

to average 1 hour per response, including the time for reviewing instructions, searching existing data sources, gathering and maintaining the collection of information. Send comments regarding this burden estimate or any other aspect of this collection of information, including suggestions for reducing this burden, to Washington Headquarters Services, Directorate for information Operations and Reports, 1215 Jefferson Davis Highway, Suite 1204, Arlington, VA 22202-4302, and to the Office of Management and Budget, Paperwork Reduction Project (0704-0188), Washington, DC 20503.

| DATE | 3. REPORT TYPE AND DATES COVERED |
|---|---|
| August 1993 | THESIS/DISSERTATION |

**4. TITLE AND SUBTITLE**
Evaluation Of Hybird Reinforcement (Fiber-Reinforced-Plastic Rod with Steel Core)

**5. FUNDING NUMBERS**

**6. AUTHOR(S)**
Capt Markus J. Henneke

**7. PERFORMING ORGANIZATION NAME(S) AND ADDRESS(ES)**
AFIT Student Attending: Pennsylvania State University

**8. PERFORMING ORGANIZATION REPORT NUMBER**
AFIT/CI/CIA- 93-114

**9. SPONSORING / MONITORING AGENCY NAME(S) AND ADDRESS(ES)**
DEPARTMENT OF THE AIR FORCE
AFIT/CI
2950 P STREET
WRIGHT-PATTERSON AFB OH 45433-7765

DTIC
ELECTE
AUG17 1993
S E D

**10. SPONSORING / MONITORING AGENCY REPORT NUMBER**

**11. SUPPLEMENTARY NOTES**

**12a. DISTRIBUTION / AVAILABILITY STATEMENT**
Approved for Public Release IAW 190-1
Distribution Unlimited
MICHAEL M. BRICKER, SMSgt, USAF
Chief Administration

**12b. DISTRIBUTION CODE**

**13. ABSTRACT** *(Maximum 200 words)*

93-19009

93 8 16 079

**14. SUBJECT TERMS**

**15. NUMBER OF PAGES**
158

**16. PRICE CODE**

| 17. SECURITY CLASSIFICATION OF REPORT | 18. SECURITY CLASSIFICATION OF THIS PAGE | 19. SECURITY CLASSIFICATION OF ABSTRACT | 20. LIMITATION OF ABSTRACT |
|---|---|---|---|
| | | | |

Capt. Markus J. Henneke

U.S. Air Force

# EVALUATION OF HYBRID REINFORCEMENT

# (FIBER-REINFORCED-PLASTIC ROD WITH STEEL CORE)

158 Pages

Master of Science

Architectural Engineering

Accesion For
NTIS CRA&I
DTIC TAB
Unannounced
Justification
By
Distribution /
Availability Codes
Dist | Avail and / or Special
A-1

DTIC QUALITY INSPECTED 3

The Pennsylvania State University

Department of Architectural Engineering

The Pennsylvania State University

The Graduate School

College of Engineering

# EVALUATION OF HYBRID REINFORCEMENT

# (FIBER-REINFORCED-PLASTIC ROD WITH STEEL CORE)

A Thesis in

Architectural Engineering

by

Markus J. Henneke

Submitted in Partial Fulfillment
of the Requirements
for the Degree of

Master of Science

August 1993

We approve the thesis of Markus J. Henneke.

Date of Signature

Antonio Nanni — 05/20/93

Antonio Nanni
Associate Professor of Architectural Engineering
Thesis Adviser

Paul A. Seaburg — 5/20/93

Paul A. Seaburg
Professor of Architectural Engineering
Head of the Department of Architectural Engineering

Theodor Krauthammer — 5-20-93

Theodor Krauthammer
Professor of Civil Engineering

# ABSTRACT

The corrosion of concrete reinforcement is a problem that seriously affects structures exposed to harsh environments (parking garages, marine structures, chemical plants, etc.). Currently the most popular method of corrosion protection is epoxy-coating for steel rebars and tendons. As an alternative to epoxy-coating, this project presents an initial evaluation of hybrid reinforcement. Hybrid reinforcement consists of a FRP (fiber-reinforced-plastic) skin with a steel core. The FRP skin (fully-bonded) is made of braided, epoxy-impregnated aramid or vinylon fiber. Besides protecting the steel core from corrosion, the FRP skin provides a structural function. Hybrid reinforcement allows specifying a reinforcement behavior by changing the core-to-skin cross-sectional ratios and by combining different core and skin materials. Uniaxial tensile test results are presented to show the characteristics of different hybrid rods. Results from beams reinforced with hybrid rods are presented to demonstrate the flexural behavior of concrete members reinforced with hybrid rods.

The results from the tensile tests showed that changing the FRP skin material, FRP skin thickness, steel core diameter and steel core strength provided various stress-strain behaviors. The stress-strain curves of the hybrid rods displayed a bi-linear nature due to differences in mechanical properties of the FRP skin and steel core. The tensile tests also demonstrated that the law of mixtures can be used to predict the stress-strain behavior of the hybrid rods.

From the concrete beam tests, it was found that the load deflection curves could be predicted based on the tensile behavior of the hybrid rods and the classical assumptions used in conventionally reinforced concrete analysis. Beams with hybrid rods had fewer cracks which were further spaced than beams with steel reinforcement. Longitudinal cracks developed in beams reinforced with hybrid rods that had a aramid skin. After failure of the FRP skin, the beam was still able to sustain the load resisted by the steel core.

# TABLE OF CONTENTS

Page

LIST OF ILLUSTRATIONS ..... viii

LIST OF TABLES ..... xvi

ACKNOWLEDGMENTS ..... xvii

CHAPTER 1. INTRODUCTION ..... 1

1.1 BACKGROUND ..... 1

1.2 LITERATURE REVIEW ..... 3

1.2.1 Mechanical Properties of FRP Rods ..... 4

1.2.2 Bond Characteristics ..... 5

1.2.3 Application of FRP Rods ..... 6

1.2.4 Durability of FRP Rods ..... 8

1.3 SCOPE AND PURPOSE ..... 9

1.4 JUSTIFICATION ..... 10

CHAPTER 2. FIBER-REINFORCED-PLASTIC CONSTITUENT MATERIALS ..... 11

2.1 ARAMID FIBER ..... 11

2.1.1 Background ..... 11

2.1.2 Physical Properties ..... 12

2.1.3 Mechanical Properties ..... 13

2.1.4 Durability: Behavior in Different Environments ..... 14

2.2 POLYVINYL ALCOHOL FIBER ..... 16

2.2.1 Background ..... 16

2.2.2 Physical Properties ..... 17

2.2.3 Mechanical Properties ..... 18

2.2.4 Durability: Behavior in Different Environments ..... 20

2.3 RESIN ..... 20

2.3.1 Thermoplastic Resins ..... 21

2.3.2 Thermosetting Resins ..... 21

2.4 NOTATION ..... 23

CHAPTER 3. UNIAXIAL TENSILE TESTS ..... 24

3.1 TENSILE TEST SET-UP ..... 24

3.1.1 First Set ..... 24

3.1.2 Second Set ..... 25

3.1.3 Testing ..... 27

3.2 TEST RESULTS AND OBSERVATIONS ..... 29

3.3 DISCUSSION OF RESULTS ..... 34

3.4 CONCLUSIONS ..... 39

CHAPTER 4. REINFORCED CONCRETE BEAM TESTS ..... 41

4.1 CONCRETE BEAM TEST SET-UP ..... 41

4.2 CASTING OF CONCRETE BEAMS ..... 45

4.3 TESTING ..... 47

4.3.1 Equipment ..... 47

4.3.2 Loading Procedure ..... 49

4.4 TEST RESULTS ..... 50

CHAPTER 5. DISCUSSION OF BEAM TESTS ..... 58

5.1 BEAMS WITH VINYLON AND ARAMID HYBRID RODS ..... 58

5.2 BEAMS WITH #5 REBAR AND SMOOTH 13.0 mm ROD ..... 61

5.3 CRACKING PATTERN OF TEST BEAMS ..... 66

5.3.1 Flexural Crack Width ..... 66

5.3.2 Flexural Crack Spacing ..... 69

5.3.3 Longitudinal Cracks ..... 71

5.4 CONCLUSIONS ..... 75

CHAPTER 6. SUMMARY AND RECOMMENDATIONS ..... 78

6.1 SUMMARY ..... 78

6.1.1 Uniaxial Tensile Tests ..... 78

6.1.2 Beam Tests ..... 78

6.2 RECOMMENDATIONS ..... 79

APPENDIX A. UNIAXIAL TENSILE TEST DATA ..... 82

APPENDIX B. BEAM TEST DATA ..... 109

APPENDIX C. SAMPLE CALCULATIONS ..... 143

BIBLIOGRAPHY ..... 155

## LIST OF ILLUSTRATIONS

Figure Page

Figure 1. Diagram of Hybrid Rod ..... 2

Figure 2. Schematic Chemical Degradation of Aramid, Aramid FRP and Steel ..... 15

Figure 3. Granular Fracture of Vinylon ..... 18

Figure 4. Cross-section of Hybrid Rod Anchor ..... 27

Figure 5. Tensile Testing Apparatus ..... 28

Figure 6. Failed Aramid Hybrid Rod ..... 32

Figure 7. Failed Vinylon Hybrid Rod ..... 33

Figure 8. Stress-Strain Curve: K96/9.2 mm/SBPR80 ..... 35

Figure 9. Stress-Strain Curve: Experimental and Theoretical, K96 and V96 with 9.2 mm/SBPR80 Core ..... 36

Figure 10. Load-Strain Curve: K96 and V96 with 9.2 mm/SBPR80 Steel Core ..... 37

Figure 11. Stress-Strain Curve: K96 and V96 with 9.2 mm/SBPR80 Steel Core ..... 38

Figure 12. Load-Strain Curve: Increasing Cross-Section of Vinylon Skin ..... 38

Figure 13. Load-Strain Curve: Increasing Cross-Section of Aramid Skin ..... 39

Figure 14. Reinforcement Configuration ..... 42

Figure 15. Cross-section Diagram of Test Beams ..... 42

Figure 16. Rebar Cage with Hybrid Rod ..... 43

Figure 17. Graph of Concrete Strength ..... 46

Figure 18. Test Equipment Assembly ..... 47
Figure 19. Diagram of Beam Test Setup ..... 48
Figure 20. Beam Setup for Testing ..... 48
Figure 21. Graph of Raw Data for K96/13.0 mm ..... 52
Figure 22. Predicted Shape of Load-Deflection Curve ..... 52
Figure 23. Failed Beam with K96/9.0 mm Hybrid Rod ..... 57
Figure 24. Combined Load-Deflection Curves of Beams with Aramid Hybrid Rods ..... 59
Figure 25. Combined Load-Deflection Curves of Beams with Vinylon Hybrid Rods ..... 59
Figure 26. Failure Crack ..... 60
Figure 27. Experimental and Theoretical Load-Deflection Curves for K64/9.0 mm ..... 62
Figure 28. Experimental and Theoretical Load-Deflection Curves for V64/9.0 mm ..... 62
Figure 29. Load-Deflection Curves for Beams #5 Rebar ..... 63
Figure 30. Load-Deflection Curve for Smooth 13.0 mm Rod ..... 65
Figure 31. Failed Anchorage, Smooth 13.0 mm Rod ..... 65
Figure 32. Bond Stress vs. Slip ..... 70
Figure 33. Photo of Longitudinal Cracks ..... 72
Figure 34. Two Classical Bond Failure Modes ..... 74
Figure 35. Concrete Section ..... 75
Figure A1. Photo K48/9.0 mm/SR24 ..... 83
Figure A2. Photo K96/9.0 /SR24 ..... 83
Figure A3. Photo K96/13.0 mm/SR24 ..... 84
Figure A4. K64/13.0 mm/SBPR80 ..... 84

Figure A5. Photo K64/9.2 mm/SBPR80 ..... 85

Figure A6. Photo K96/9.2 mm/SBPR80 ..... 85

Figure A7. Photo V48/9.0 mm/SR24 ..... 86

Figure A8. Photo V64/9.0 mm/SR24 ..... 86

Figure A9. Photo V64/9.0 mm/SR24 ..... 87

Figure A10. Photo V96/9.2 mm/SBPR80..... 87

Figure A11. Load-Strain Data for K32/3.0 mm (Mild Strength Steel)..... 88

Figure A12. Stress-Strain Curve K32/3.0 mm (Mild Strength Steel)..... 88

Figure A13. Load-Strain Data: K32/4.0 mm (Mild Strength Steel)..... 89

Figure A14. Stress-Strain Curve: K32/4.0 mm (Mild Strength Steel)..... 89

Figure A15. Load-Strain Data: K32/6.0 mm (Mild Strength Steel)..... 90

Figure A16. Stress-Strain Curve: K32/6.0 mm (Mild Strength Steel)..... 90

Figure A17. Load-Strain Data: K32/6.0 mm Threaded (Mild Strength Steel)..... 91

Figure A18. Stress-Strain Curve: K32/6.0 mm Threaded (Mild Strength Steel)..... 91

Figure A19. Load-Strain Data: K64/6.0 mm/PC Wire Core..... 92

Figure A20. Stress-Strain Curve: K64/6.0 mm/PC Wire Core ..... 92

Figure A21. Load-Strain Data: K64/9.3 mm/PC Wire Core..... 93

Figure A22. Stress-Strain Curve: K64/9.3 mm/PC Wire Core ..... 93

Figure A23. Load-Strain Data: K48/9.0 mm/SR24 ..... 94

Figure A24. Stress-Strain Curve: K48/9.0 mm/SR24 ..... 94

Figure A25. Load-Strain Data: K64/9.0 mm/SR24 ..... 95

Figure A26. Stress-Strain Curve: K64/9.0 mm/SR24 ..... 95

Figure A27. Load-Strain Data: K96/9.0 mm/SR24 ..... 96

Figure A28. Stress-Strain Curve: K96/9.0 mm/SR24 ..... 96

Figure A29. Load-Strain Data: V48/9.0 mm/SR24 ..... 97

Figure A30. Stress-Strain Curve: V48/9.0 mm/SR24 ..... 97

Figure A31. Load-Strain Data: V64/9.0 mm/SR24 ..... 98

Figure A32. Stress-Strain Curve: V64/9.0 mm/SR24 ..... 98

Figure A33. Load-Strain Data: V96/9.0 mm/SR24 ..... 99

Figure A34. Stress-Strain Curve: V96/9.0 mm/SR24 ..... 99

Figure A35. Load-Strain Data: K96/13.0 mm/SR24 ..... 100

Figure A36. Stress-Strain Curve: K96/13.0 mm/SR24 ..... 100

Figure A37. Load-Strain Data: K64/9.2 mm/SBPR80 ..... 101

Figure A38. Stress-Strain Curve: K64/9.2 mm/SBPR80 ..... 101

Figure A39. Load-Strain Data: K96/9.2 mm/SBPR80 ..... 102

Figure A40. Stress-Strain Curve: K96/9.2 mm/SBPR80 ..... 102

Figure A41. Load-Strain Data: V96/9.2 mm/SBPR80 ..... 103

Figure A42. Stress-Strain Curve: V96/9.2 mm/SBPR80 ..... 103

Figure A43. Load-Strain Data: K96/13.0 mm/SBPR80 ..... 104

Figure A44. Stress-Strain Curve: K96/13.0 mm/SBPR80 ..... 104

Figure A45. Load-Strain Data: 9.0 mm/SR24 Steel Core ..... 105

Figure A46. Stress-Strain Curve: 9.0 mm/SR24 Steel Core ..... 105

Figure A47. Load-Strain Data: 9.2 mm/SBPR80 Steel Core ..... 106

Figure A48. Stress-Strain Curve: 9.2 mm/SBPR80 Steel Core ..... 106

Figure A49. Load-Strain Data: 13.0 mm/SR24 Steel Core.....107

Figure A50. Stress-Strain Curve: 13.0 mm/SR24 Steel Core.....107

Figure A51. Load-Strain Data: 13.0 mm/SBPR80 Steel Core.....108

Figure A52. Stress-Strain Curve: 13.0 mm/SBPR80 Steel Core.....108

Figure B1. Hybrid Rod Anchor.....110

Figure B2. Hybrid Rod Anchor.....110

Figure B3. Hybrid Rod Anchor.....111

Figure B4. Rebar Cage with Hybrid Rod.....111

Figure B5. Rebar Cage with Conventional Rebar.....112

Figure B6. Closeup of Conventional Rebar Anchorage.....112

Figure B7. Rebar Cage with Smooth 13.0 mm Rod.....113

Figure B8. Closeup of Smooth Rod Anchorage.....113

Figure B9. Forms for Test Beams.....114

Figure B10. Large Form and Rebar Cages.....114

Figure B11. Small Form and Rebar Cages.....115

Figure B12. Placement and Vibration of Concrete.....116

Figure B13. Placement of Concrete.....116

Figure B14. Curing of Test Beams.....117

Figure B15. Test Beam #1 - #5 Rebar.....117

Figure B16. Test Beam #3 - K48/9.0 mm/SR24.....118

Figure B17. Test Beam #3 - Failure Crack.....118

Figure B18. Test Beams #3, #4 and #5.....119

Figure B19. Test Beam #10 - Smooth 13.0 mm Rod.....119

Figure B20. Test Beam #1 - #5 Rebar, Flexural Cracks.....120

Figure B21. Load-Deflection Curve: Test Beam #1 - #5 Rebar.....121

Figure B22. Load-Deflection Curve: Test Beam #3 - K48/
9.0 mm/SR24 ..... 121
Figure B23. Load-Deflection Curve: Test Beam #4 - K64/
9.0 mm/SR24 ..... 122
Figure B24. Load-Deflection Curve: Test Beam #5 - V48/
9.0 mm/SR24 ..... 122
Figure B25. Load-Deflection Curve: Test Beam #6 - K96/
9.0 mm/SR24 ..... 123
Figure B26. Load-Deflection Curve: Test Beam #7 - K96/
13.0 mm/SR24 ..... 123
Figure B27. Load-Deflection Curve: Test Beam #8 - V64/
9.0 mm/24 ..... 124
Figure B28. Load-Deflection Curve: Test Beam #9 - V96/
9.0 mm/SR24 ..... 124
Figure B29. Load-Deflection Curve: Test Beam #10 - Smooth
13.0 mm Rod ..... 125
Figure B30. Load-Deflection Curve: Test Beam #11 - K96/
9.0 mm/SR24 ..... 125
Figure B31. Load-Deflection Curve: Test Beam #12 - V96/
9.0 mm/SR24 ..... 126
Figure B32. Load-Deflection Curve: Test Beam #13 - K96/
13.0 mm/SR24 ..... 126
Figure B33. Load-Deflection Curve: Test Beam #14 - K48/
9.0 mm/SR24 ..... 127
Figure B34. Load-Deflection Curve: Test Beam #15 - V64/
9.0 mm/SR24 ..... 127

Figure B35. Load-Deflection Curve: Test Beam #16 - K64/
9.0 mm/SR24 ..... 128
Figure B36. Load-Deflection Curve: Test Beam #17 - V48/
9.0 mm/SR24 ..... 128
Figure B37. Load-Deflection Curve: Test Beam #18 - #5 Rebar ..... 129
Figure B38. Experimental and Theoretical Load-Deflection Curves for
Beams with K48/9.0 mm Hybrid Rod ..... 130
Figure B39. Experimental and Theoretical Load-Deflection Curves for
Beams with K96/9.0 mm Hybrid Rod ..... 130
Figure B40. Experimental and Theoretical Load-Deflection Curves for
Beams with K96/13.0 mm Hybrid Rod ..... 131
Figure B41. Experimental and Theoretical Load-Deflection Curves for
Beams with V48/9.0 mm Hybrid Rod ..... 131
Figure B42. Experimental and Theoretical Load-Deflection Curves for
Beams with V96/9.0 mm Hybrid Rod ..... 132
Figure B43. Sample of XY Plotter Data ..... 133
Figure B44. Crack Pattern Tracing: Test Beam #1 - #5 rebar ..... 134
Figure B45. Crack Pattern Tracing: Test Beam #3 - K48/9.0 mm
Hybrid Rod ..... 134
Figure B46. Crack Pattern Tracing: Test Beam #4 - K64/9.0 mm
Hybrid Rod ..... 135
Figure B47. Crack Pattern Tracing: Test Beam #5 - V48/9.0 mm
Hybrid Rod ..... 135
Figure B48. Crack Pattern Tracing: Test Beam #6 - K96/9.0 mm
Hybrid Rod ..... 136

Figure B49. Crack Pattern Tracing: Test Beam #7 - K96/13.0 mm Hybrid Rod.....136

Figure B50. Crack Pattern Tracing: Test Beam # 8 - V64/9.0 mm Hybrid Rod.....137

Figure B51. Crack Pattern Tracing: Test Beam #9 - V96/9.0 mm Hybrid Rod.....137

Figure B52. Crack Pattern Tracing: Test Beam #10 - Smooth 13.0 mm rod.....138

Figure B53. Crack Pattern Tracing: Test Beam #11 - K96/9.0 mm Hybrid Rod.....138

Figure B54. Crack Pattern Tracing: Test Beam #12 - V96/9.0 mm Hybrid Rod.....139

Figure B55. Crack Pattern Tracing: Test Beam # 13 - K96/9.0 mm Hybrid Rod.....139

Figure B56. Crack Pattern Tracing: Test Beam #14 - K48/9.0 mm Hybrid Rod.....140

Figure B57. Crack Pattern Tracing: Test Beam #15 - V64/9.0 mm Hybrid Rod.....140

Figure B58. Crack Pattern Tracing: Test Beam #16 - K64/9.0 mm Hybrid Rod.....141

Figure B59. Crack Pattern Tracing: Test Beam #17 - V48/9.0 mm Hybrid Rod.....141

Figure B60. Crack Pattern Tracing: Test Beam #18 - #5 Rebar.....142

# LIST OF TABLES

Table Page

Table 1. Density and Coefficient of Thermal Expansion in the Longitudinal and Transverse Directions ..... 13

Table 2. Typical Fiber Properties ..... 13

Table 3. Properties of Vinylon ..... 19

Table 4. Epoxy Resin Properties ..... 22

Table 5. Areas of FRP Skin ..... 23

Table 6. Combinations of Hybrid Rods (Second Set) ..... 26

Table 7. Tensile Properties of Braided FRP Material ..... 26

Table 8. Tensile Test Results for First Set of Hybrid Rods ..... 31

Table 9. Tensile Test Results for Second Set of Hybrid Rods ..... 31

Table 10. Loading and Unloading Cycles ..... 49

Table 11. Experimental and Theoretical Results ..... 54

Table 12. Summary of Crack Patterns ..... 56

Table 13. Theoretical and Experimental Crack Spacing ..... 71

## ACKNOWLEDGMENTS

I would like to thank the following people:

U.S. Air Force for giving me the opportunity to pursue my Master's Degree.

Professor Antonio Nanni for his help and enthusiasm in this project.

The National Science Foundation (NSF) and Mitsui Construction Co. for their funding and support.

Jeremy for all of his help with the beam tests.

My fellow graduate students, Mike, Keith and Nick, for their help and support.

Finally, to my wife, Stephani, whose encouragement and support kept me going through the long days.

# CHAPTER 1

# INTRODUCTION

## 1.1 BACKGROUND

One of the main drawbacks of reinforced and prestressed concrete is the susceptibility of the reinforcement to corrosion. In order to inhibit/eliminate reinforcement corrosion, several active and passive reinforcement protection methods have been developed and evaluated in recent years (Pfeifer et al 1991). These include such methods as sealers, membranes, dense concrete toppings and epoxy-coating. The most popular of these methods has been the epoxy-coated rebars and prestressing tendons.

Recently there has been debate on the effectiveness of epoxy coated rebars for protection. A study by Rasheeduzzafar et al. (1992), found that in high chloride concrete, the epoxy-coated rebars showed significant amounts of corrosion on the steel under the coating. This suggests that epoxy-coatings may have a finite tolerance limit for chlorides.

As an alternative to conventional and epoxy-coated steel reinforcement for reinforced concrete and prestressed concrete members, new reinforcing materials, generally identified as fiber-reinforced-plastic (FRP) composites, have been of increasing interest in the construction

industry. FRP reinforcement consists of glass, aramid, carbon or other synthetic fibers embedded in thermosetting (harden upon application of heat or catalyst and cannot reliquify) or thermoplastic (harden upon cooling and can reliquify) matrix (Iyer and Sen 1991). The physico-mechanical properties of FRP reinforcement are substantially different from that of conventional steel (i.e., elastic up to failure, high-strength, low-modulus).

A new idea has developed to combine FRP and steel in what can be termed hybrid reinforcement. This idea has two important implications: first, it can provide an economically-feasible and more effective method to protect steel reinforcement from corrosion; and, second, it can lead the way for a gradual introduction of FRP reinforcement by using the steel component for ductility. Figure 1 is a diagram showing a section of a hybrid rod. It is clear that the thickness of the FRP skin is substantial and could provide good protection of the steel core.

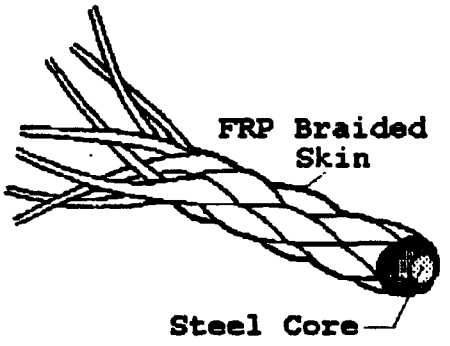


Figure 1. Diagram of Hybrid Rod

With a fiber braiding technique, resin-impregnated yarns of any suitable continuous fiber material (glass, aramid, carbon, etc.) can be used to fully encase a steel wire core, see Figure 1. Steel core and FRP skin are fully bonded by resin impregnating the fiber yarns. Different steel-to-FRP cross-sectional area ratios, as well as steel-grade and fiber type, can be used to allow for different performances of the hybrid reinforcement.

The braiding process provides a number of advantages over conventional pultrusion process FRP rods. First, conventional pultrusion limits the diameter of the rods which can be used for practical applications, while braiding allows almost unlimited diameter. Pultruded rods also require additional processing to improve the bond between its smooth surface and the concrete. The braiding process enhances the bond capacity of the rod by the protrusions and depressions formed on the surface. Finally, the braiding provides an improved stress distribution to all fibers in the cross-section.

## 1.2 LITERATURE REVIEW

In the last 20 years, the interest in the use of advanced fiber composite materials (ACM) in construction has increased substantially. Europe and Japan have been leaders in this area for years, and are continuing their efforts to discover new uses and manufacturing techniques for FRP material.

### 1.2.1 Mechanical Properties of FRP Rods

Before FRP rods can be used in reinforced or prestressed applications, the mechanical properties, such as, stress-strain behavior and bond performance of the different types of FRP rods, need to be understood. A number of researchers have conducted tests on different FRP rods to determine the physical and mechanical properties of FRP rods. Nanni et al. (1992c), Mukae et al. (1993), Pleimann (1991), Yamasaki et al. (1993), Uomoto et al. (1993), Chaallal and Benmokrane (1992), and Porter and Barnes (1991) have all done studies on the properties of FRP rods with different fibers (e.g., aramid, carbon, fiberglass and vinylon). In all studies, it was found that the FRP rods displayed a linear elastic behavior up to failure and that the modulus of elasticity of FRP rods is less than that of steel. The elastic modulus is dependent on fiber type and the volume percentages of the constituent materials (matrix and fiber).

Of interest to this research project is the work done by Nanni et al. (1992c) on the tensile properties of braided FRP rods. The data from this research is used as the material properties for the FRP skin of the hybrid rods. These authors reported on the static tensile properties of braided epoxy-impregnated FRP rods made with glass, aramid and polyvinyl alcohol fibers. The focus of the research program was to determine stress-strain curve shape, elastic modulus, ultimate strength, and Poisson's ratio and ultimate elongation in the longitudinal direction. They determined that braided rods can be considered linear elastic and that, under optimal conditions, strength and rigidity are approximately 80% of that derived on the basis of constituent material properties. It

was also found that the ultimate strength is dependent on the diameter of the rod, and that Poisson's ratio can be affected by rod size as well as manufacturing, depending on fiber type.

### 1.2.2 Bond Characteristics

To replace steel rebars, the bond performance of FRP rods is very important. Larralde and Silva (1990), Daniali (1990), Mashima and Iwamoto (1993), Makitani et al. (1993), Burgoyne (1993), Kanakubo et al. (1993), and Tao et al. (1992) have all done studies on bond performance of different FRP rods. In all cases it was found that the bond strength of FRP rod is less than that of conventional steel. Studies found that in order to fully utilize the FRP rod strength, the embeddment length of a FRP rod must be greater than that of a steel rod.

Larralde and Silva (1990) found that to fully utilize the tensile strength of fiberglass reinforced-plastic (FRP) rebars in reinforced concrete and to avoid extreme cracking or even failure, the bond between the rebar and the concrete has to be large enough for the rebar to develop its ultimate tensile strength. Because of differing material and physical properties between steel rebars and FRP rebars, normal design guidelines for anchorage of steel cannot be used directly in the anchorage design of FRP rebars. In general, the embedded lengths of the rebars were much shorter than the values specified by ACI Code 318-89 for steel rebars.

For prestressed concrete, Burgoyne (1993) suggests that FRP rods should be unbonded due to the susceptibility of the FRP rod to tensile failure. In a reinforced concrete application it is unlikely that a fiber

failure would occur. But in a prestressed concrete, the prestressing absorbs much of the fiber strain capacity, leaving the tendon very sensitive to high strains in the vicinity of a crack.

To improve bond, research has shown that FRP rod surface preparation is the paramount factor. Yamasaki et al. (1993) determined that the initial slip bond stress and maximum bond stress is more dependent on the surface shape than kinds of fiber. Faza and GangaRao (1991) and Makitani et al. (1993) have done work with sand coated rods and have shown that it significantly increases bond performance.

### 1.2.3 Application of FRP Rods

The use of FRP rods is divided into two areas, reinforced concrete (RC) and prestressed concrete (PC). In RC applications, researchers are studying the effect the lower modulus of elasticity of the FRP rods has on deflection and cracking of a concrete member. Also, since the FRP rods are considered linearly elastic up to failure and have tensile strengths significantly greater, how does that affect the design procedures.

Saadatmanesh and Ehsani (1989) did work with GFRP rods in concrete beams to determine behavior in both flexure and shear. They found that the GFRP rods can be used successfully as a concrete reinforcement and that the response to the materials under load can be predicted using analytical methods likely used by engineers.

Faza and GangaRao (1991) did work with glass FRP rods in varying concrete strengths. They suggest that, because of the high

tensile strength of FRP rods, high strength concrete would allow better utilization of FRP rods. Their study found significant gains in moment capacity are obtained when concrete strength is increased.

The design of RC members using FRP rods has been addressed by a number of different researchers. Larralde et al. (1989) conducted laboratory tests on concrete beams reinforced with glass FRP rebars, alone and, in combination with steel rebars were presented. They found that the calculated ultimate loads differed from the experimental loads.

In a paper by Nanni (1992a), it is suggested that flexural design for FRP reinforced concrete members may use either the ultimate strength method or the working stress method. It is contended at this stage of development, the working stress method may be better suited to FRP-reinforced concrete members. The reason for this is the predicted ultimate moment capacity represents a highly variable state only attainable at a high level of deformation and crack opening, and strictly dependent on concrete ultimate strain. Nanni also suggests that since FRP reinforcement does not yield, there should be an explicit provision that failure be controlled by concrete crushing as opposed to reinforcement rupture, and that deflection control may become as important as flexural strength for the design of FRP-reinforced concrete.

The use of FRP rods in prestressing or post-tensioning applications is receiving more emphasis than in RC applications. The reason for this, is the high tensile strength characteristics of FRP rods is better utilized in prestress or post-tensioning applications. As with RC applications, the mechanical and bond behavior of FRP elements has

been the major area of research. Gerritse and Werner (1991), Rostasy (1993), Kaci (1992), Noritake et al. (1993), Reinold de Sitter and Vonk (1993), Nanni et al. (1992d), and Iyer and Khubchandani (1992) have all done work on prestressing FRP properties and bond performance. Important findings are that relaxation is more or less independent of the applied stress level, bond is improved with rod surface preparation, and permanent end special anchorage is needed due to low transverse strength of FRP rods.

### 1.2.4 Durability of FRP Rods

The main purpose for the use of FRP reinforcement is its resistance to corrosion. While there is no question that its corrosion resistance is greater than of steel in certain environments, information is lacking on the long term durability of FRP reinforcement. Nanni et al. (1992c) did work with braided aramid rods and found that strength retention in an alkali solution was satisfactory for non-pretensioned rods. Katawaki et al. (1992) conducted actual exposure durability tests on carbon, aramid, glass and vinylon fibers in a marine environment. The tests found deterioration was nonexistent or negligible in the carbon and aramid fibers, but cracks occurred in the glass fibers and surface deterioration started in the vinylon.

For prestressed FRP rods the main concern is stress rupture. Budelman and Rostasy (1993) found that at high tensile stress, FRP elements exhibit a creep rupture phenomenon. It is suggested that for FRP elements, the stress rupture (stress corrosion) behavior is

influenced by the micro-environment around the element and the type of fiber and matrix used .

## 1.3 SCOPE AND PURPOSE

The main purpose of this study is an initial investigation of the behavioral characteristics of hybrid reinforcement and its feasibility for use in concrete structures susceptible to reinforcement corrosion. To determine these characteristics, a two phase experimental program is employed. This program consists of uniaxial tensile tests (Phase I) and flexural testing of concrete beams reinforced with hybrid rods (Phase II). The hybrid rods vary with respect to material type, skin thickness, steel core strength, and steel core diameter. This research project did not include an evaluation of the durability of hybrid rods.

In Phase I, destructive uniaxial tensile tests are conducted on the hybrid rods to develop stress-strain relationships. These stress-strain relationships are used to determine elastic modulus, ultimate strength and ultimate elongation. An understanding of these properties is very important in predicting the behavior of reinforced concrete members using hybrid reinforcement (at least for cases that are not temperature-, time-, load repetition-, or load rate-dependent). The experimental stress-strain curves are then compared to theoretical stress-strain curves which are developed from the individual material properties and the law of mixtures (e.g., $E_{Hybrid} = V_{FRP}*E_{FRP} + V_{Core}*E_{Core}$, where V is the volume percentage of the component).

Phase II of the study consists of evaluating the behavior of the hybrid rods in a concrete structure, and investigating the failure modes and load-deflection curves. In addition, analytical calculations will be done to determine if load-deflection behavior of a hybrid reinforced beam can be predicted from hybrid rod tensile test stress-strain data. This is accomplished by constructing hybrid reinforced concrete beams and testing them in flexure to develop load-deflection curves.

## 1.4 JUSTIFICATION

The justification for this project is that this type of reinforcement has never been tested before. With the current problems in reinforcement corrosion affecting a large portion of the infrastructure, there is an increasing need for a concrete reinforcement that does not corrode. The successful development of an alternative reinforcement for reinforced and prestressed concrete members can result in more efficient and durable structures.

The cost of aramid FRP rods is comparable to carbon based rods, but higher than glass FRP rods, which in turn are more expensive than steel. It is estimated that initial construction costs may be higher when FRP rods or prestressing tendons are used instead of conventional steel tendons, but in special applications where non-magnetic and non-electrical conductivity is required, the extra cost may be warranted. If the life cycle costs of construction are considered, the use of FRP reinforcement should prove more economical.

# CHAPTER 2

# FIBER-REINFORCED-PLASTIC CONSTITUENT MATERIALS

## 2.1 ARAMID FIBER

### 2.1.1 Background

Aramid fibers were the first organic fibers to be used as a reinforcement in advanced composites due to their high tensile modulus and strength (ASM International 1989, 54-57). They were first introduced in the 1960s by E.I. Du Pont de Nemours & Company, Inc. (U.S.A.), under the trade name Kevlar. Recently, other manufactures have introduced aramid fibers, such as, Enka Corporation (Netherlands), making Twaron fibers, and Teijin (Japan) producing HM-50 and Technora fibers (ASM international 1989, 54-57). Aramid fibers may be produced in different grades, such as, Kevlar 29, Kevlar 49, Kevlar 149. The different grades vary with respect to strength and elastic modulus. For example, Kevlar 29 has a high toughness as opposed to a Kevlar 149 which has a very high elastic modulus.

The chemical composition of aramid fiber is poly para-phenyleneterephthalamide. This fiber is known as PPD-T because it is made from the condensation reaction of para-phenylene diamine and trephthaloyl chloride (ASM International 1989, 54-57). The aromatic ring structure contributes to high thermal stability, while the para

configuration leads to stiff, rigid molecules that contribute high strength and high modulus. Aramid fibers belong to a class of materials known as liquid crystalline polymers. Since these polymers are very rigid and rodlike, they can connect in solution to form ordered domains in parallel arrays (Flory 1984). This is in contrast to conventional flexible polymers, which when placed in solution become bent and entangled, forming random coils. The aramid fibers are produced when the PPD-T solutions are extruded through a spinneret (a small metal plate or cap with fine holes through which a chemical solution is forced) and drawn through an air gap. During fiber manufacture, the liquid crystalline domains can orient and align in the direction of flow (ASM International 1989, 54-57). With aramid, there is an exceptional degree of alignment of long, straight polymer chains parallel to the fiber axis.

### 2.1.2 Physical Properties

Aramid fiber is anisotropic and gives higher strength and modulus in the longitudinal direction than in the transverse direction. It has a low density (1.39 to 1.47 $g/cm^3$), as opposed to steel which has a density over 5 times that (7.85 $g/cm^3$). Table 1 gives the density and the coefficient of thermal expansion in the transverse ($\alpha_t$) and longitudinal ($\alpha_l$) directions for different grades of currently available aramid fibers.

The electrical conductivity of aramid fiber is low. Therefore, aramid FRP composites behave as electrical insulators, making them good for applications where electromagnetic neutrality is required.

Table 1. Density and Coefficient of Thermal Expansion in the Longitudinal and Transverse Directions

| | Density $g/cm^3$ | $\alpha_t$ $(10^{-6}/^oC)$ | $\alpha_l$ $10^{-6}/^oC$ |
|---|---|---|---|
| Kevlar 29 | 1.44 | 60 | -2 |
| Kevlar 49 | 1.44 | 60 | -2 |
| Kevlar 149 | 1.47 | 60 | -2 |
| Twaron | 1.44 | -- | -- |
| Twaron HM | 1.45 | -- | -2 |
| HM-50 | 1.39 | -- | -- |
| Technora | 1.39 | -- | -- |

2.1.3 Mechanical Properties

Typical fiber properties are given in Table 2 for different makes and grades of aramid fibers.

Table 2. Typical Fiber Properties (ASM International 1989, 54-57)

| | Initial Modulus (GPa) | Secant Modulus at 1% Elongation (GPa) | Tensile Strength (MPa) | Ultimate Elongation (%) |
|---|---|---|---|---|
| Kevlar 29 | 62 | 62 | 2900 | 3.8 |
| Kevlar 49 | 114 | 117 | 2900 | 2.4 |
| Kevlar 149 | 146 | 160 | 2410 | 1.4-1.5 |
| Twaron | 80 | 80 | 2775 | 3.3 |
| Twaron HM | 125 | -- | 3150 | 2.0 |
| HM-50 | 81 | -- | 3100 | 4.4 |
| Technora | 72 | -- | 3150 | 4.4 |

The aramid fibers in tension respond almost linearly elastic up to failure. But in compression, the fibers exhibit nonlinear, ductile behavior. Because of the behavior in compression, the use of aramid

fibers in applications that are subject to high compressive strain or flexure loads is limited (ASM International 1989, 54-57).

Creep of non-impregnated aramid strands is slightly higher than that of prestressing steel wire. From tests done by Gerritse and Schurhoff (1986), a creep of less than 0.002 m/m is expected after 100 years. Elongation seems to be nearly linear on a log time scale in the stress ratio (stress/ultimate strength) range between 0.25 and 0.5. Elevated temperatures and alkaline solutions raise the elongation percentage slightly.

### 2.1.4 Durability: Behavior in Different Environments

Aramid fibers show a good resistance to chemical attack but can be chemically degraded by strong acids and bases (Gerritse 1990). Figure 2 is a schematic representation showing the degradation rate at different pH values for aramid FRP, aramid fiber and steel. From Figure 2, it is apparent that the resin matrix significantly improves the chemical resistance of a FRP element, over individual fibers.

The failure mode of aramid fibers is through the development of long axial splits in the individual filaments. According to Hearle et al. (1989, 56):

> Axial splits are caused by any discontinuity or defect, either on the surface of the fibre or internally, this will give rise to a shear stress. As the load on the fibre is increased, the shear stress rises, eventually overcoming the transverse cohesive forces and causing an axial crack to form. If the crack is slightly off axis, it will eventually cross the fibre and lead to rupture. Failure occurs in this way because even a small shear stress will overcome the weak intermolecular bonds between the polymer molecules before the large tensile stress breaks the covalent bonds within the chain molecules. The difference may be accentuated by structural discontinuities.

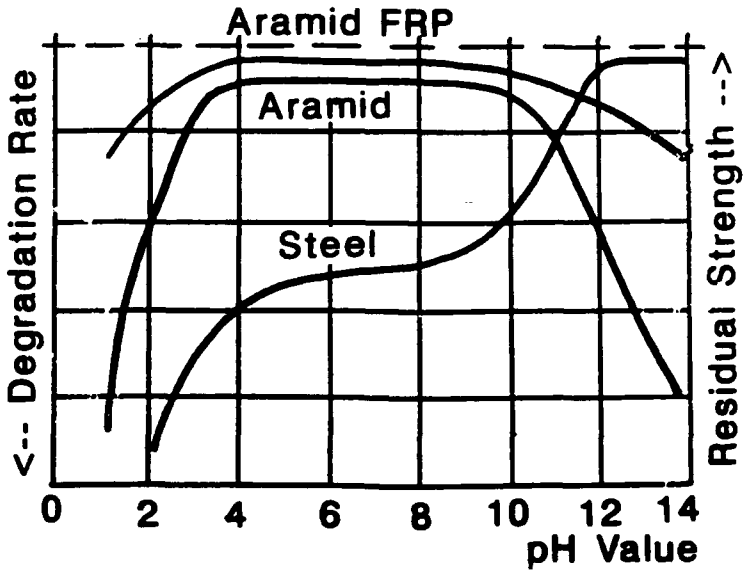


Figure 2. Schematic Chemical Degradation of Aramid, Aramid FRP and Steel (Gerritse 1990)

This is important since axial split type failures tend to be sudden and without warning.

The tensile properties of aramid fibers decrease less than 5% due to moisture (ASM International 1989, 54-57). The equilibrium moisture content of aramid fibers is determined by the relative humidity. Moisture regain at 22 $^{o}$C and 55% relative humidity ranges from 1.0% to 4.8%. The long term effects of fiber moisture regain in FRP elements has been addressed by few researchers (Nanni et al. 1992b). More research is needed to adequately understand the moisture effects.

The aromatic chemical structure of aramid imparts a high degree of thermal stability. Fibers from PPD-T do not have a literal melting point or glass transition temperature ($T_g$) (estimated at $\geq$375 $^{o}$C), as normally observed with other synthetic polymers. They decompose in air at 425 $^{o}$C and are inherently flame resistant (oxygen index of 0.29). They have utility over a broad temperature range of about -200 to 200 $^{o}$C, but are not generally used long-term at temperatures above 150 $^{o}$C because of oxidation (ASM International 1989, 54-57).

Ultraviolet radiation can degrade aramid fibers. The degree of degradation depends on the material thickness because aramid is self-screening, meaning, the outer layers of aramid fibers will degrade but the ultraviolet radiation cannot penetrate past these degraded layers

## 2.2 POLYVINYL ALCOHOL FIBER

### 2.2.1 Background

Polyvinyl Alcohol (PVA) was discovered in the early 1900's. Commercial production of PVA fibers started in 1950 in Japan for use in the textile industry (Sakurada 1985, 5-6). PVA was given the trade name "vinylon" in Japan and "vinal" in the U.S. (from here on, Polyvinyl Alcohol will be referred to as vinylon). Today, vinylon fibers have limited use in the textile industry with their main use being industrial applications.

Vinylon is produced from the basic ingredients of ethylene, acetic acid and oxygen. These three chemicals are synthesized to produced vinyl acetate, which is in turn polymerized by heat in a methanol

solution to produce polyvinyl acetate methanol. A small amount of alkali is then added to the solution and vinylon is precipitated out. The fibers are produced by either a wet spinning process or a dry spinning process. Tow and staple fibers are produced by wet spinning, whereas filaments are produced mostly by dry spinning and partly by wet spinning (Sakurada 1985, 9). When vinylon is produced it is soluble in water and thermoplastic. To make it commercial useful, it is treated with heat and formalin making it insoluble in water. This is due to the fiber becoming partly crystalline, similar to highly stretched, dry rubber (Sakurada 1985, 9).

### 2.2.2 Physical Properties

Vinylon fibers high strength and relatively high modulus, plus, good resistance to weathering and chemicals make for a good fiber for FRP applications. The specific gravity of vinylon fibers ranges from 1.26 to 1.30, compared to 1.45 and 7.85 for aramid and steel respectfully. Heating and drawing of the vinylon molecules increases the orientation of the molecules in the direction of drawing and in turn increases the strength and modulus of the fiber.

The failure mode of PVA fibers is a granular fracture, which is most common with fibers spun from solution. According to Hearle et al. (1989), during the spinning process the fibers coagulate from solution to give a spongy structure with voids filled with excess solvent in the fiber. In the subsequent stretching and drying, the voids elongate, collapse and apparently disappear. But seemingly, the original void

surfaces remain as weak boundaries separating the material into separate fibrillar elements. The progression of a granular fracture is shown in Figure 3.

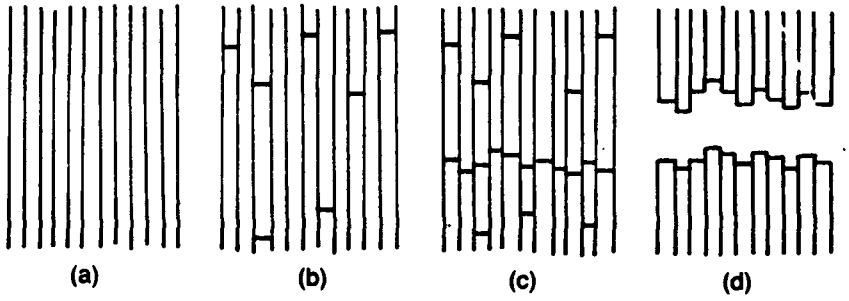


Figure 3. Granular Fracture of Vinylon (Herale et al. 1989, 62)

In Figure 3, part (a) shows the structure of the separate elements. In part (b), as the tension increases, the elements begin to break. However, the discontinuities prevent the occurrence of a large enough stress concentration to cause the crack to propagate across the fiber. Part (c) shows that because of the cohesion between elements, the excess stress is transferred to neighboring elements which are thus more likely to break at a nearby position. Eventually the failure becomes cumulative over a cross section and breaks, as shown in part (d).

### 2.2.3 Mechanical Properties

The mechanical properties of vinylon depend on the conditions of production as well as on the parameters of the stages of fiber

preparation, such as spinning, drawing, heat treatment, and formalization (Sakurada 1985). Table 3 gives mechanical properties of regular and high tenacity (strength per unit weight) vinylon.

From Table 3, it is clear that vinylon has a wide range of breaking strengths and elongations. Very high strength vinylon (tensile strength > 2180 MPa) is prepared by wet spinning in an alkali coagulation bath. Staple fibers with a tensile strength of 1800 MPa or higher have also been obtained by spinning in the presence of boric acid. Recently, vinylon staples with tensile strength greater than 1283 MPa and initial modulus greater than 25.7 GPa have become available commercially (Sakurada 1985)

Table 3. Properties of Vinylon (Sakurada 1985, 362-363)

| | Staple and tow | | Filament | |
|---|---|---|---|---|
| | Regular tenacity | High tenacity | Regular tenacity | High tenacity |
| Tensile Strength, MPa | 513-834 | 873-1347 | 385-513 | 770-1540 |
| Elongation at Failure, % | 12-26 | 9-17 | 17-22 | 6-22 |
| Elastic modulus, GPa | 2.94-7.85 | 7.85-28.4 | 6.86-9.32 | 7.85-28.4 |
| Moisture regain, % 20°C, 65%R.H. | 4.5-5.0 | 3.5-4.5 | 3.5-4.5 | 2.5-4.5 |
| Moisture regain, % 20°C, 90%R.H. | 10.0-12.0 | 8.0-10.0 | 10.0-12.0 | 8.0-10.0 |

Vinylon is a hydrophilic synthetic fiber and has relatively high water absorbency. In fact, it has the highest among the synthetic fibers. The ratio of standard to wet tenacity may be as low as 80%. As with aramid fibers, this could become a problem if the resin matrix in a FRP element becomes weakened (i.e. cracking, crazing, resin-fiber debonding or porosity). More research is needed on the moisture effects on FRP elements.

### 2.2.4 Durability: Behavior in Different Environments

Polyvinyl alcohol fibers have a good resistance to various chemicals, including acids, alkalies, and salts. This is based on comparative tests against nylon in which polyvinyl alcohol fibers proved superior in most instances. (Sakurada 1985)

## 2.3 RESIN

The resin is the matrix that binds or holds the fibers together to form a FRP composite material. The resin performs three major roles: to bind the fibers together with its cohesive and adhesive properties, to allow load transfer between fibers, and to protect fibers from environmental effects (ASM International 1989, 31). In addition, the resin keeps the fibers in proper orientation to carry the intended loads, distributes the load evenly among the fibers, provides resistance to crack propagation, and determines the FRP composite temperature limitations and environmental resistance. Resins are classified into two major groups: thermoplastic or thermosetting.

### 2.3.1 Thermoplastic Resins

The use of thermoplastic resins in FRP composites is not as prevalent as thermosets. Common thermoplastic resins are nylon, polyethylene, polyvinyl chloride (PVC), and polystyrene. The advantage of thermoplastics over thermosets, is the ability to be heated and remolded to any desired shape.

### 2.3.2 Thermosetting Resins

Thermosets have historically been the primary choice for use in FRP composites and account for more than 80% of all resins used (ASM International 1989, 43). Thermosetting resins consist of a liquid resin, a curing agent, fillers and other minor components. The availability of different resin formulations, curing agents and fillers allows tailoring the matrix properties to fit a desired application.

Common types of thermosetting resins are polyesters, polyimides and epoxies. Polyester resins are the most commonly used of all matrix material because they provide a good combination of low cost, versatility, and adequate property performance (ASM International 1989, 31).

In applications where thermal stability at high temperatures is important, polyimide resins are used. Polyimide resins are more expensive and less widely used than polyesters or epoxies, but they provide thermal stability at service temperatures of 260 $^{o}$C and above. This is two times the maximum allowable service temperature for epoxy.

For more structurally demanding applications, epoxy resins are used. Epoxy resins may cost more than polyester resins and not have

the thermal stability at high temperatures as polyimide resins, but they provide an extensive range of physical properties and mechanical capabilities that make them the most versatile of all commercially available matrices (ASM International 1989, 61). By varying the chemical structure of the resin and curing agent, along with the modifying reactants and curing conditions, the physical and mechanical properties can be optimized.

An epoxy resin was used as the matrix for both the kevlar and vinylon hybrid rods in this research project. The epoxy was Epikote #827 with TETA hardener, manufactured by Yuka Shell Epoxy, Japan. Table 4 gives tension and compression properties .

Table 4. Epoxy Resin Properties (Nanni et al. 1992a)

| Property | Tension | Compression |
|---|---|---|
| Density ($gr/cm^3$) | 1.1 to 1.4 | |
| Strength (MPa) | 62 | 90 |
| Elastic Modulus (MPa) | 3820 | 980 |
| Poisson's Ratio | 0.35 | |
| Ultimate elongation (%) | 4.4 | Not Available |

## 2.4 NOTATION

In the following chapters, a three parameter notation is used to identify the different hybrid rods; e.g., K48/9.0 mm/SR24. K48 designates the FRP material type, either aramid (K) or vinylon (V), and skin thickness; 32, 48, 64 or 96. These numbers are related to the number of rovings per yarn and yarns per rod, where individual fibers are bundled into rovings and rovings are combined into yarns. As an example, K64 has 8 rovings/yarn and 8 yarns per rod. Table 5 gives the cross-sectional areas of the different FRP skin materials.

Table 5. Areas of FRP Skin

| Parameter for Skin Thickness Notation | K - Aramid $mm^2$ | V - Vinylon $mm^2$ |
|---|---|---|
| 32 | 24 | -- |
| 48 | 33 | 38 |
| 64 | 42 | 50.5 |
| 96 | 65 | 75 |

The middle parameter in the notation, indicates the steel core diameter; e.g., 9.0 mm. The last parameter, SR24, states the grade of steel core material used, either SR24 (mild round steel bar) or SBPR80 (high strength round steel bar). This choice was based on the fact that the steel was manufactured in Japan under Japanese specifications.

# CHAPTER 3

# UNIAXIAL TENSILE TESTS

## 3.1 TENSILE TEST SET-UP

Two sets of hybrid rods were tested in tension to determine stress-strain relationships and tensile properties (i.e., ultimate strength, $f_u$; elastic modulus, E; and ultimate strain, $\varepsilon_u$). The first set was conducted in 1990 before the start of this project, and is reported here to show how improved manufacturing techniques can affect the properties of FRP materials. From the results of the first set, a second set of hybrid rods were manufactured and tested in 1992 as an integral part of this project. The hybrid rods from the second set are used to reinforce the concrete beams in this research program.

### 3.1.1 First Set

This set of hybrid rods consisted of two groups, which differ by the type of steel core material and thickness of aramid skin. In the first group, the steel core consisted of a mild steel ($f_y$ = 235 MPa). Three smooth rods (diameters of 3, 4, and 6 mm) and a threaded rod (diameter of 6 mm) were used. Five samples for each of the three smooth core rods and three samples with the threaded rod core were tested. In all samples, the skin consisted of K32 aramid FRP with an

area of 24 $mm^2$. The FRP skin, when tested separately, had the following properties: $f_u$ = 1516 MPa; E = 68.4 GPa, and $\varepsilon_u$ = 0.0222 mm/mm.

The second group consisted of hybrid rods made with a high-strength steel core ($f_y$ = 1373 MPa; $f_u$ = 1569 MPa; E = 196 GPa). Two diameters were used, 6 mm and 9.3 mm. The FRP skin consisted of K64 aramid with the following properties: $f_u$ = 1489 MPa; E = 64.9 GPa; Area = 44 $mm^2$. Three samples with the 6 mm core and seven samples with the 9.3 mm core hybrid rod were tested in tension.

### 3.1.2 Second Set

The second set of tests consisted of eleven different types of hybrid rods, varying with respect to FRP skin thickness, FRP skin material, steel core strength, and steel core diameter. Table 6 shows the different combinations of hybrid rods tested. The first two columns designate to skin material type, either K (aramid) or V (vinylon), and the amount of FRP skin per hybrid rod based on manufacturer data (see Section 2.4, Table 5). The last two columns give the different core diameters and the corresponding grade of steel, either round mild steel (SR24) or round high strength steel (SBPR80). The labels "SR24" and "SBPR80" are used in Japan to denote different grades of steel (SR24; $f_y$ = 235 MPa and SBPR80; $f_y$ = 784 MPa).

All eleven hybrid rod types and the four different steel core samples were tested in tension to establish stress-strain curves and tensile properties. Three samples of each type of hybrid rod and plain

Table 6. Combinations of Hybrid Rods (Second Set)

| Skin Material | Area of Skin Material ($mm^2$) | Diameter of Core (mm) | Steel Core Type |
|---|---|---|---|
| K48 | 33 | 9.0 | SR24 |
| K64 | 42 | 9.0 | SR24 |
| K96 | 65 | 9.0 | SR24 |
| K64 | 42 | 9.2 | SBPR80 |
| K96 | 65 | 9.2 | SBPR80 |
| K96 | 65 | 13.0 | SR24 |
| K96 | 65 | 13.0 | SBPR80 |
| V48 | 38 | 9.0 | SR24 |
| V64 | 50 | 9.0 | SR24 |
| V96 | 65 | 9.0 | SR24 |
| V96 | 65 | 9.2 | SBPR80 |

Table 7. Tensile Properties of Braided FRP Material

| Properties | Aramid - K | Vinylon - V |
|---|---|---|
| Ultimate Strength, $f_u$ MPa | 1489 | 429 |
| Elastic Modulus, E GPa | 68.4 | 15.0 |
| Ultimate Strain, $\varepsilon_u$ % | 2.18 | 2.86 |

core rod were tested. The hybrid rods were tested up to failure of the FRP material. The tensile properties for the FRP skin are taken from tests conducted on plain braided FRP rods in 1990 by Nanni et al (1992a). The FRP material properties are listed in Table 7.

### 3.1.3 Testing

All specimens in both sets of tests were made of 1.0 meter long rods including the anchorage system. The anchorage system consisted of a reusable FRP cone filled with epoxy resin and sand as shown schematically in Figure 4.

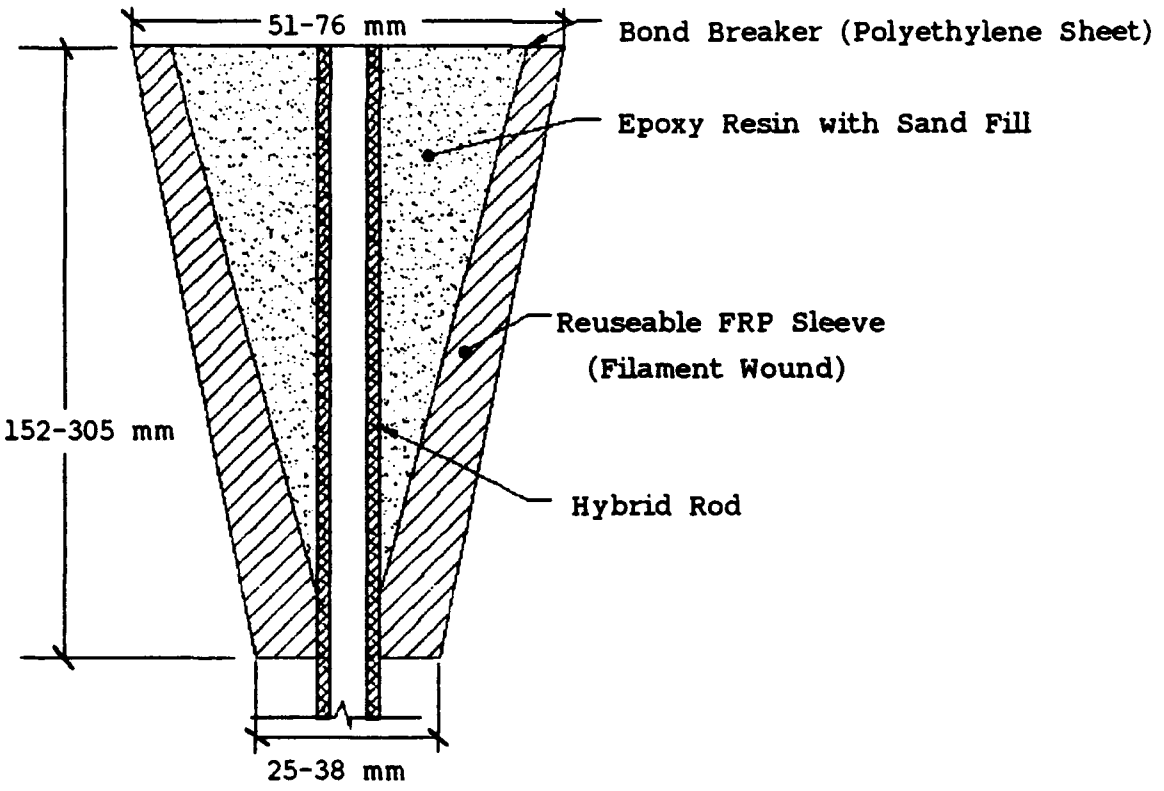


Figure 4. Cross-section of Hybrid Rod Anchor

The sand is used as a filler in the resin and to reduce the cost of each anchor. A polyethylene sheet is used as a bond breaker between the epoxy resin and FRP cone to allow reuse of FRP cone upon completion of test.

Strain gages were attached at mid-length in the longitudinal and transverse directions. The uniaxial static tests were conducted in a specially modified frame to absorb the energy suddenly released by the rods at failure. Figure 5 shows one of the hybrid rods in the testing apparatus. In all cases the tests were halted after failure of the FRP skin.

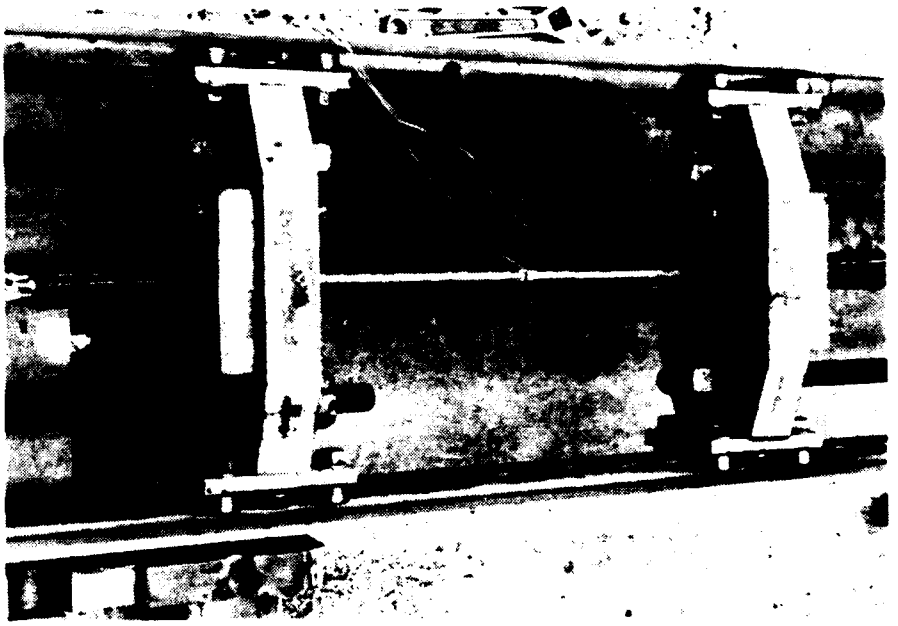

Figure 5. Tensile Testing Apparatus

## 3.2 TEST RESULTS AND OBSERVATIONS

To ease organization, raw data of the uniaxial tensile tests is contained in Appendix A, Uniaxial Tensile Test Data. Included in Appendix A are photos of failed hybrid rods (second set hybrid rods only), load-strain curves for each of the hybrid and steel core rods tested (all hybrid rods tested), and stress-strain curves of the rods compared with theoretical curves (all hybrid rods tested).

The strain that is measured experimentally, is only the strain on the surface of the hybrid rod, it does not represent the entire strain across the cross-section of the hybrid rod. Since a hybrid rod is composed of different materials, the strain distribution cannot be linear, as in the case of a single material rod (e.g., steel). For this project, a constant strain distribution across the hybrid rod cross-section is assumed to ease in calculations of theoretical curves.

An average load-strain curve is determined by specifying a range of load for each hybrid rod type, then calculating the strain at each specified load based on the actual individual sample load-strain curve. The average strain is then calculated at each specified load value (Example: $(\varepsilon_{\text{sample 1}} + \varepsilon_{\text{sample 2}} + \ldots + \varepsilon_{\text{sample N}})/N$).

The stress-strain curves for each hybrid rod is based on the average load-strain curve of the samples tested. The stress for each hybrid rod is calculated from the load divided by the total area of the hybrid rod ($\text{Area}_{\text{hybrid}} = \text{Area}_{\text{steel core}} + \text{Area}_{\text{FRP skin}}$). Since there is no way of knowing the stress in the steel core, it is assumed that the calculated stress is constant across the hybrid rod cross-section.

The theoretical curves are calculated using the law of mixtures (e.g., $E_{Hybrid} = V_{FRP}*E_{FRP} + V_{Core}*E_{Core}$, where V is the volume percentage of the component). To obtain a more accurate representation, the material properties (i.e. steel core yield strength, $f_y$, and FRP ultimate strength, $f_u$) are based on the actual test data, not on the nominal strengths.

Tables 8 and 9 give a summary of the test data for the two sets of uniaxial tensile tests. Column 1 designates the rod type used in the tests. Column 2 shows the mean sample ultimate load for each different rod type. Column 3 is the coefficient of variation for the samples tested and is defined as the standard deviation divided by the mean for the samples. Columns 4 is the theoretical ultimate load based on the sum of the individual components (law of mixtures).

In the first set of tests, the hybrid rods with the K32 FRP skin had ultimate loads that were 19% to 44% less than the theoretical. The hybrid rods with the K32 skin also had the highest coefficient of variation of all the rods tested. This was due to inconsistency in manufacturing technique since these were the first rods produced.

The ultimate strain for aramid hybrid rods ranged between 2.78 and 2.95 percent. These values are considerably higher than that of aramid FRP rods tested individually. The ultimate strain for the vinylon hybrid rods ranged between 2.05 to 3.15 percent, which is approximately the same as plain vinylon FRP rods.

The failure mode of the hybrid rods was always initiated by FRP skin failure. In hybrid rods with a high strength steel core, total

Table 8. Tensile Test Results for First Set of Hybrid Rods

| Rod Type (1) | $P_u$ (kN) (2) | C.V. (%) (3) | $P_{u,t}$ (kN) (4) |
|---|---|---|---|
| K32/3.0 mm | 31.4* | 6.9 | 37.4 |
| K32/4.0 mm | 31.2 | 14.9 | 38.7 |
| K32/6.0 mm | 29.5 | 15.7 | 42.4 |
| K32/6.0 mm/Threaded | 29.8* | 4.2 | 41.3 |
| K64/6.0 mm | 113.5 | 3.3 | 101.2 |
| K64/9.3 mm | 162.7 | 1.48 | 155.6 |

* One sample failed at grip

Table 9. Tensile Test Results for Second Set of Hybrid Rods

| Rod Type (1) | $P_u$ (kN) (2) | C.V. (%) (3) | $P_{u,t}$ (kN) (4) |
|---|---|---|---|
| K48/9.0 mm/SR24 | 71.1 | 3.8 | 68.1 |
| K64/9.0 mm/SR24 | 88.1 | 4.9 | 81.4 |
| K96/9.0 mm/SR24 | 116.5 | 8.4 | 115.6 |
| K96/13.0 mm/SR24 | 142.6 | 4.9 | 136.3 |
| V48/9.0 mm/SR24 | 33.9 | 2.6 | 35.3 |
| V64/9.0 mm/SR24 | 38.5 | 3.4 | 40.8 |
| V96/9.0 mm/SR24 | 43.3 | 5.9 | 51.3 |
| K64/9.2 mm/SBPR80 | 163.0 | 1.9 | 152.1 |
| K96/9.2 mm/SBPR80 | 187.9 | 1.6 | 186.2 |
| K96/13.0 mm/SBPR80 | 295.3 | 1.2 | 275.7 |
| V96/9.2 mm/SBPR80 | 123.1* | 1.2 | 118.1 |

* One sample failed at grip

failure of the core usually followed because of the low steel ductility. In rods with the mild strength steel there was no core failure because of the high ductility of the steel. The type of FRP skin also determined the type of failure mode. Rods with aramid skin tended to rupture in the center portion with many axial splits. The rods with a vinylon skin showed a tendency to fail close to the anchors and had cleaner breaks.

The failure of the aramid hybrid rods also displayed the typical bird caging of the FRP skin at the supports. Bird caging results from energy released when the aramid skin failed. Figure 6 shows a failed hybrid rod with aramid skin.

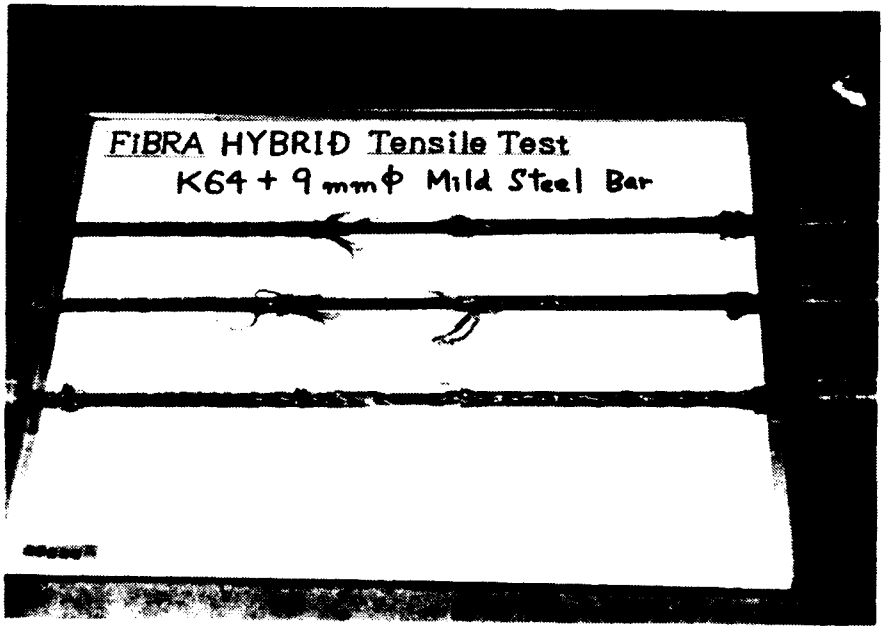


Figure 6. Failed Aramid Hybrid Rod

The difference in failure modes between the FRP skins is expected since the failure mode of the individual fibers is different. The failure mode of the individual vinylon fibers is a granular failure (see Section 2.2.2) as opposed to an axial failure for the aramid fibers (see Section 2.1.2). Figure 7 shows a failed vinylon hybrid rod with the rupture of the skin close to the anchors.

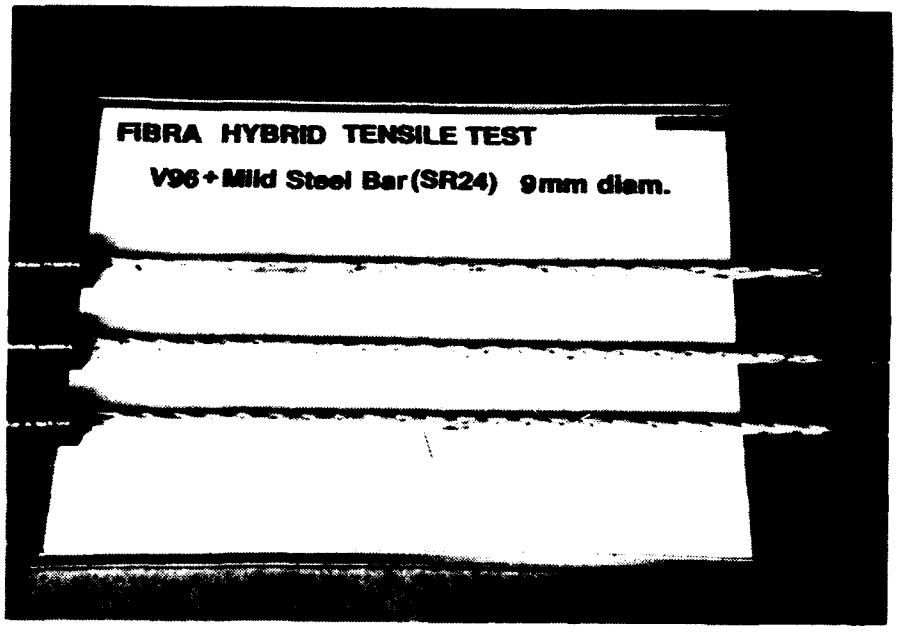


Figure 7. Failed Vinylon Hybrid Rod

The difference in location of failure is most likely attributed to the differences in mechanical properties of the fibers. It is possible that the transverse strength of vinylon is significantly less than the

aramid. This would account for the hybrid rods with vinylon skin failing at the anchors. As the rod is loaded, the grips apply a transverse and longitudinal force on the FRP skin. If the FRP fiber is weak in the transverse direction, the stress/strain concentrations at the anchor would case failure in the rod at the point leading into the anchors.

## 3.3 DISCUSSION OF RESULTS

The results from the uniaxial tensile testing show a number of important aspects of the hybrid rods. First of all, the stress-strain diagrams displayed a bi-linear behavior. All of the rods tested clearly showed a point at which the steel core started yielding. An example of this is displayed in Figure 8, which is the stress-strain curve for K96/9.2 mm/SBPR80. Also plotted on the graph is the stress-strain curves for the 9.2 mm high strength steel core and a plain K96 aramid rod. The data for the K96 rod came from tests conducted by Nanni et al. (1992a) in 1991 on plain aramid FRP rods. Figure 8 clearly shows that up to steel yield, the capacity of the hybrid rod is dependent on the strength of core material. During this period the stress or load is transferred to the core via the bond between the core and skin. After the steel core has yielded, the increase in capacity of the hybrid rod becomes solely dependent on the FRP skin material.

It is evident from Figure 8 that the curve of the hybrid rod falls in between the curves of the individual components, steel and aramid. This is important in trying to predict a stress-strain curve for design

purposes. Using the law of mixtures, theoretical stress-strain curves were developed and compared with the experimental curves. Figure 9 shows a comparison of the experimental results with theoretical curves.

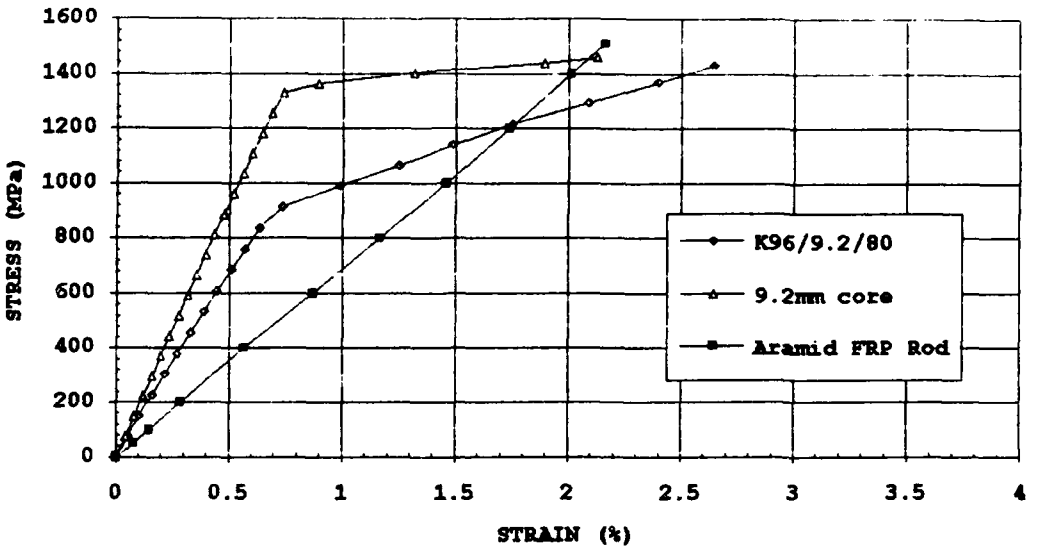


Figure 8. Stress-Strain Curve: K96/9.2 mm/SBPR80

In Figure 9, the experimental curve for the aramid hybrid rod follows the theoretical curve almost exactly up to yielding of the steel but then gradually deviates to below the theoretical curve. This deviation could be attributed partially to bond slippage between the aramid skin and steel core, which cases a loss of rigidity in the rod. The deviation could also be due to the assumed perfectly elastic-plastic stress-strain behavior for the steel core. The theoretical curve for the vinylon hybrid rod runs slightly below the experimental results. This is

probably due to the unconservative assumption that the theoretical stress-strain curve for vinylon is linearly elastic, when in actuality the curve is slightly non-linear. Figure 9 also shows that the strain measured on the surface of the hybrid rod can be used as a valid measurement since the theoretical stress-strain curve followed the experimental almost exactly.

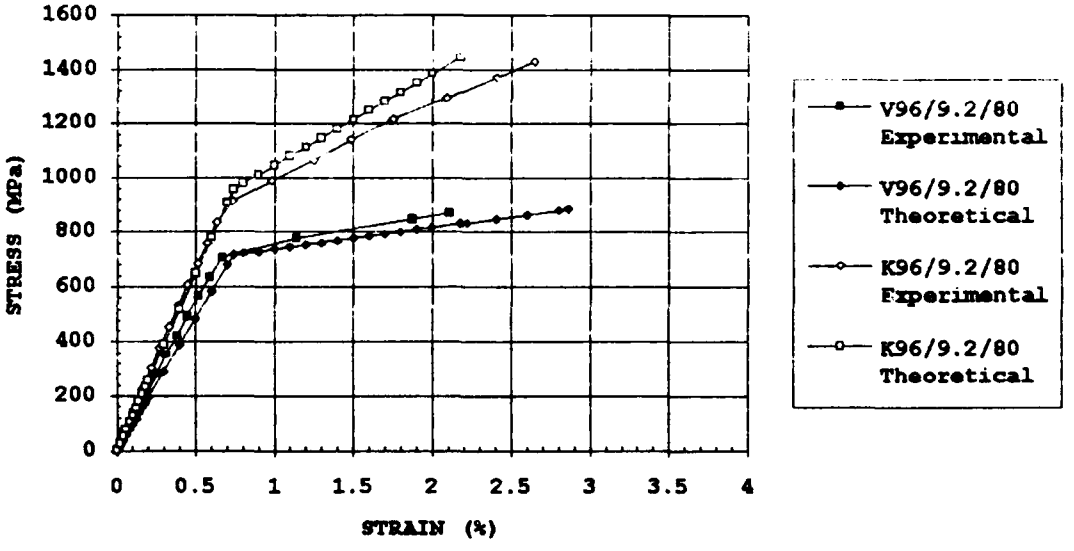


Figure 9. Stress-Strain Curve: Experimental and Theoretical, K96 and V96 with 9.2 mm/SBPR80 Core

As expected, it was found that vinylon FRP had little effect on increasing the strength of the steel core, whereas, aramid increased the strength considerably. Figures 10 and 11 compare two hybrid rods (K96/9.2 mm/SBPR80 and V96/9.2 mm/SBPR80) with the same FRP skin thickness and core material, but different FRP material. Figure 10 is a

load-strain diagram and Figure 11 is a stress-strain diagram. Figure 10 shows that the load capacity of the aramid hybrid rod is significantly greater than the vinylon hybrid rod and steel core. Figure 11 shows that while the aramid hybrid rod has a higher load capacity, its rigidity (elastic modulus, E) based on total rod area, is less than the 9.2 mm steel core but greater than the vinylon hybrid rod.

It was also found that increasing the area of FRP skin material increased the load capacity of the hybrid rod. Figures 12 and 13 are load-strain curves for vinylon and aramid hybrid rods with mild strength steel (9.0 mm/SR24) core. In both figures, the load capacity of the hybrid rod increased with the increase of FRP skin.

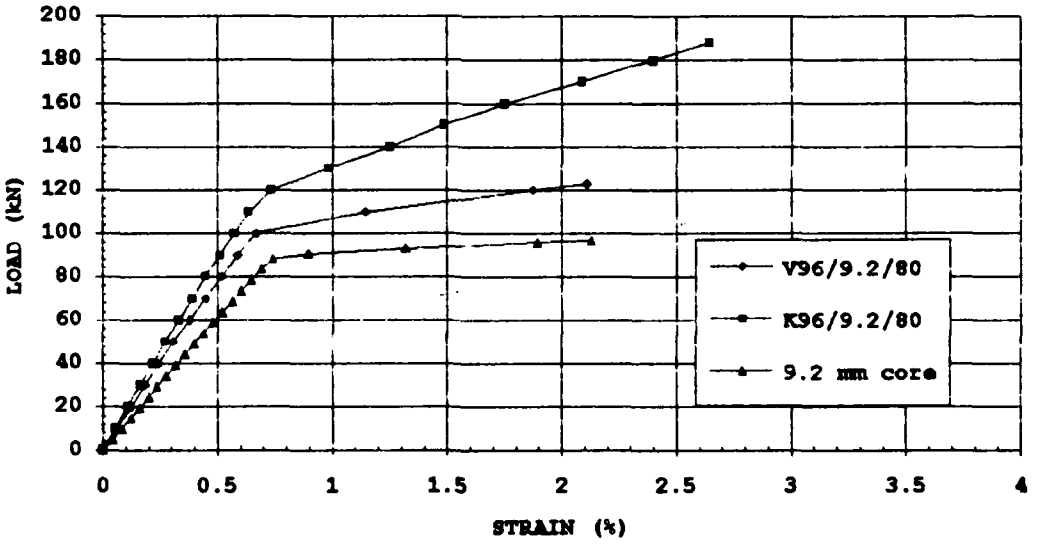


Figure 10. Load-Strain Curve: K96 and V96 with 9.2 mm/SBPR80 Steel Core

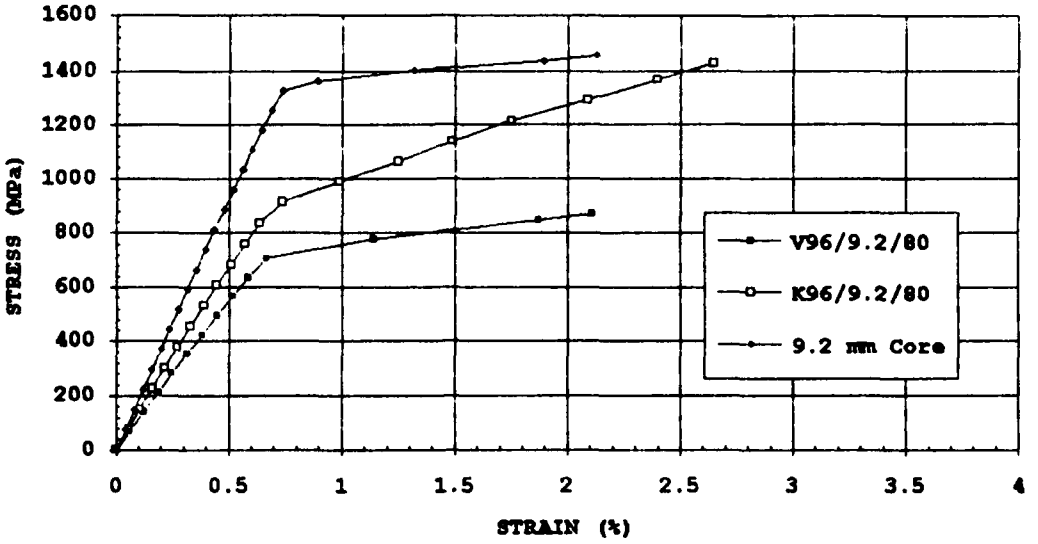


Figure 11. Stress-Strain Curve: K96 and V96 with 9.2 mm/SBPR80 Steel Core

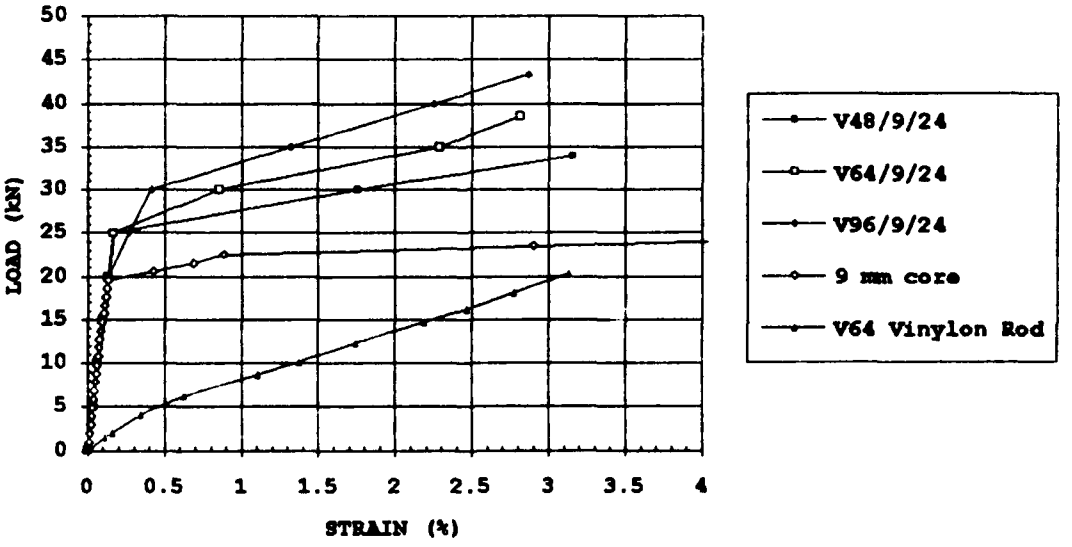


Figure 12. Load-Strain Curve: Increasing Cross-Section of Vinylon Skin

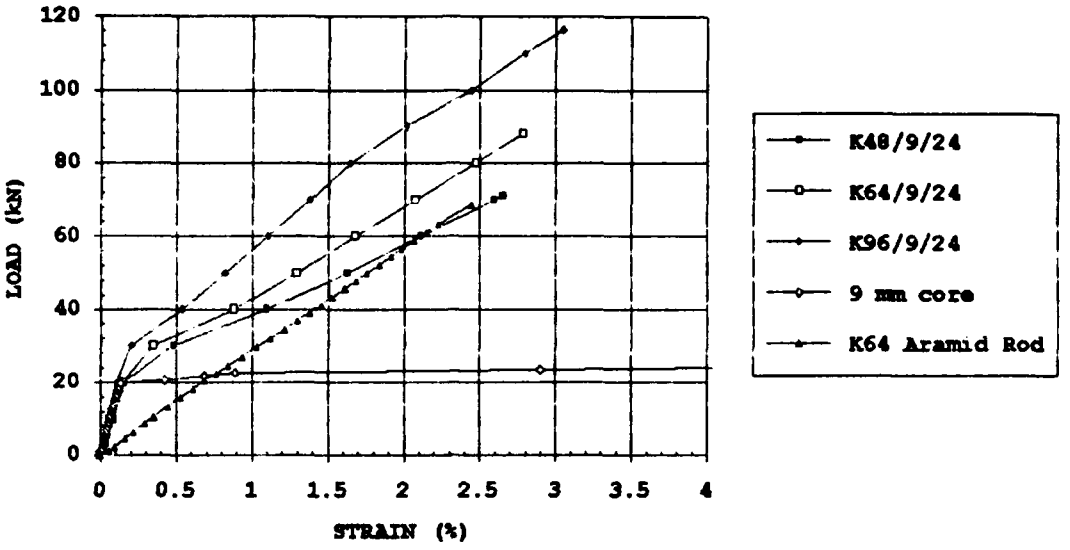


Figure 13. Load-Strain Curve: Increasing Cross-Section of Aramid Skin

## 3.4 CONCLUSIONS

The uniaxial tensile tests demonstrated that a hybrid rod, composed of an FRP skin and steel core, performs as expected (based on law of mixtures). The combination of FRP skin and steel core provides utilization of the best properties of each material. The FRP skin could provide corrosion protection (to be established in future projects), and if high strength FRP skin is used, can substantially increase the tensile capacity of the steel. In the rods with aramid skin, the strength gain was large, especially in the case of a mild strength steel core. The steel core provided improved rigidity in the elastic range and a plastic range that plain FRP rods do not have. By varying the FRP skin material, skin thickness, steel core diameter, and strength of steel core,

a designer could tailor the concrete reinforcement to a specific application.

The experimental curves compared well with the analytical curves. Using the law of mixtures and the stress-strain behavior of the hybrid rod components (FRP and steel), analytical stress-strain curves were calculated that closely followed the experimental stress-strain curves up through the elastic range and then deviated slightly in the plastic range. The deviation was due to the assumed perfect bond and linear elasto-plastic behavior of the steel. The assumed constant strain distribution across the cross-section was a good approximation. This shows that using the law of mixtures and constant strain distribution across the rod cross-section, allows adequate predictions of hybrid rod performance.

# CHAPTER 4

# REINFORCED CONCRETE BEAM TESTS

## 4.1 CONCRETE BEAM TEST SET-UP

Eighteen reinforced concrete beams were constructed and tested in flexure to evaluate the behavior of the hybrid rods in a reinforced concrete application. The following hybrid rod types were tested: K48, K64, K96, V48, V64, and V96 with the mild strength steel (SR24) 9.0 mm core, and K96 with the mild strength steel (SR24) 13.0 mm core. For comparison, beams reinforced with smooth 13.0 mm rod (SBPR80) and conventional #4 (fy = 414 MPa, Dia. = 12.7 mm) and #5 (fy = 276 MPa, Dia. = 15.87 mm) rebar are tested.

Two test beams for each type of reinforcement were constructed except for the smooth 13.0 mm rod and the #4 rebar which only had one test beam. Figures 14 and 15 show the reinforcement spacing and placement in the test beams. Figure 16 is a photo of the rebar cage with a hybrid rod. Figures' B4 through B8 in Appendix B (Beam Test Data) contain detailed photos of the rebar cages for the smooth 13.0 mm rod and conventional steel rebar.

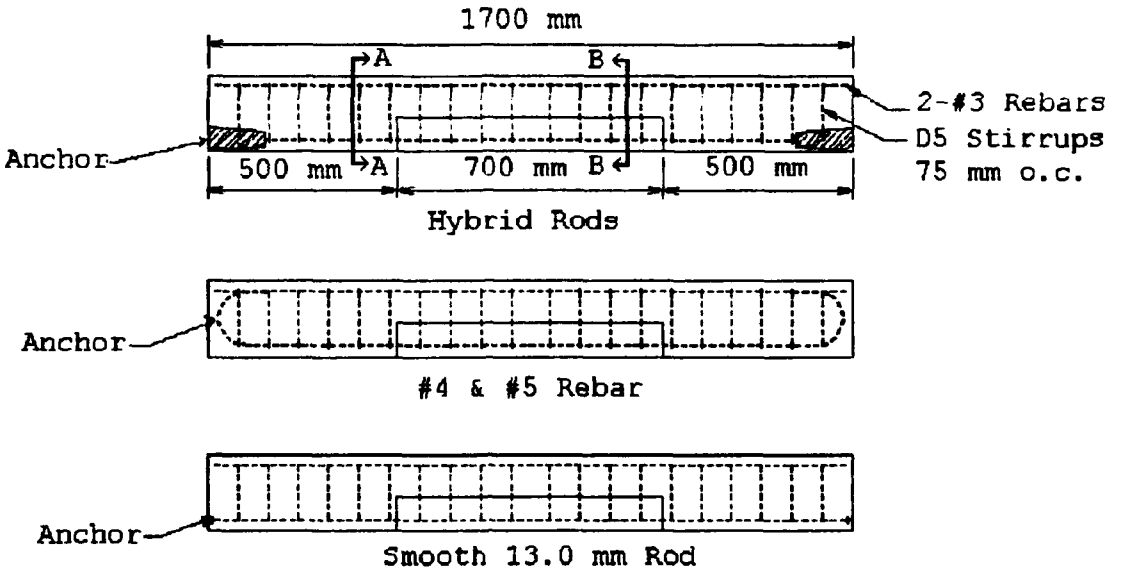


**Figure 14. Reinforcement Configuration**

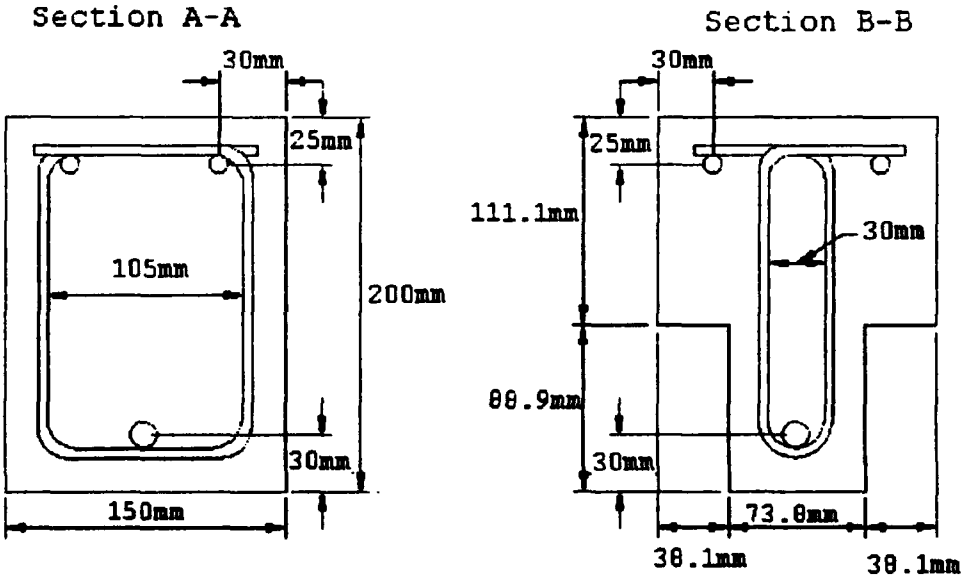


**Figure 15. Cross-section Diagram of Test Beams**

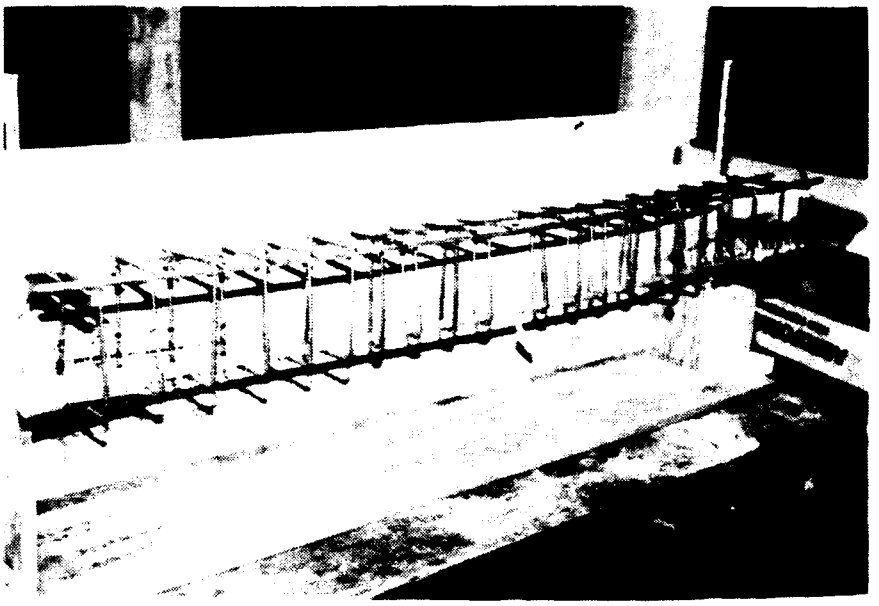

Figure 16. Rebar Cage with Hybrid Rod

The choice of the beam shape and geometry is based on the following factors:

- Flexural capacity had to be limited because of the constraints of the test frame and load actuator. From theoretical calculations, the range of ultimate loads for beams reinforced with one rod is 24 kN for V48/9.0 mm/SR24 to 69 kN for K96/13.0 mm/SR24. The MTS load actuator and hydraulic system had a load capacity of 98 kN.
- To use a closed loop system, the beam had to fit within the test frame that limited the length to approximately 1.8 meters.

- A limited number of hybrid rods available precluded using more than one rod per beam.
- The concrete cover thickness needed to represent field conditions to fully evaluate cracking patterns and behavior.
- Decrease the chance of a shear failure in the beams.

This led to the T-beam section in the central 70 cm of the beams (see Figure 14). The end sections of the beams were left full width to provide adequate support surfaces and to ensure that the rod end anchors would not fail. The beam can be considered a pure T-beam due to the fact that the load acts sufficiently within the T-section based on Saint-Venant's Principle (Cook and Young 1989). Saint-Venant's Principle states that stresses change appreciably only in the neighborhood of the loaded region. The term "neighborhood" is defined as the material whose distance from the center of the loaded region is roughly equal to the largest span of the loaded region.

The stirrup size and spacing is based on the maximum theoretical load calculated, 69 kN. Using ACI Code 318-89 procedures, and assuming a stirrup size of D5 deformed wire; As = 32.3 $mm^2$ (0.05 $in^2$), $f_y$ = 517 MPa (75 ksi) minimum yield strength stress. The calculated spacing was 81.4 mm (3.2 in). A spacing of 75 mm was used to provide a factor of safety and to ease construction.

To insure composite action between tension reinforcement and the concrete, the ends of the rods were anchored or hooked. The conventional #4 and #5 rebar had the ends hooked as shown in Figure B6. The smooth 13.0 mm rod had its ends threaded to allow washers backed by nuts to be placed on the ends. Figure B8 in Appendix B

shows one of the end anchors for the smooth 13.0 mm rod. The anchors used for the hybrid rods are similar to the anchors used in the tensile tests; disposable fiberglass cones filled with epoxy resin and sand. A cross-section is displayed in Chapter 3, Figure 4. In Appendix B, Figures B1 to B3 are photos of anchors used.

## 4.2 CASTING OF CONCRETE BEAMS

The concrete used for the test beams was a Type I cement with pea gravel and a superplastizer (MB Rheo-1000 8.oz/100wt) to insure consolidation with little vibration. 101 mm x 203 mm (4" x 8") cylinders were used to obtain compressive strength of the concrete at 3, 7, 14 and 21 days. Four samples were tested at each interval. The concrete had a compressive strength of 35.86 MPa (5200 psi) after 21 days. Figure 17 is a graph of the concrete strength.

Detailed photos of beam fabrication is contained in Appendix B, Figures B4 to B9. The photos show the construction of the rebar cages. Each one of the 360 stirrups was cut and bent by hand. The compression steel [two #3 rebars, $f_y$ = 414 MPa (60 ksi)] served two purposes; to provide added strength and ductility to the test beams, and more importantly, as a means of supporting the rebar cage during construction. Figure's B10 and B11 show how the cages were placed in the forms. The wood strips across the top provide added stability to

the forms. To lift the rebar cages off the bottom of the form, tie wire is used to hang the cages from the wood strips. This helped control the depth of the reinforcement and insured uniform construction.

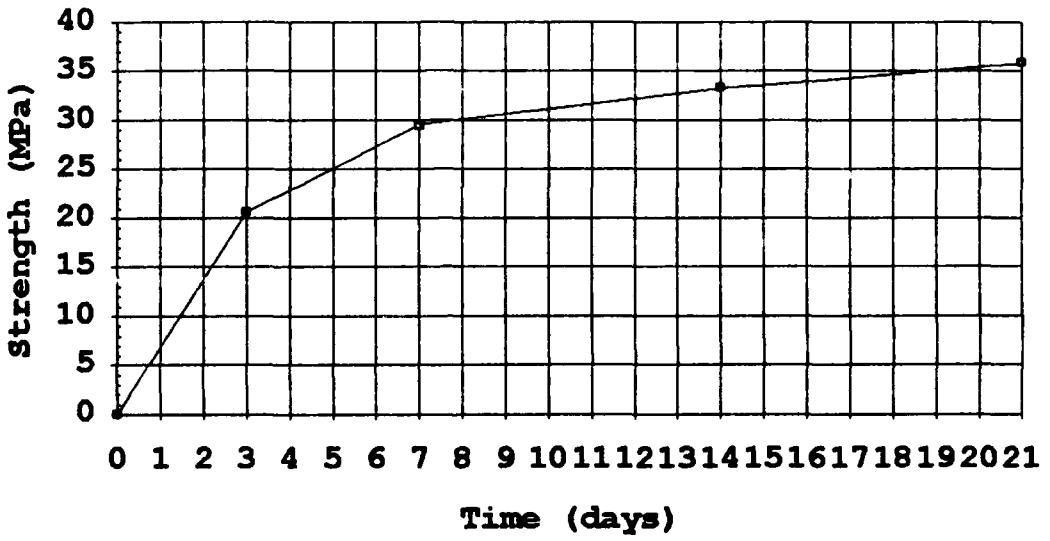


Figure 17. Graph of Concrete Strength

Figure's B12 and B13 show the placing of the concrete. The concrete was placed in two lifts to insure adequate vibration and to reduce initial stress on the form. The wood strips were removed after the concrete had set to allow a good finish.

## 4.3 TESTING

### 4.3.1 Equipment

Testing was done in the Architectural Engineering Structures Lab. The testing assembly consisted of a testing frame, MTS hydraulic pump, MTS actuator with internal LVDT, MTS 98 kN load cell and MTS electronic control system. Figure 18 is a diagram of the testing assembly.

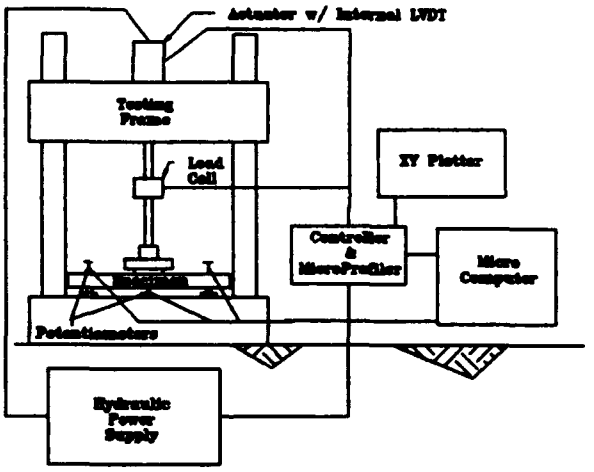


Figure 18. Test Equipment Assembly

A total of four potentiometers were used to measure displacement; two at the center of the beam to measure deflection, and one over each support to measure settlement. Figure 19 is a diagram of the beam testing setup, showing load placement and location of potentiometers. Figure 20 shows one of the test beams' setup for testing.

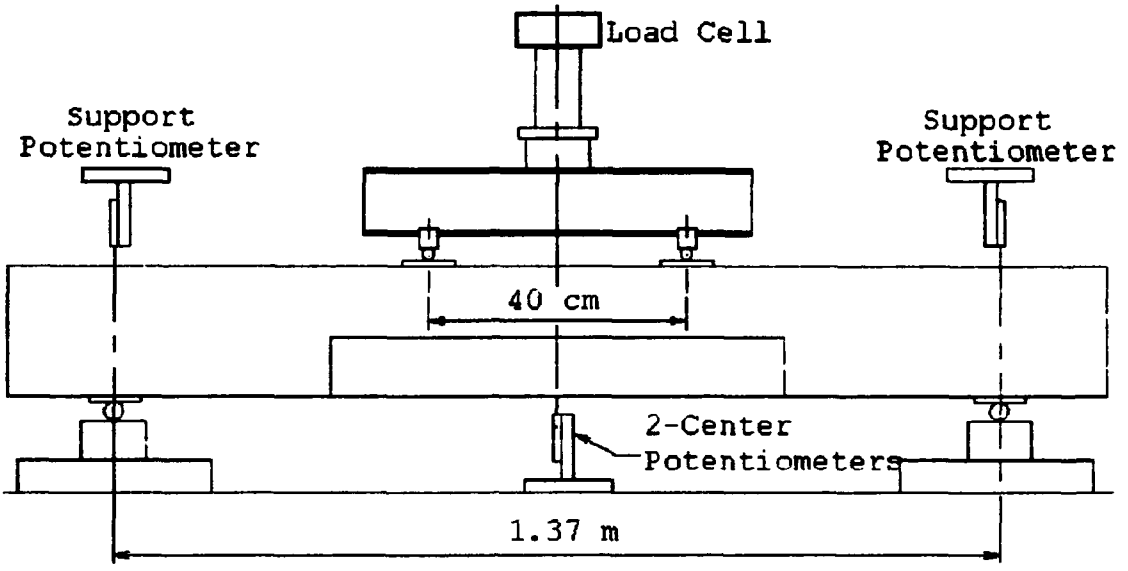


**Figure 19. Diagram of Beam Test Setup**

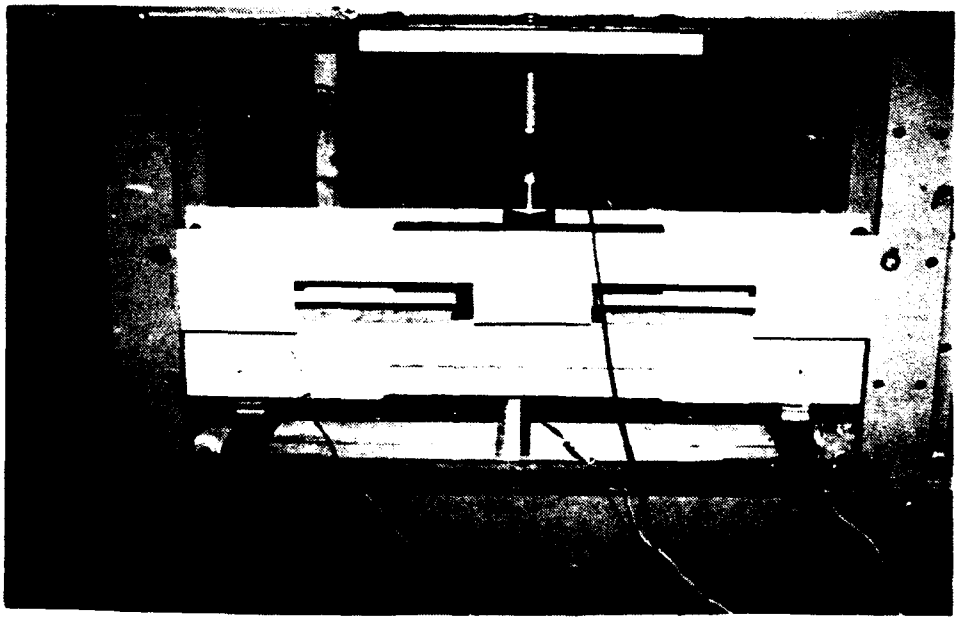

**Figure 20. Beam Setup for Testing**

Data acquisition was accomplished by personal computer with Notebook/SE software and an XY-plotter plotting load versus LVDT displacement. The XY-plotter was used as data backup in case of a malfunction with Notebook/SE data acquisition program. Figure B43 in Appendix B is an example of a plot obtained from the XY-plotter.

### 4.3.2 Loading Procedure

Testing of each beam consisted of loading and unloading cycles to show the elasto-plastic behavior of the beams and to obtain an envelope of the load-deflection curve. Five cycles were accomplished before the beam was taken up to failure. Table 10 gives the displacement, based on span length (L), at which each loading cycle was interrupted and held to map the cracks.

Table 10. Loading and Unloading Cycles

| Cycle | Displacement (mm) |
|---|---|
| #1 - L/1000 | 1.37 |
| #2 - L/500 | 2.74 |
| #3 - L/300 | 4.57 |
| #4 - L/100 | 13.70 |
| #5 - L/50 | 27.4 |

The testing procedure involved programming the Micro-Profiler contained in the MTS Controller with a loading and unloading profile. The controller was set in stroke (displacement) control with a loading rate of 1.27 mm/min (0.05 in/min) and an unloading rate of 12.7 mm/min (0.5 in/min). The personal computer displayed a real time reading of the load, LVDT displacement, and the two center potentiometers' displacements. Loading was manually stopped when the average of the center potentiometers reached one of the loading cycle displacement thresholds. Once the loading was halted, beams were examined and cracks mapped to aid in tracing after failure. After the 5th cycle, the center potentiometers were removed and the beam was taken to failure.

## 4.4 TEST RESULTS

After the test completion, the raw data was downloaded to a spreadsheet program for manipulation. A sample of the raw data is plotted in Figure 21 to indicate the accuracy of the data gathered.

The net load-deflection curves are calculated from the raw data by subtracting the average settlement of the two supports from the average reading of the two center potentiometers. After the fifth cycle, when the center potentiometers are removed, the data from the LVDT is used to plot the remainder of the curve. To adjust the LVDT data to correspond better with the potentiometer data, the difference between the last average reading from the center potentiometers and the LVDT

reading at that point is subtracted from the LVDT data. Appendix B contains the net load-deflection curves of the beam tests.

It should be mentioned that the beam reinforced with the #4 bar (Test Beam #2) was damaged during testing. Therefore, no data is available for that test.

Appendix B also contains load-deflection curves comparing both experimental and theoretical data for beams tested with the different types of hybrid rods. The theoretical curve is plotted by finding three key points: concrete cracking, steel core yield, and ultimate (failure of FRP skin). From these three points, a predicted load-deflection is developed, as shown in Figure 22.

Up to Point 1, the beam is in the elastic uncracked range with the concrete providing the majority of the tensile resistance. The slope of the load-deflection curve corresponds to the flexural stiffness, $E_cI_g$ ($E_c$ is defined as the elastic modulus of concrete and $I_g$ is the gross moment of inertia for the beam cross-section), of the beam. When the beam cracks, Point 1 in Figure 22, the contribution of the concrete in the tension zone becomes negligible. This causes a decrease in rigidity of the beam and an upward shift in the neutral axis to maintain force equilibrium in the section. In Stage II, the beam still exhibits elastic behavior except the slope of the load-deflection curve has decreased due to the decrease in stiffness, $E_cI_{cr}$ ($I_{cr}$ is defined as the moment of inertia of the cracked cross-section). Stage III begins when the tensile steel yields, point 2 in Figure 22. The slope of the load-

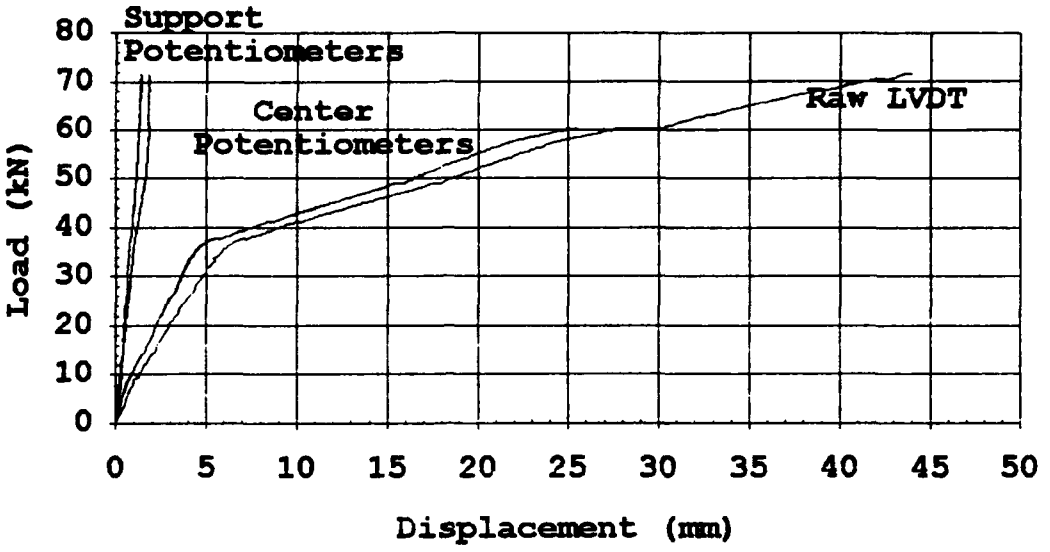


Figure 21. Graph of Raw Data for K96/13.0 mm

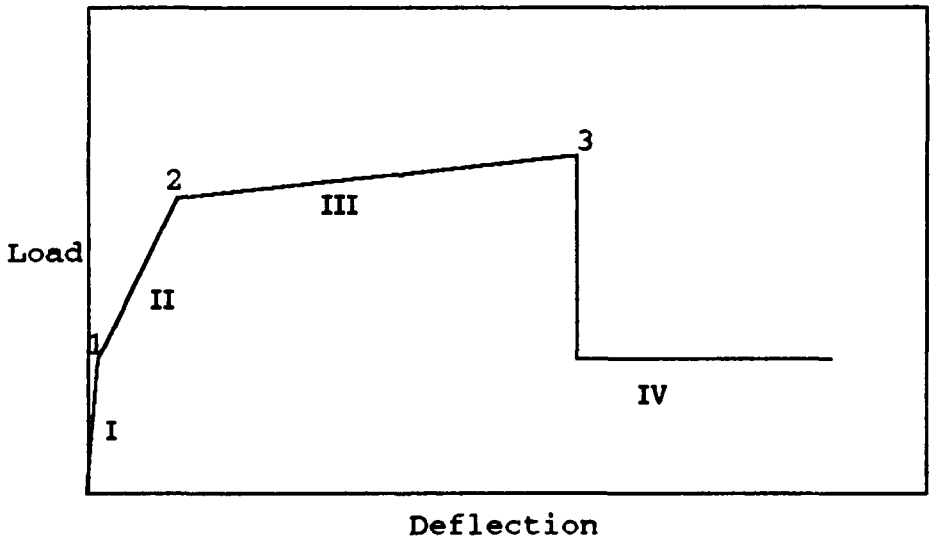


Figure 22. Predicted Shape of Load-Deflection Curve

deflection curve is further decreased because of the change in the elastic modulus ($E_s$) of the tensile steel and the continued upward shift of the neutral axis (decrease in cracked moment of inertia, $I_{cr}$). In a conventional steel reinforced beam, Stage III ends (point 3) with compression failure of concrete. In beams reinforced with hybrid rods point 3 denotes the failure of the FRP skin. Since the strain capacity of the steel core is greater than that of the FRP skin (aramid or vinylon), the beam is still able to sustain load, Stage IV. This load is related to the yield strength of the steel core.

For analytical computations, reinforced concrete assumptions are made; i.e., perfect bond between bar and concrete, plain sections remain plain, and stress at any point depends on the strain at that point in a manner given by the stress-strain diagram of the material (Nilson and Winter 1986). A detailed description of the theoretical calculation is contained in Appendix C.

A summary of the experimental and theoretical results is contained in Table 11. For the test beams with hybrid rods, the ultimate load (L) and deflection ($\delta$) is taken as the point at which the hybrid rod fails (FRP skin failure). The load and deflection at yield is given for the beams reinforced with conventional rebar #5 this provides a better comparison with the theoretical yield values. No comparisons are made for the smooth 13.0 mm rod because anchorage failure occurred before the steel yielded.

The final section of Appendix B contains tracings of the cracking patterns for all of the test beams. The tracings show the cracked

Table 11. Experimental and Theoretical Results

| | | Experimental | | Theoretical | | |
|---|---|---|---|---|---|---|
| | | Ultimate | | | | |
| Reinforcement Type | Test # | $L_e$ (kN) | $\delta_e$ (mm) | $L_t$ (kN) | $\delta_t$ (mm) | $L_e/L_t$ |
| K48/9.0 mm /SR24 | #3 | 42.80 | 34.83 | 44.31 | 26.04 | 0.966 |
| | #14 | 43.19 | 37.41 | | | 0.975 |
| K64/9.0 mm /SR24 | #4 | 49.23 | 37.78 | 49.87 | 25.04 | 0.987 |
| | #16 | 44.32 | 36.69 | | | 0.889 |
| K96/9.0 mm /SR24 | #6 | 56.64 | 36.09 | 61.77 | 22.78 | 0.917 |
| | #11 | 62.39 | 43.51 | | | 1.01 |
| V48/9.0 mm /SR24 | #5 | 19.90 | 16.79 | 24.80 | 27.72 | 0.802 |
| | #17 | 19.25 | 14.12 | | | 0.776 |
| V64/9.0 mm /SR24 | #8 | 21.85 | 21.16 | 27.28 | 27.86 | 0.801 |
| | #15 | 22.81 | 24.12 | | | 0.836 |
| V96/9.0 mm /SR24 | #9 | 26.11 | 25.58 | 32.09 | 27.71 | 0.814 |
| | #12 | 27.89 | 26.92 | | | 0.869 |
| K96/9.0 mm /SR24 | #7 | 72.17 | 42.63 | 69.39 | 19.98 | 1.04 |
| | #13 | 71.77 | 38.04 | | | 1.03 |
| | | Yield | | | | |
| #5 Rebar | #1 | 41.23 | 3.55 | 47.06 | 2.97 | 0.876 |
| | #18 | 43.27 | 4.79 | | | 0.919 |

central section of each of the beams. The numbers on the cracks indicate the load at which the loading was stopped, and the crack was mapped. A 38 mm x 38 mm grid is drawn on the test beams to aid in crack location and tracing. Table 12 contains a quantitative summary of the cracking patterns. Column 3 gives the number of primary cracks, which are defined as cracks that propagated to the compression zone of the beam. Column 4 is the average spacing of primary cracks. Columns 5 and 6 indicate the presence of longitudinal cracks at the level of tensile reinforcement and local concrete crushing at the load points.

From crack pattern tracings and Table 12, it is apparent that the cracking patterns are dependent on the type of reinforcement. The beams reinforced with hybrid rods had fewer cracks and a greater spacing between cracks than beams reinforced with conventional reinforcement (#5 rebar). In the beams reinforced with the aramid hybrid rods, longitudinal cracks occurred at the level of reinforcement. As the thickness of the aramid skin increased, the amount and severity of the longitudinal cracks increased. The longitudinal cracks led to spalling of the concrete when the hybrid rod ruptured due to the energy release from the aramid skin. Figure 23 shows the spalling of the concrete at failure in one of the beams with K96/9.0 mm hybrid rod.

Table 12. Summary of Crack Patterns

| Rod Type (1) | Test # (2) | # of Primary Cracks (3) | Average Spacing, mm (4) | Longitudinal Cracks (5) | Local Concrete Crushing (6) |
|---|---|---|---|---|---|
| V96/9.0 mm | #9 | 4 | 152 | no | yes |
| | #12 | 6 | 127 | no | yes |
| V64/9.0 mm | #8 | 4 | 139 | no | yes |
| | #15 | 4 | 139 | yes | yes |
| V48/9.0 mm | #5 | 4 | 165 | no | yes |
| | #17 | 3 | 177 | no | yes |
| K96/9.0 mm | #6 | 5 | 152 | yes, major spalling | yes |
| | #11 | 6 | 139 | yes, major spalling | yes |
| K64/9.0 mm | #4 | 6 | 127 | yes | yes |
| | #16 | 6 | 114 | yes | yes |
| K48/9.0 mm | #3 | 4 | 152 | yes | no |
| | #14 | 4 | 165 | yes, minor | yes |
| K96/13.0 mm | #7 | 7 | 102 | yes, major spalling | yes |
| | #13 | 7 | 114 | yes, major spalling | yes |
| Smooth 13.0 mm | #10 | 4 | 109 | no | yes |
| #5 rebar | #1 | 8 | 102 | no | yes, major |
| | #18 | 6 | 102 | no | yes, major |

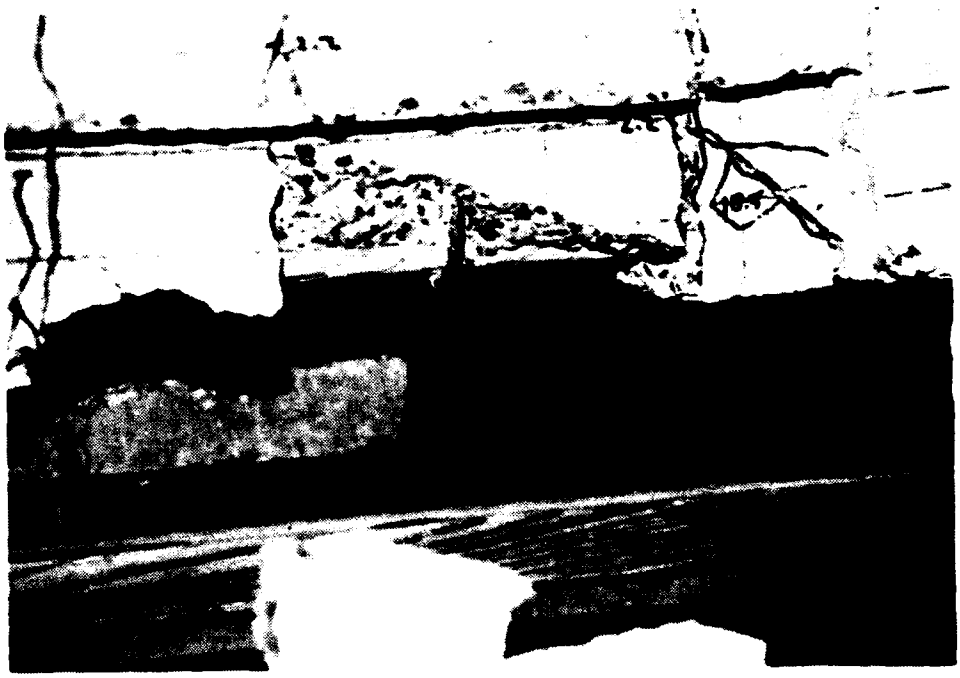

Figure 23. Failed Beam with K96/9.0 mm Hybrid Rod

# CHAPTER 5

# DISCUSSION OF BEAM TEST RESULTS

## 5.1 BEAMS WITH VINYLON AND ARAMID HYBRID RODS

Figures 24 and 25 show the combined load-deflection curves of aramid and vinylon hybrid rod reinforced beams. In all of the beams with hybrid reinforcement, the load-deflection curves displayed the 4 stage pattern given in Figure 22. The cracking loads are approximately the same for all of the test beams, 8 to 9 kN, since this is more dependent on concrete strength than on the reinforcement. The yield loads are dependent on the steel core strength, steel core diameter, and (to a smaller extent) the skin type and thickness. The beam yield loads did not vary much due to the type or thickness of FRP skin because the stress in the hybrid rod in this stage is more dependent on the yield strength of the steel core. The yield loads had ranges of 16 to 19 kN for the rods with a 9.0 mm core, and 36 kN for the rods with a 13.0 mm core. The deflection at steel core yield is the same for all of the beams, approximately 3.5 mm.

The ultimate loads and deflections, as given in Table 11, show that varying the type and thickness of FRP skin has considerable influence. The load-deflection curves in Figures 24 and 25 show that increasing

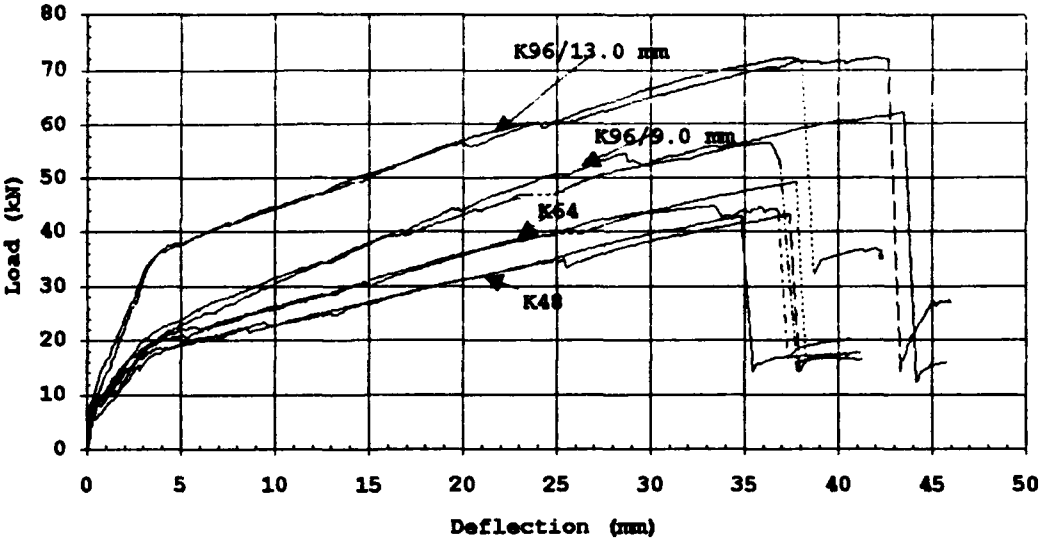


Figure 24. Combined Load-Deflection Curves of Beams with Aramid Hybrid Rods

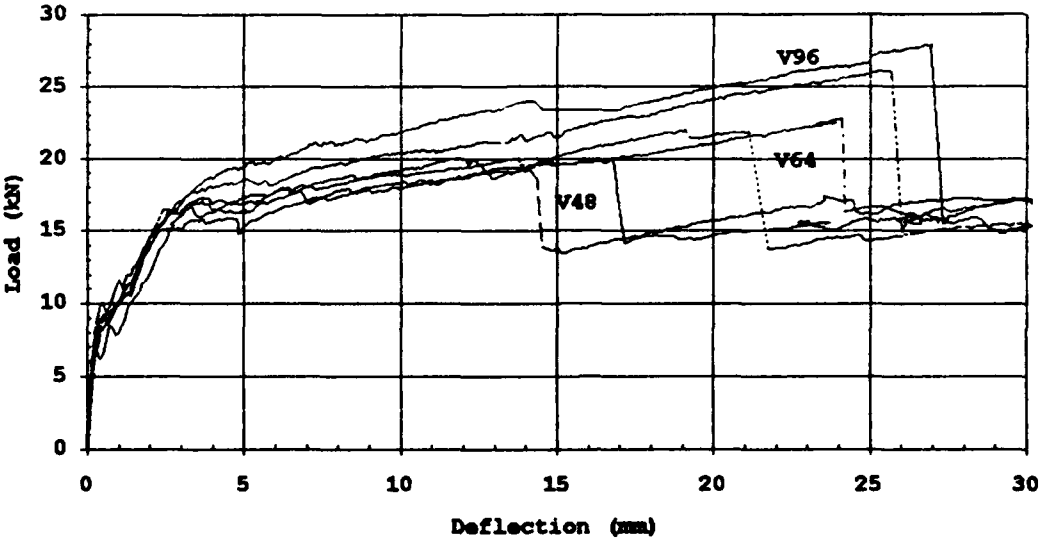


Figure 25. Combined Load-Deflection Curves of Beams with Vinylon Hybrid Rods

the amount of FRP skin on the hybrid rod increased the load at failure of the beam. This increase in load with increased FRP skin is expected because the tensile tests revealed that stress at failure of the hybrid rods is directly proportional to the skin thickness of the FRP.

The failure mode of beams with either vinylon or aramid hybrid rods was the same, rupture of the FRP skin. As the beam deflected and cracked, stress/strain concentrations are induced in the bar at crack openings (evaluations of the stress/strain concentrations is difficult because of debonding). When the stress/strain at a crack reached the ultimate stress/strain of the FRP skin, the skin failed suddenly. Consistently, the location of skin failure occurred at the placement of a stirrup. After the FRP skin failed, the beam was still able to maintain a load due to the presence of the steel core. Figure 26 is a photo of a beam failure crack.

Figure 26. Failure Crack

When comparing the experimental curves to the theoretical curves, the beams behaved close to the predicted values with only slight differences. Figures 27 and 28 are two of the load-deflection curves showing both experimental and theoretical data. The remaining curves are contained in Appendix B.

Up to cracking, the theoretical curve follows the experimental curve almost exactly. After cracking, the curves have approximately the same slope, even though the yield point of the experimental beam is higher than that of the theoretical beam. This difference can be attributed to the values of $f_y$ assumed in the calculations. After the yielding of the steel core, the slope of the theoretical beam is greater than the experimental beam. This shows that there is a loss of bond between the hybrid rod and concrete, which is not considered in theoretical calculations. While the cracking and steel yield points on the load-deflection curve can be predicted fairly accurately, the ultimate load and deflection is harder to predict. This due to the use of an assumed ultimate concrete strain ($\varepsilon_u$= 0.0035) and the influence of the cracking pattern on the compressive strength.

## 5.2 BEAMS WITH #5 REBAR AND SMOOTH 13.0 mm ROD

Figure 29 shows the load-deflection curves for the beams with conventional steel reinforcement (#5 rebar).

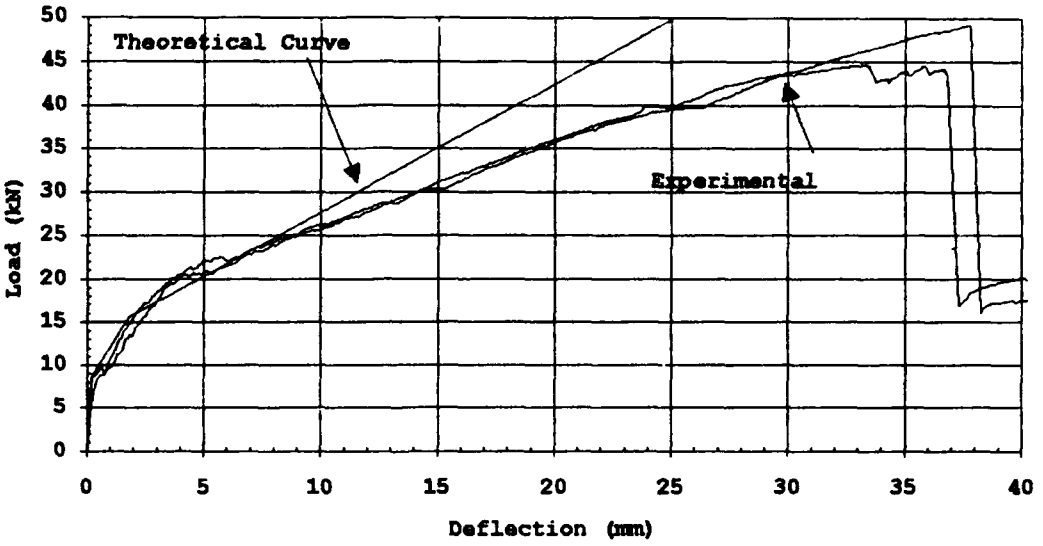


Figure 27. Experimental and Theoretical Load-Deflection Curves for K64/9.0 mm

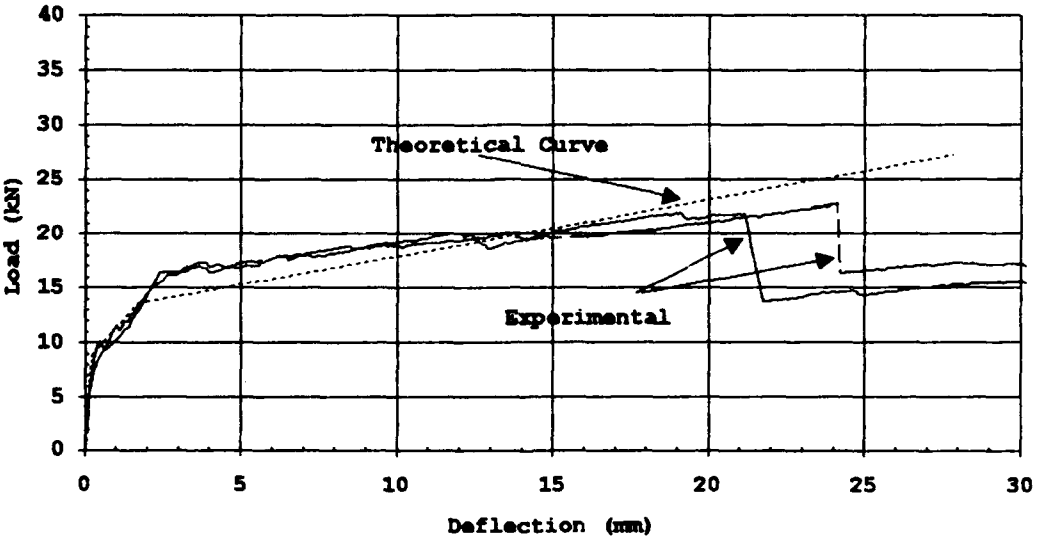


Figure 28. Experimental and Theoretical Load-Deflection Curves for V64/9.0 mm

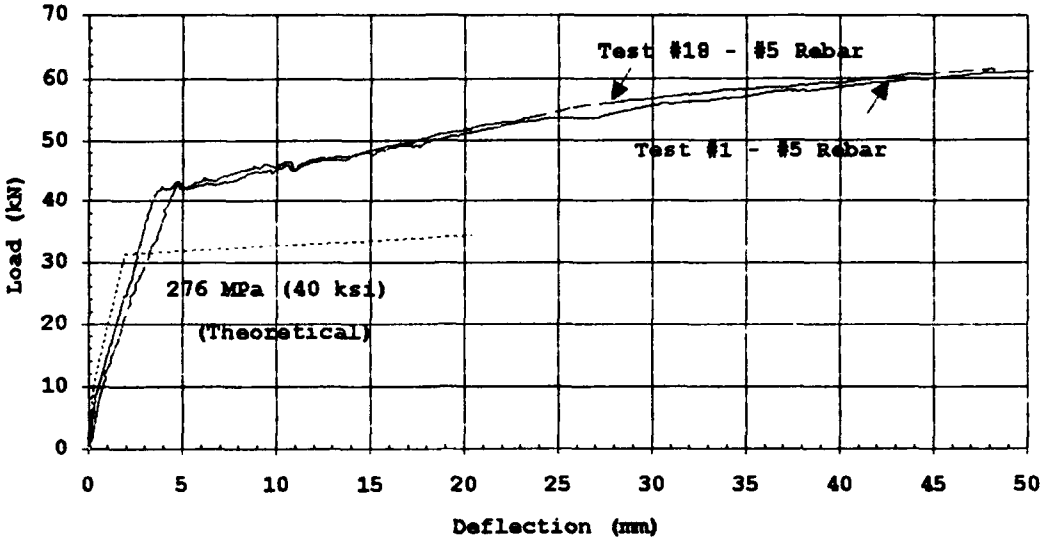


Figure 29. Load-Deflection Curves for Beams #5 Rebar

The load-deflection curves for the beams reinforced with the #5 rebar displayed the three stage pattern that is common for beams with conventional reinforcement. The cracking and yield loads are clearly defined, followed by a significant decrease in slope after steel yielding. After concrete cracking load, the slope of the experimental curve becomes slightly less than the theoretical curve due to a decrease in bond, and the presence of flexural cracks. This difference is expected since the theoretical curves assume perfect bond between the bar and concrete.

The difference between the experimental and theoretical yield loads is due to the actual tensile strength of the steel being greater than the assumed nominal strength used in the theoretical calculation. The difference between the experimental and theoretical ultimate load

and deflection cannot be adequately explained without knowing the actual strains on the bar and concrete. It can be speculated that the steel is in a state of strain hardening. The exact position of the reinforcement may also play a role in the difference between experimental and theoretical data.

The load-deflection curve, Figure 30, for the plain 13.0 mm rod is interesting because it shows the complete loss of bond between the bar and the concrete. Up through the cracking load, the experimental curve closely follows the theoretical curve. After cracking, at about 12 kN, the slope (flexural stiffness) of the experimental curve suddenly decreases. This indicates the loss of bond between the rod and the concrete. A lower flexural stiffness is expected if the rod becomes unbonded because the tensile stress is now distributed throughout the length of the rod instead of the bond transfer length (as in the case of a bonded bar). At approximately 28 kN, there is a flattening of the curve that indicates anchorage failure at one end of the beam. The lack of bond caused all the stress in the rod to be transferred to the anchors. Even with a wire cage used to confine the concrete around the anchors (See Appendix B, Figure B8), the concrete capacity was overcome. Figure 31 shows the anchorage failure of the beam reinforced with a smooth 13.0 mm rod.

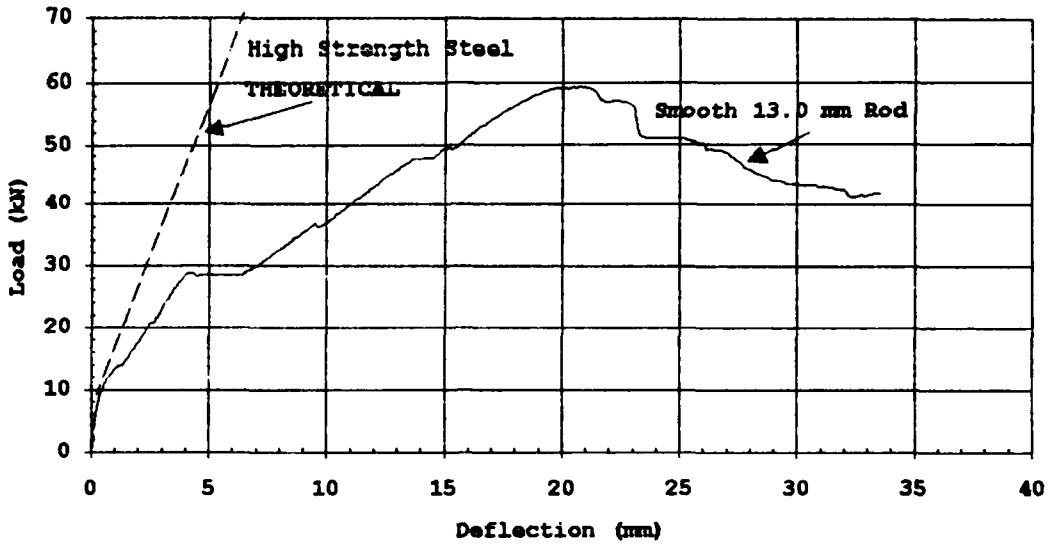


Figure 30. Load-Deflection Curve for Smooth 13.0 mm Rod

Figure 31. Failed Anchorage, Smooth 13.0 mm Rod

## 5.3 CRACKING PATTERN OF TEST BEAMS

The cracking pattern of a beam depends on the type and amount of reinforcement and the bond. As the beam is loaded, cracks occur on the tension face of a beam when the ultimate tensile stress/strain of the concrete is reached. After the beam cracks, the tensile stress in the concrete is transferred to the reinforcement through the bond forces between the concrete and the bar. The spacing of the cracks is dependent on the bond forces that can be developed. If the bond forces are high, the crack spacing will be small because the length needed to transfer the stress between the concrete and bar is shorter. Therefore, bars which provided a good concrete bond had small crack width and spacing than bars with lower bond.

From Table 12 and the beam crack pattern tracings contained in Appendix B, it is evident that the #5 rebars had a better bond than the hybrid rods. The beams with #5 rebar had more primary cracks (6 to 8) and lower average crack spacing (102 mm to 107 mm) than the beams with hybrid rods, (4 to 7) and (102 mm to 170 mm) respectfully.

### 5.3.1 Flexural Crack Width

While crack width was not measured during the beam testing, it is important to understand the work that has been done in the area of crack width and spacing for beams reinforced with FRP rods. Bresler and Watstein (197[illegible]) experimented on steel reinforced concrete beams and found that the average crack spacing value is about twice the cover thickness as measured to the center of the reinforcing rebar. ACI 224.2R-86 reported that the expected value of the maximum crack

spacing is about twice that of the average crack spacing. Therefore, according to ACI 224.2R-86, crack width may be estimated by multiplying the maximum crack spacing with an average strain in the reinforcement. The committee recommended using the Gergely-Lutz expression for predicting crack width, this expression is given below:

$$W_{max} = 0.076\,\beta f_s \sqrt[3]{d_c A} \times 10^{-3} \text{ (in)} \qquad (4.1)$$

where,

$\beta$ = Ratio of distances to the neutral axis from the extreme tension fiber and from the centroid of the main reinforcement.

$d_c$ = Cover thickness measured to center of bars (in).

$f_s$ = Maximum stress in the reinforcement at service load level (psi).

A = The effective tension area of concrete surrounding the principal reinforcement divided by the number of rebars ($in^2$).

This equation is based on the use of steel reinforcement. The current ACI 224.2R-86 mathematical expression for predicting crack spacing and crack width cannot be used directly for FRP reinforcement.

In work done by Faza and GangaRao (1991) on bending and bond behavior of glass FRP (GFRP) rebars, two expressions were developed to predict crack widths. The first one is based on the Gergely-Lutz expression. To account for the difference in rigidity between GFRP rods and steel rebar, they assumed the elastic modulus of the GFRP rod

($E_{FRP}$) to be 1/4 that of the steel rebar ($E_s$), and adjusted the formula accordingly ($E_{FRP} = E_s/4$).

$$W_{max} = 0.3\beta f_f \sqrt[3]{d_c A} \times 10^{-3} \quad \text{(in)} \tag{4.2}$$

where,

$f_f$ = FRP stress (psi)

The second expression is based on work done by Bresler and Watstein (1974). In this expression, the relationship between the tensile strength of concrete, the bond strength and crack spacing, leads to the crack width. First, the crack spacing is found from the following expression:

$$l = (2f_t A) / (\mu_m \pi D) \tag{4.3}$$

where,

$f_t$ = tensile strength of concrete

$\mu_m$ = maximum bond stress

D = rebar diameter

Once the crack spacing is computed, the crack width is approximated by an average strain in a FRP rebar multiplied by the crack spacing:

$$W_{max} = (f_f / E_f) l \tag{4.4}$$

From equations 4.3 and 4.4, GangaRao and Faza derived the expression:

$$W_{max} = 0.14 f_f \frac{2f_t'}{\mu_m} \frac{A}{\pi D} \times 10^{-3} \quad \text{(in)} \tag{4.5}$$

where,

$$f_t' = 7.5\sqrt{f_c'} \tag{4.6}$$

$f_f$ = Maximum stress (ksi) in FRP reinforcement at service load level

Faza and GangaRao found that the second expression, equation 4.5, was closer in predicting the experimental crack widths, as long as the values for bond stress can be accurately predicted. They suggest that to better predict crack width and spacing, more experimental data on actual bond strength of FRP rods is needed.

### 5.3.2 Flexural Crack Spacing

For a comparison, crack spacing using equation 4.3 is calculated for the test beams in this project. Since no bond stress data is available for hybrid rods, the maximum bond stress is obtained from tests done by Tanigaki (1991) on braided FRP rods. Figure 32 is a graph of the results (bond stress verses slip) for different bars (K - kevlar, C - carbon, S - sand coated, and D10 - deformed steel rebar with 10 mm diameter).

The specific bond strengths at 0.0 mm and 3.0 mm slip for the K96 bar in Figure 32 are assumed for all the hybrid rods, 25 kgf/cm$^2$ (2.45 MPa) and 125 kgf/cm$^2$ (12.3 MPa), to obtain a range of crack spacing.

The bond stresses for the conventional (#5) rebar is assumed from the maximum and minimum of the D10 curve, 40 kgf/cm$^2$ (3.92 MPa) and 135 kgf/cm$^2$ (13.2 MPa). The results are given in Table 13.

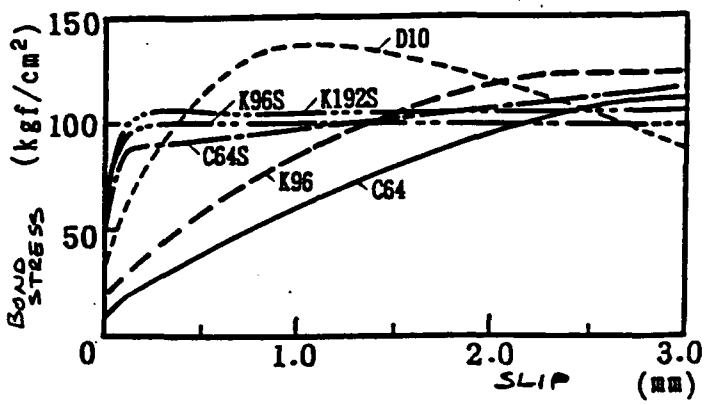


Figure 32. Bond Stress vs. Slip (Tanigaki 1991)

From Table 13, it is apparent that assuming the correct bond stress is critical in predicting crack spacing and crack width. When 0.0 mm (minimum bond stress) slip is assumed, the predicted crack spacing is 250% to 350% greater than the experimental. When 3.0 mm (maximum bond stress) is assumed the predicted crack spacing is 20% to 40% less than the experimental. Bresler and Watstein (1974) even state that because of the difficulties associated with the definition of a "bond-slip" law, empirical values of crack spacing based on statistical studies might be more useful.

Table 13. Theoretical and Experimental Crack Spacing

| Reinforcement Type | Cracking Spacing, (mm) | | |
|---|---|---|---|
| | Theoretical | | Experimental |
| | @Minimum Bond Stress | @Maximum Bond Stress | Average of Two Beams |
| K48/9.0 mm | 644 | 129 | 158 |
| K64/9.0 mm | 616 | 123 | 120 |
| K96/9.0 mm | 558 | 111 | 145 |
| V48/9.0 mm | 628 | 125 | 171 |
| V64/9.0 mm | 594 | 119 | 139 |
| V96/9.0 mm | 538 | 107 | 139 |
| K96/13.0 mm | 450 | 90 | 108 |
| #5 Rebar | 281 | 83 | 102 |

### 5.3.3 Longitudinal Cracks

The longitudinal cracks that occurred, indicate the presence of radial stresses around the hybrid rods. The longitudinal cracks occurred in all beams with the aramid hybrid rods and one beam with a vinylon hybrid rod (Test #15 - V64/9.0 mm). Figure 33 shows a test beam with longitudinal cracks.

For longitudinal cracks in steel reinforced beams, Bresler and Watstein (1974) describe that at low stress levels the reinforcement high principal stresses occur only at the interface, zones adjacent to the full transverse cracks, where local inclined cracking occurs. The high tension is relieved by local cracking near the ends. The local cracking also shifts the zone of maximum principal stress inward from the transverse crack face. As the load increases, additional internal cracks

develop due to the stresses reaching the tensile strength of the concrete. With further increase in load, the internal cracks continue to propagate creating teeth-like segments that resist the pullout forces by wedging action. Figure 34 shows the two classical bond failure modes for conventional steel reinforcement; splitting failure and pull-out failure.

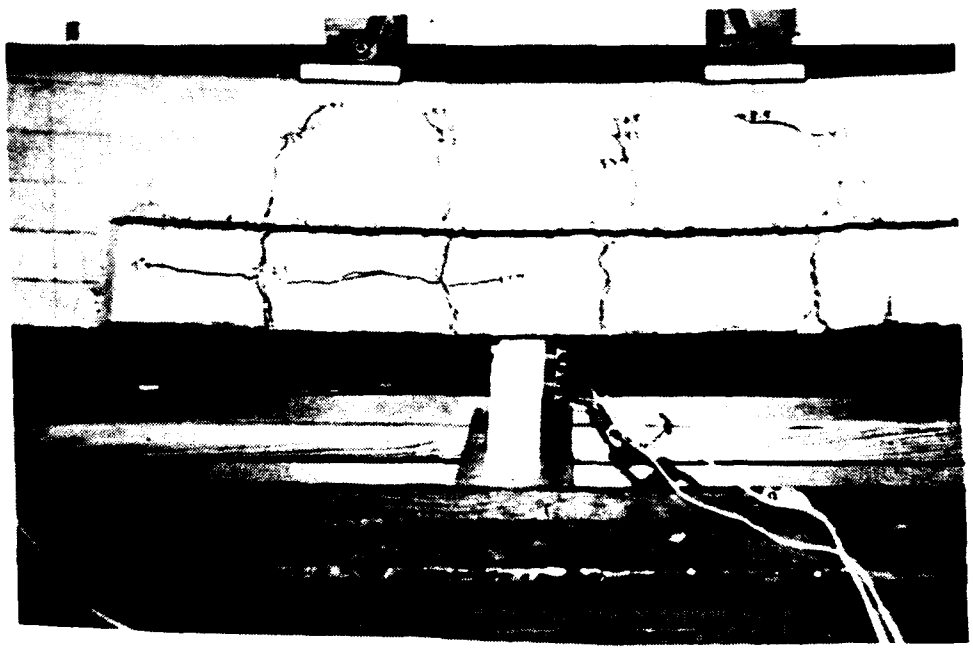

Figure 33. Photo of Longitudinal Cracks

In the beams reinforced with FRP or hybrid rods, the cause of the longitudinal cracks may be different from that of steel reinforced beams. For steel rebars, the elastic modulus ($E_s$) is the same in both the transverse and longitudinal directions and is considerably higher than $E_c$ of concrete. For FRP or hybrid rods with FRP skin, the elastic modulus in the transverse direction ($E_{FRP,t}$) is significantly less than the elastic modulus, in the longitudinal direction ($E_{FRP,l}$). In the longitudinal direction, the fiber tensile modulus ($E_f$) controls the elastic modulus ($E_{FRP,l}$) of the rod. In the transverse direction, the matrix (resin) elastic modulus ($E_r$) controls the modulus ($E_{FRP,t}$) of the rod. Since the elastic modulus of concrete ($E_c$) is approximately five times larger than the elastic modulus ($E_m$) of an epoxy resin matrix, local crushing of the surrounding concrete should not occur as shown schematically in Figure 34. Instead, as a FRP (or hybrid) rod slips, the surface of the rod deforms to match the preexisting deformed concrete interface around the rod. Figure 35 shows that as the rod slips, a large internal pressure is created. This internal pressure causes radial stresses to form in the concrete surrounding the rod and is responsible for the split cracking.

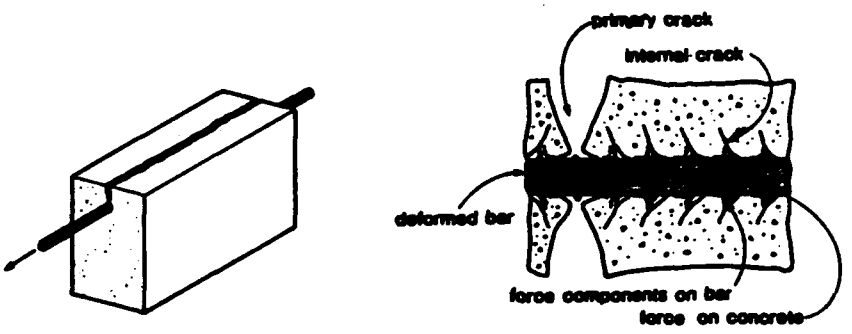


(a) Splitting failure and internal cracking

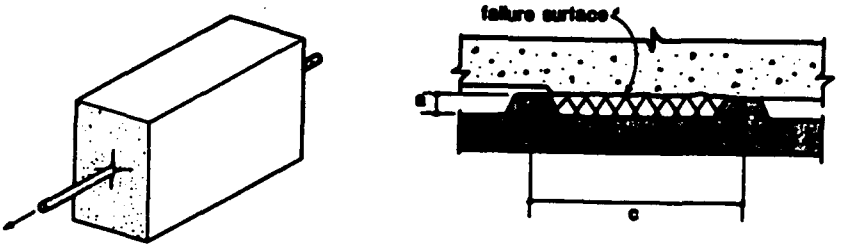


(b) Pullout failure and closeup of failure surface

Figure 34. Two Classical Bond Failure Modes (Abrishami and Mitchel 1992)

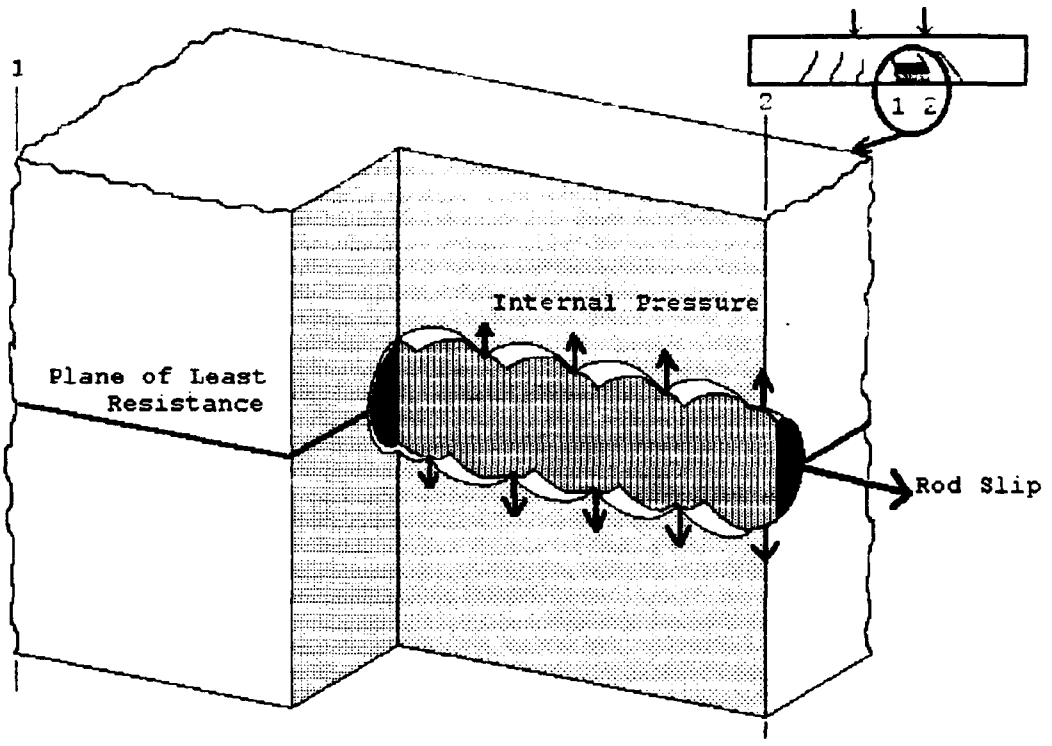


Figure 35. Concrete Section

When the radial stresses reach the tensile strength of the concrete, internal cracks are formed which may propagate to the surface (split cracks). If the load is high enough, as in the case of the beams with the aramid hybrid rods, a longitudinal crack will form on a plane of least resistance, as shown is Figure 35.

## 5.4 CONCLUSIONS

The beam test provided an understanding of the behavior of beams reinforced with a hybrid rod. The following are the main findings from the beam tests:

- The shape of the load-deflection curve for hybrid reinforced beams can be predicted based on common reinforced concrete assumptions and the tensile behavior of the hybrid rods. Analytical calculations of cracking load, steel yield load and ultimate load were used to developed theoretical curves that matched the shape of the experimental curves. The difference between the theoretical and experimental curves was due to the loss of bond between the rod and concrete.
- Beams reinforced with hybrid rods had fewer cracks and a greater spacing between cracks than beams reinforced with conventional steel reinforcement. This is most likely due to the bond strength of hybrid rods being less than the bond strength of conventional steel.
- Longitudinal cracks occurred in beams reinforced with aramid hybrid rods. The longitudinal cracks are possibly due to the internal forces in the concrete that are created when the rod slips, and the FRP skin deforms to match the existing concrete interface. The transverse strength of the FRP skin is significantly less than the strength of the concrete.
- After failure of FRP skin, beams were still able to sustain load at the steel core yield load. When the FRP skin fails, a segment of the skin becomes unbonded from the steel core. There is no way of knowing the length of this unbonding, but it cannot be the full length of the bar due to the ability of the beam to sustain a load after skin failure (there is still stress transfer through the FRP skin to the concrete).
- Beams reinforced with aramid hybrid rods had a greater ultimate load than beams with vinylon hybrid rods. This is expected, since the

stiffness and strength of aramid is significantly greater than vinylon fibers.

# CHAPTER 6

# SUMMARY AND RECOMMENDATIONS

## 6.1 SUMMARY

The following is a summary of the conclusions found in the uniaxial tensile tests and concrete beam tests.

### 6.1.1 Uniaxial Tensile Tests

- Hybrid rods allow tailoring the stress-strain behavior of concrete reinforcement by varying FRP skin material, FRP skin thickness, steel core diameter, and steel core strength.
- By using the law of mixtures, the tensile behavior of the hybrid rods can be predicted.
- The typical stress-strain curve of a hybrid rod has a bi-linear behavior, which means, that after the steel yields, the FRP skin provided additional strength.

### 6.1.2 Beam Tests

- The shape of the load-deflection curves can be predicted for beams reinforced with hybrid rods based on the tensile behavior of the hybrid rods.

- Beams reinforced with hybrid rods had fewer cracks which were further spaced than beams reinforced with conventional reinforcement.
- Beams reinforced with kevlar hybrid rods had longitudinal cracks.
- After failure of the FRP skin, the beam was still able to sustain a load at the yield load of the steel core.
- Beams reinforced with kevlar hybrid rods had a greater ultimate load than beams with vinylon hybrid rods.

## 6.2 RECOMMENDATIONS

While this project was intended to be a preliminary evaluation of hybrid reinforcement, it did provide some key insight as to the behavior of hybrid rods. There are a number of questions that still need to be answered. The following is a list of areas where further research is needed to better understand the physical and mechanical behavior of hybrid reinforcement:

- Further study in the area of durability of FRP reinforcement. Long term studies of FRP reinforcement in actual use is needed. How does an FRP element that is stressed behave in a corrosive environment?
- The use of hybrid rods as a prestressing element needs to be addressed. Hybrid rods with high strength steel core could provide excellent prestressing tendon, but the issues of stress-strain behavior, prestress losses, bond strength, and anchorage requirement need to be studied.

- The bond between FRP skin and core. The mechanics of the stress transfer is not clearly understood. Further detailed study into the actual mechanism of stress transfer is needed. Finite element modeling could be done to better understand the behavior of the hybrid components (i.e. core material, fiber, and resin matrix). Research needs to be done on how the physical properties of the hybrid components affect the bond (i.e. the effect of changing the properties of the resin matrix), and is the resin matrix the key to the bond performance. Another issue that needs to be answered is what happens to the bond after the FRP skin fails. Is the bond lost over the whole length of the rod or is it lost is just a segment where the skin fails?
- The bond between FRP rod and concrete. There has been numerous studies involving the bond of FRP rods. All of the studies have shown that the bond strength of FRP rods is less than that of conventional steel. One proposal to improve the bond of FRP rods has been the use of sand coating.
- A more detailed investigation of the stresses in the hybrid rod at failure is needed. The main problem in this area is how to attach strain gages to a braided FRP rod. The fibers lie at angles to the longitudinal axis of the rod due to the braiding process. Another problem is that strain gages attached to the surface only measure the surface strain. Since a hybrid rod is composed of different materials, the strain cannot be constant across the cross-section as in the case of a steel rod.

- Hybrid rods made for different combinations of FRP materials need to be studied. Instead of using a steel core, other FRP materials could be used to tailor the performance of the reinforcement to a specific application. This area holds the most promise for the use of FRP reinforcement in concrete.
- For hybrid reinforcement to be used as a concrete reinforcement, not only do design procedures need to change but also design philosophy. Hybrid and FRP reinforcement cannot be used in the same manner as steel is used in concrete. FRP is a completely different material, therefore to optimize its use, it has to be applied differently. FRP reinforcement cannot be used as a one-to-one replacement of steel reinforcement.
- The issue of crack width for structures reinforced with FRP or hybrid reinforcement needs further study. While crack width is not a problem in terms of corrosion for FRP rods, it could be a problem in terms of aesthetics. People in general are not comfortable is seeing large cracks in concrete structures. New methods of improving the bond performance of FRP rods need to be developed to decrease the crack width.

# APPENDIX A

## UNIAXIAL TENSILE TEST DATA

A-1. Photos of Test Rods

A-2. Load-Strain Curves for Rods Tested

A-3. Stress-Strain Curves for Rods Tested

Figure A1. Photo K48/9.0 mm/SR24

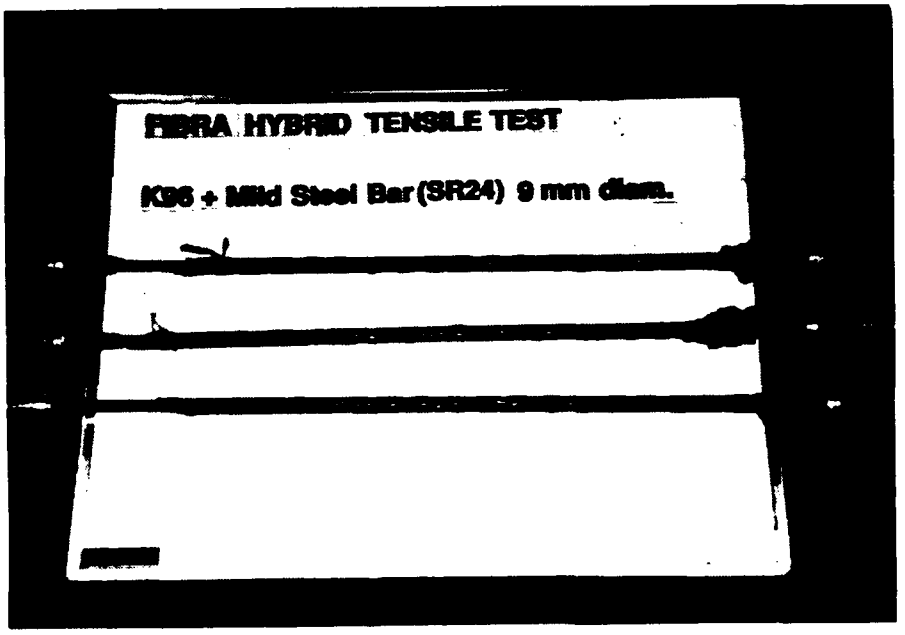


Figure A2. Photo K96/9.0 /SR24

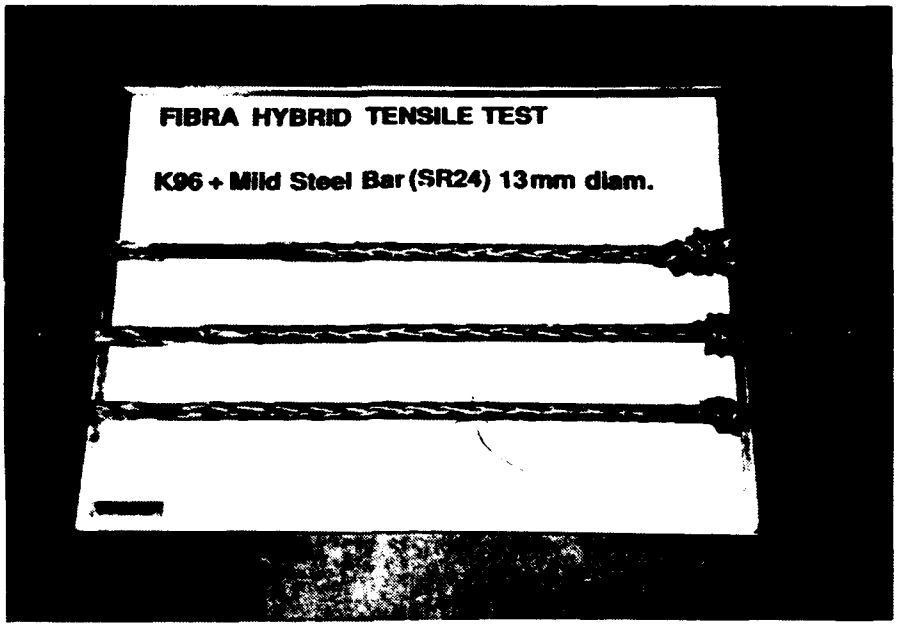


Figure A3. Photo K96/13.0 mm/SR24

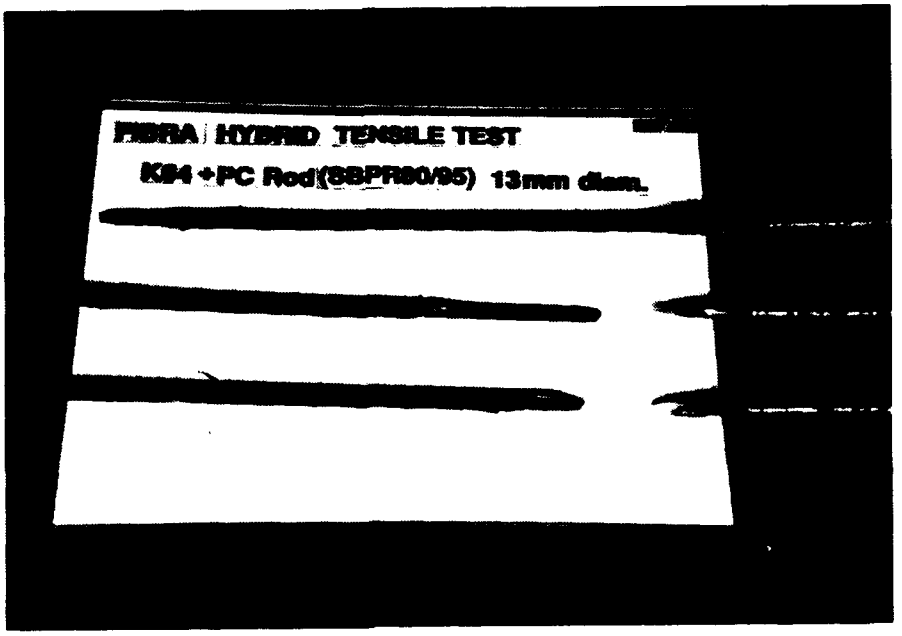


Figure A4. K64/13.0 mm/SBPR80

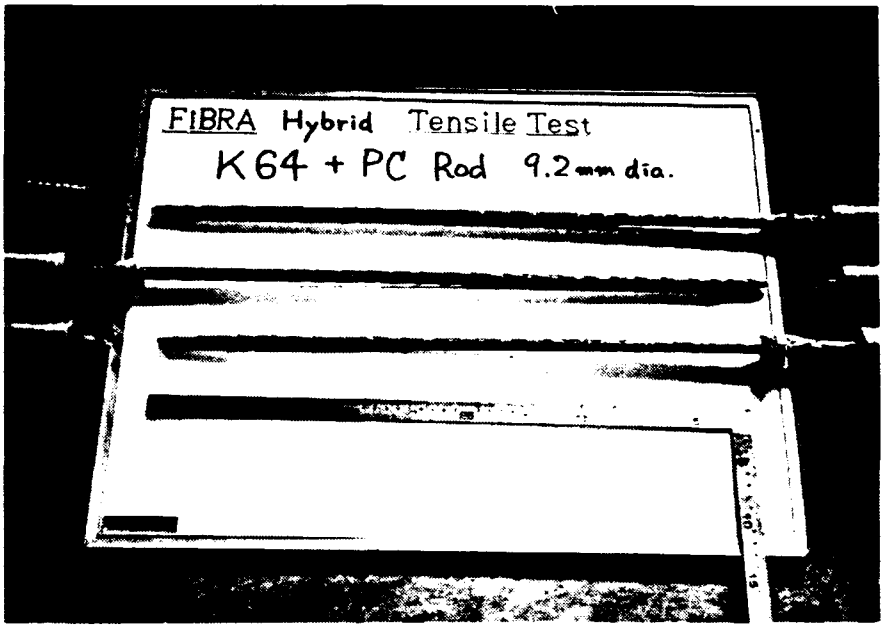


Figure A5. Photo K64/9.2 mm/SBPR80

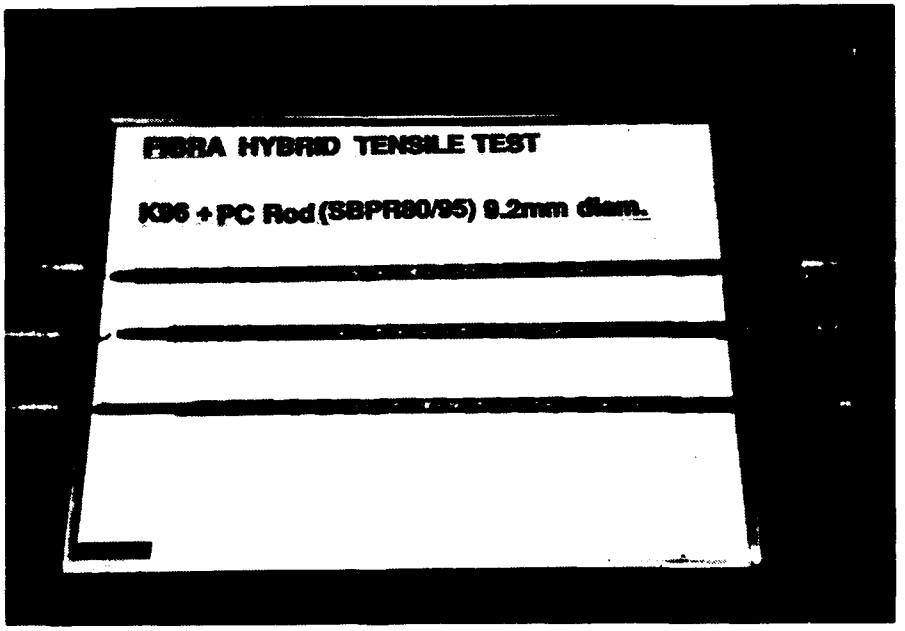


Figure A6. Photo K96/9.2 mm/SBPR80

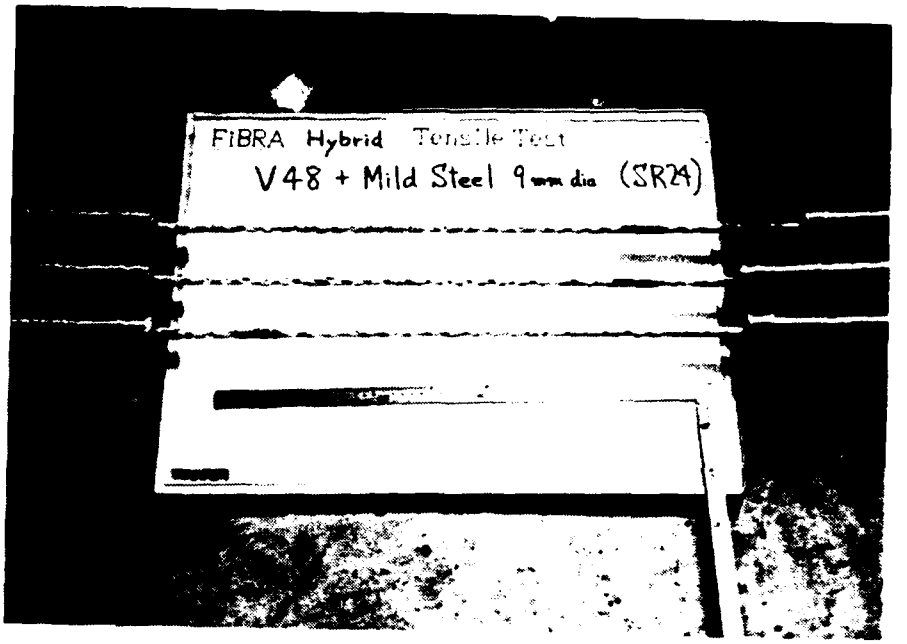


Figure A7. Photo V48/9.0 mm/SR24

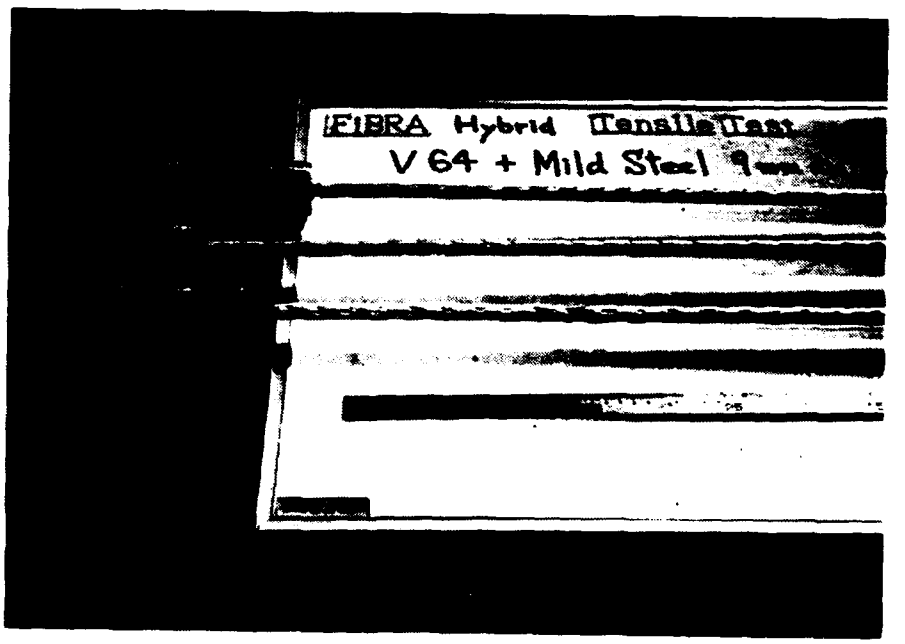


Figure A8. Photo V64/9.0 mm/SR24

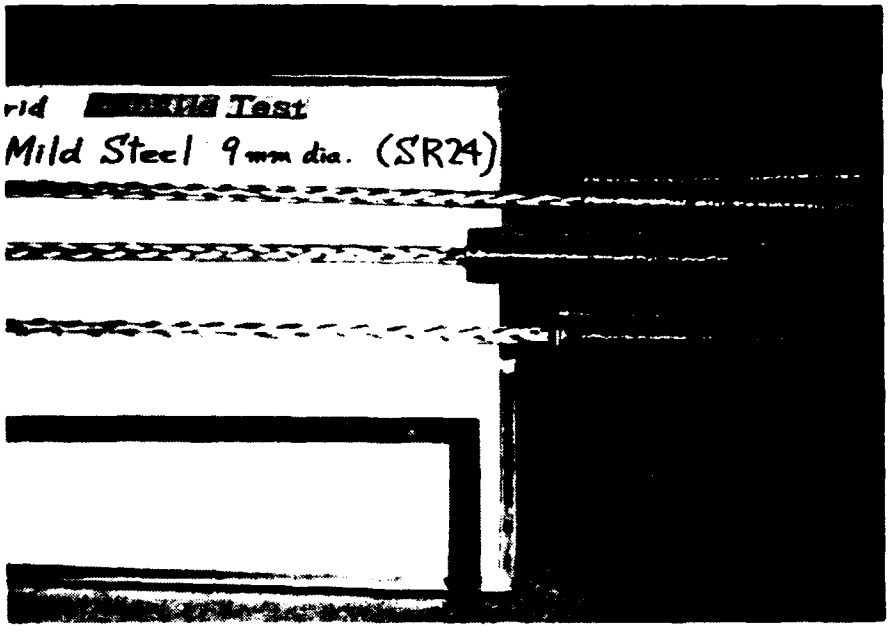


Figure A9. Photo V64/9.0 mm/SR24

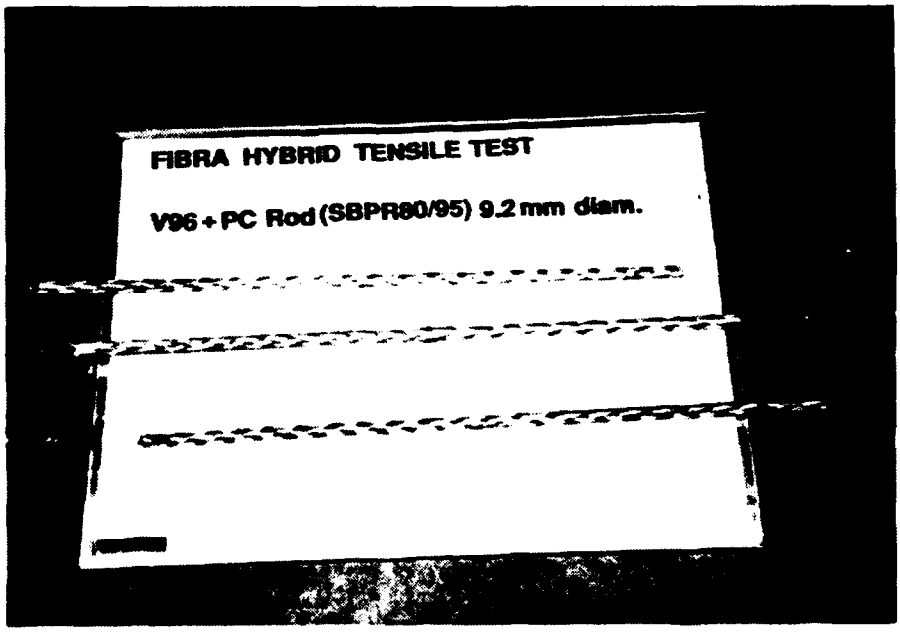


Figure A10. Photo V96/9.2 mm/SBPR80

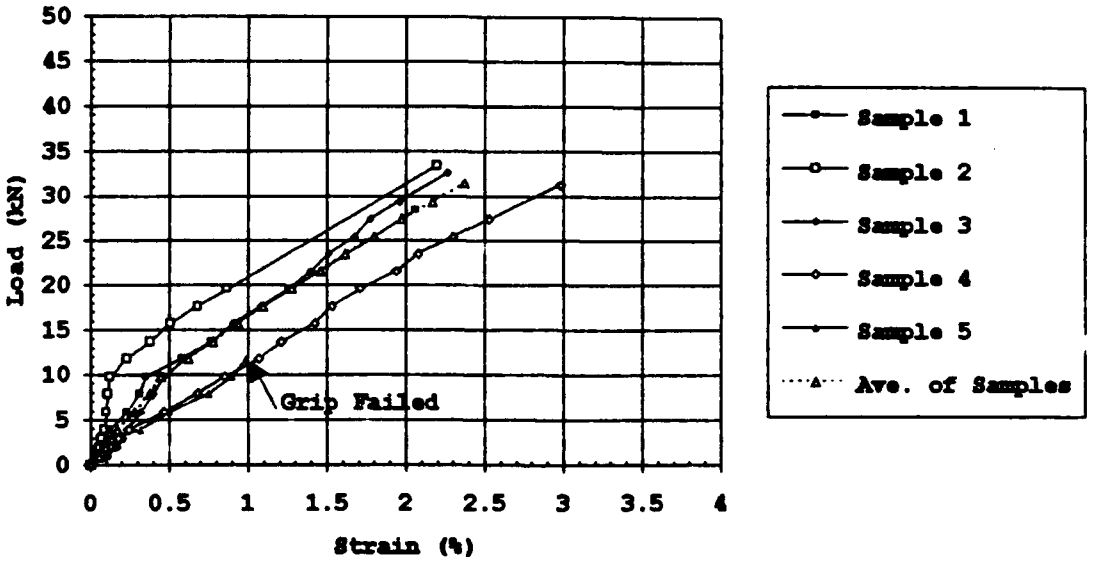


Figure A11. Load-Strain Data for K32/3.0 mm (Mild Strength Steel)

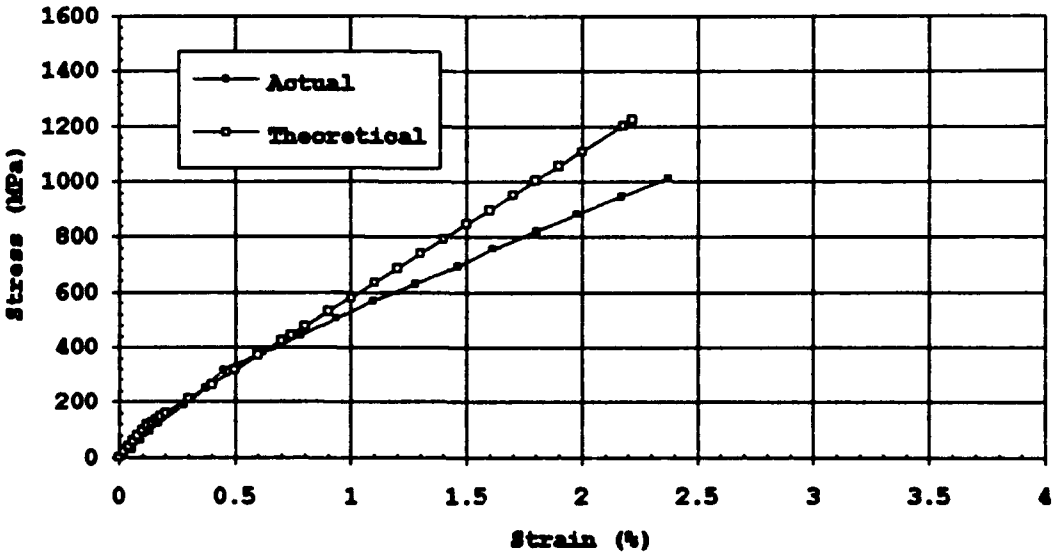


Figure A12. Stress-Strain Curve K32/3.0 mm (Mild Strength Steel)

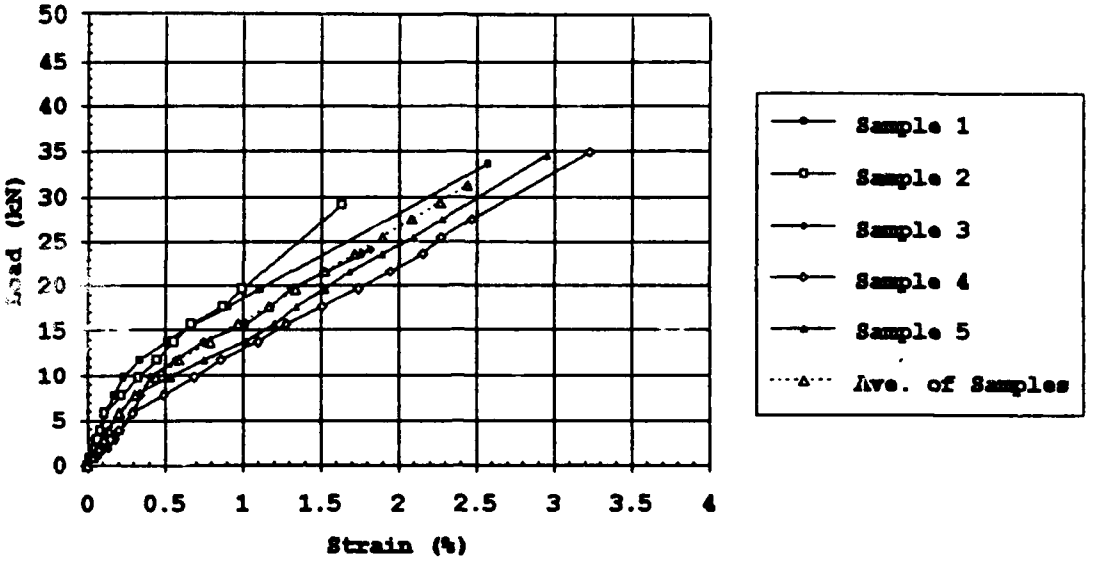


Figure A13. Load-Strain Data: K32/4.0 mm (Mild Strength Steel)

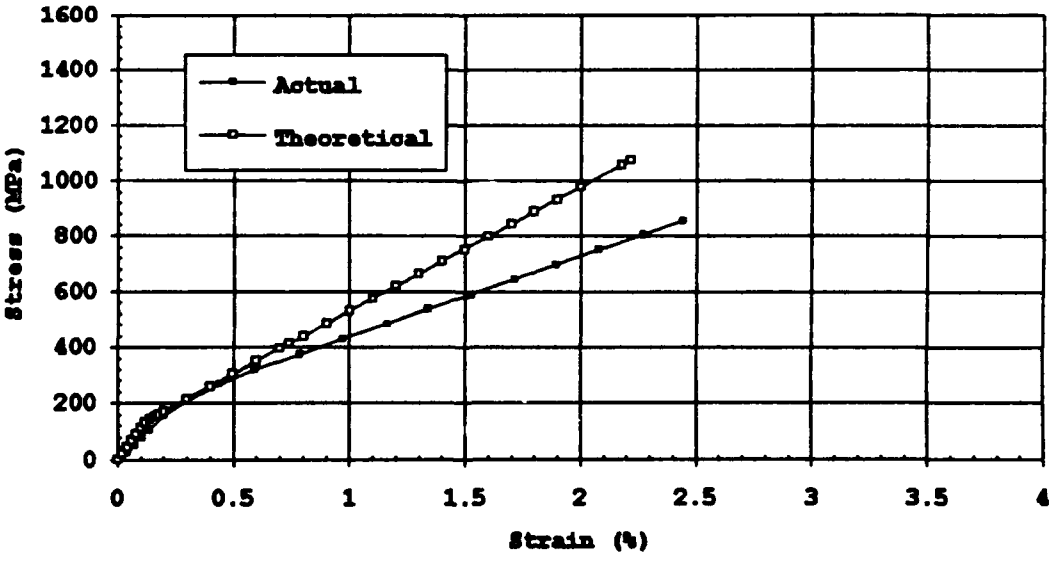


Figure A14. Stress-Strain Curve: K32/4.0 mm (Mild Strength Steel)

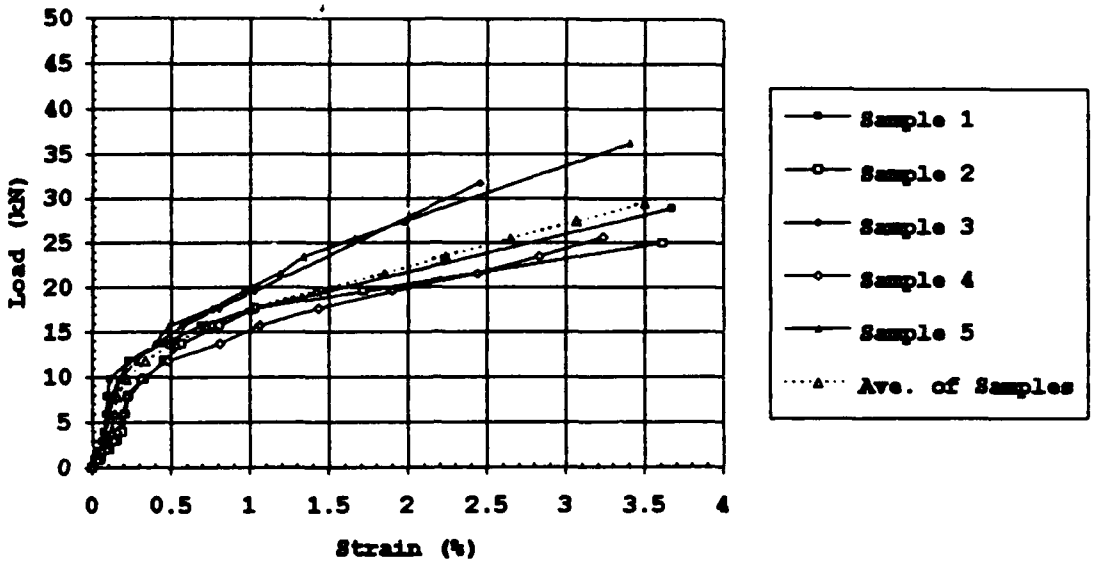


Figure A15. Load-Strain Data: K32/6.0 mm (Mild Strength Steel)

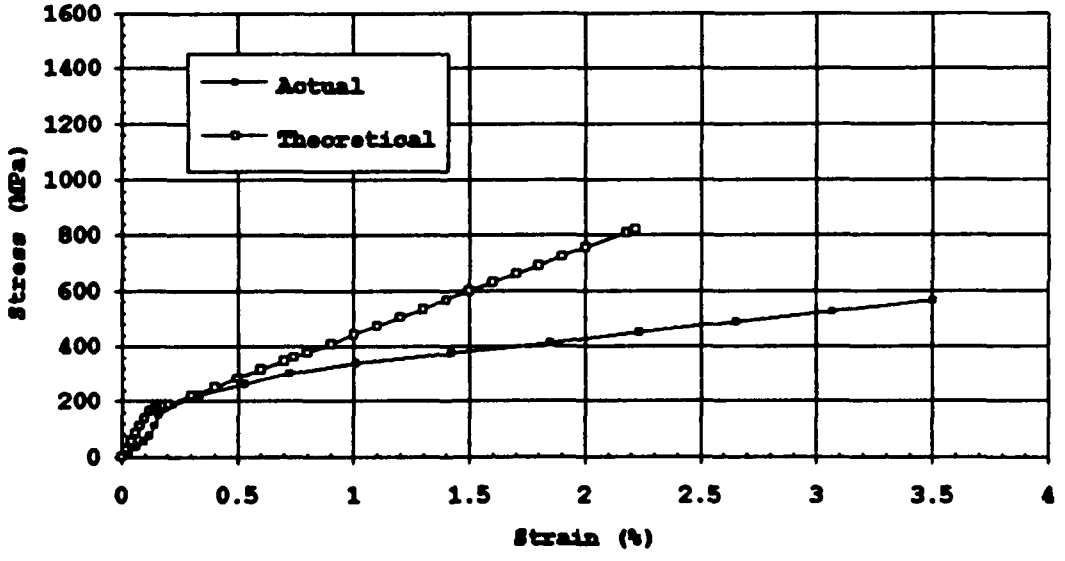


Figure A16. Stress-Strain Curve: K32/6.0 mm (Mild Strength Steel)

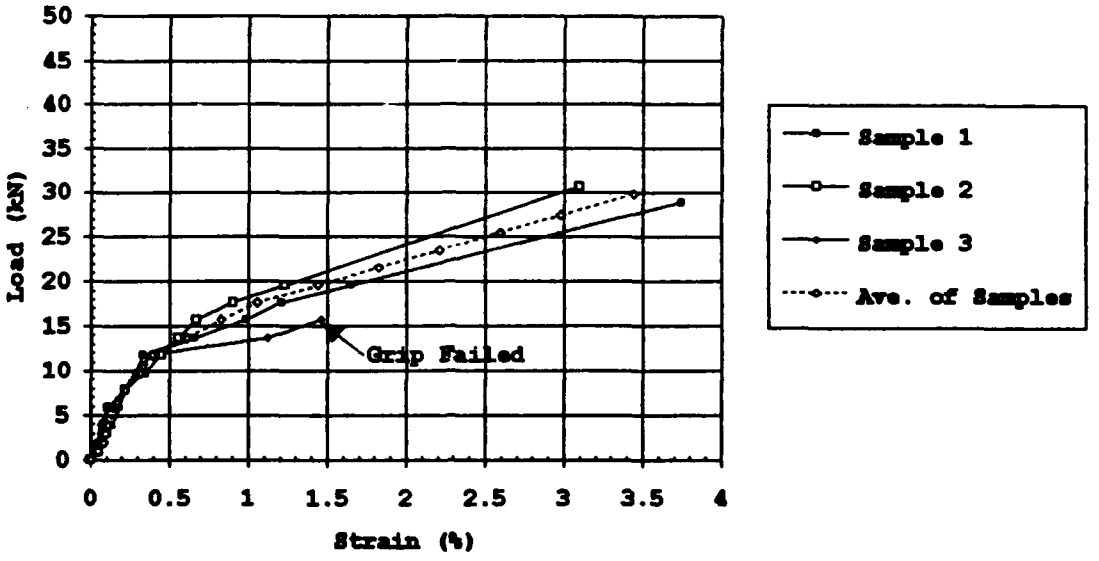


Figure A17. Load-Strain Data: K32/6.0 mm Threaded (Mild Strength Steel)

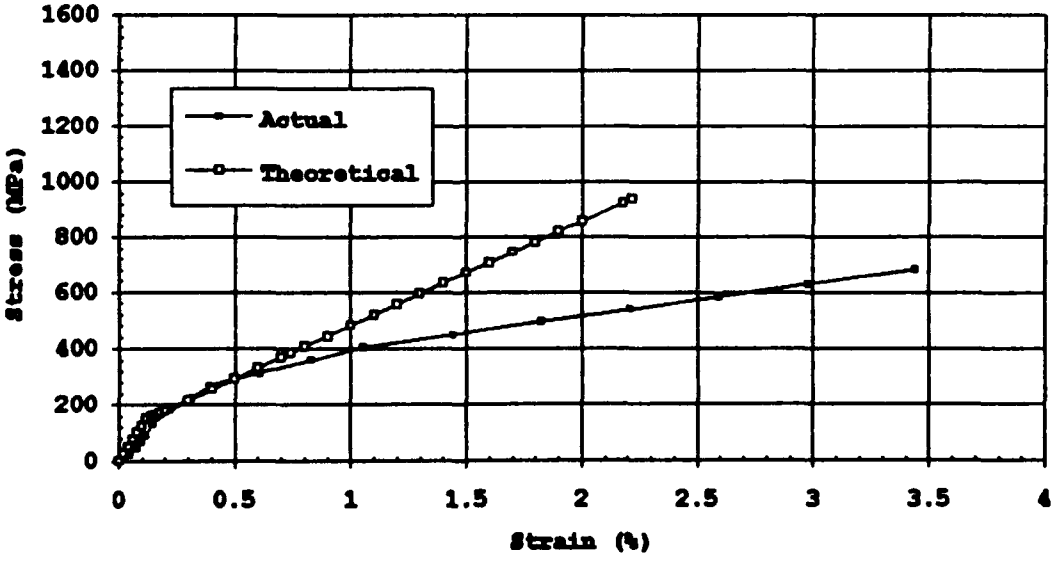


Figure A18. Stress-Strain Curve: K32/6.0 mm Threaded (Mild Strength Steel)

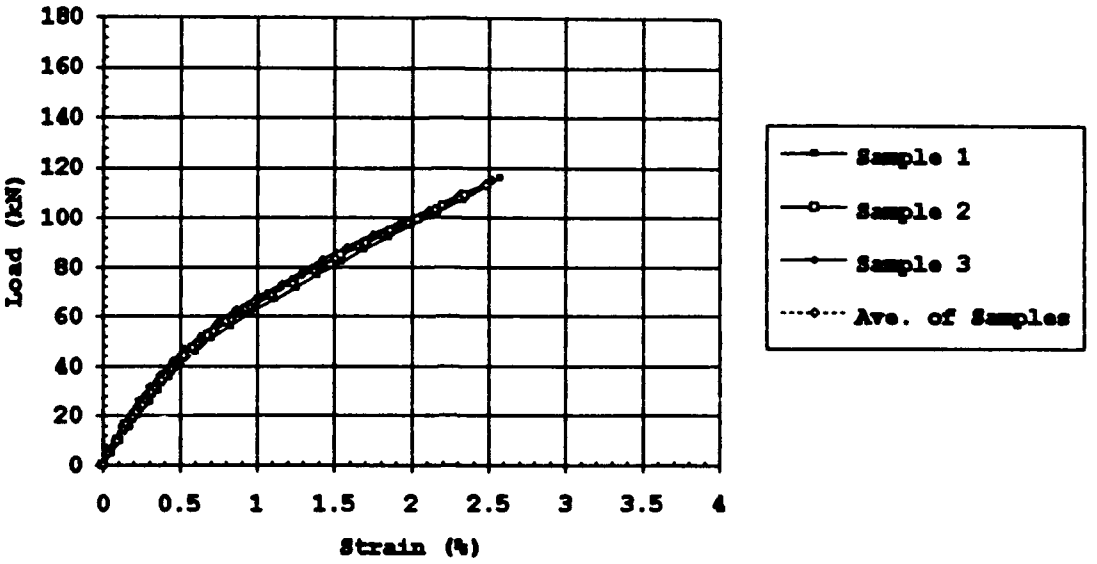


Figure A19. Load-Strain Data: K64/6.0 mm/PC Wire Core

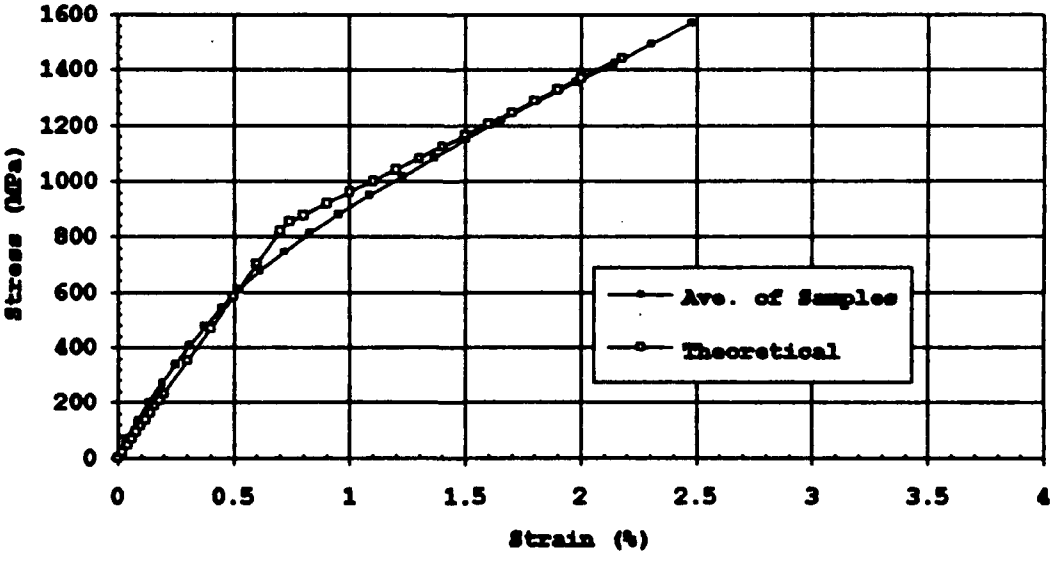


Figure A20. Stress-Strain Curve: K64/6.0 mm/PC Wire Core

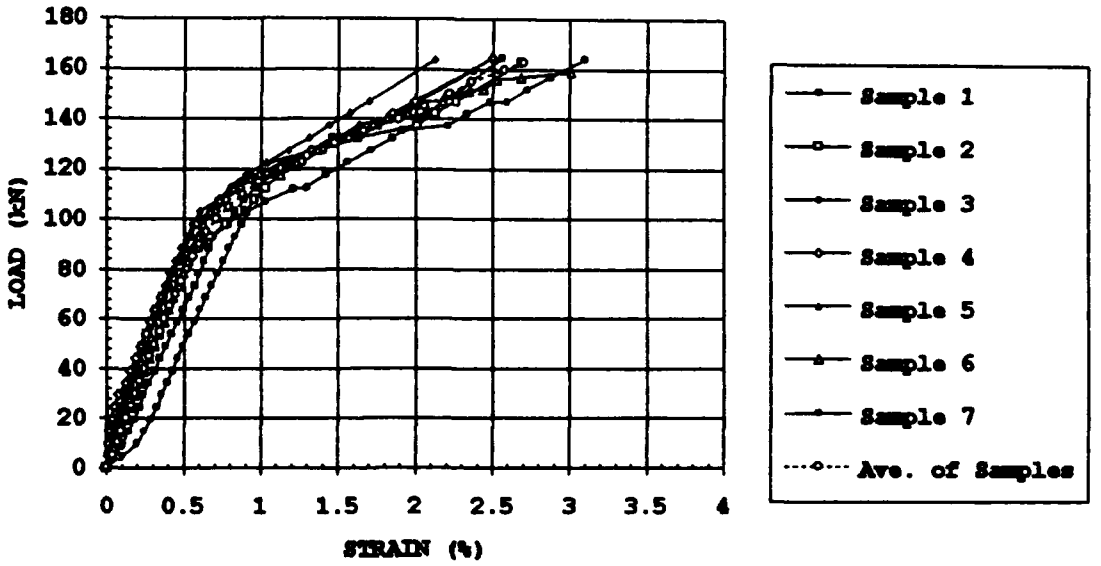


Figure A21. Load-Strain Data: K64/9.3 mm/PC Wire Core

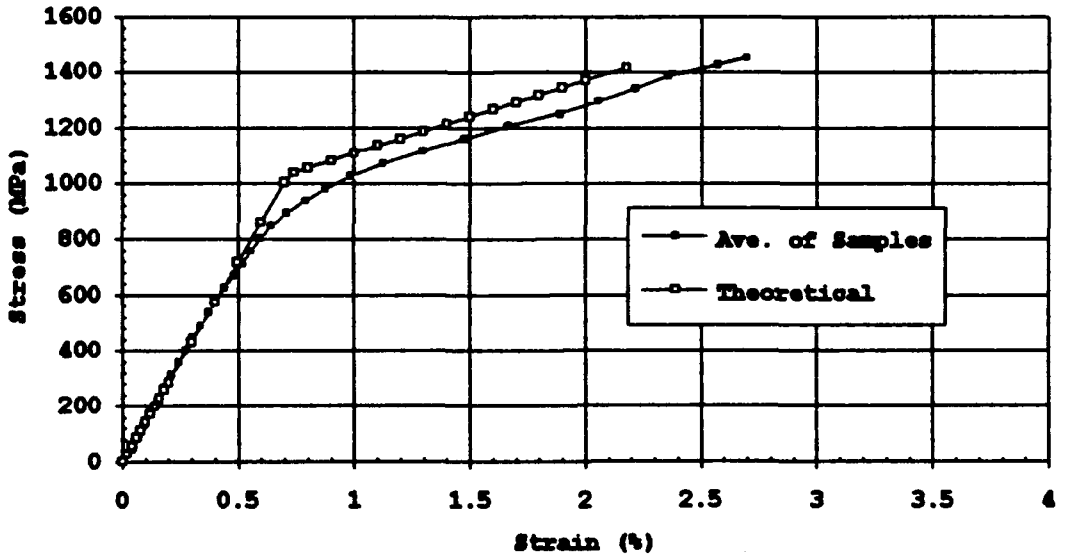


Figure A22. Stress-Strain Curve: K64/9.3 mm/PC Wire Core

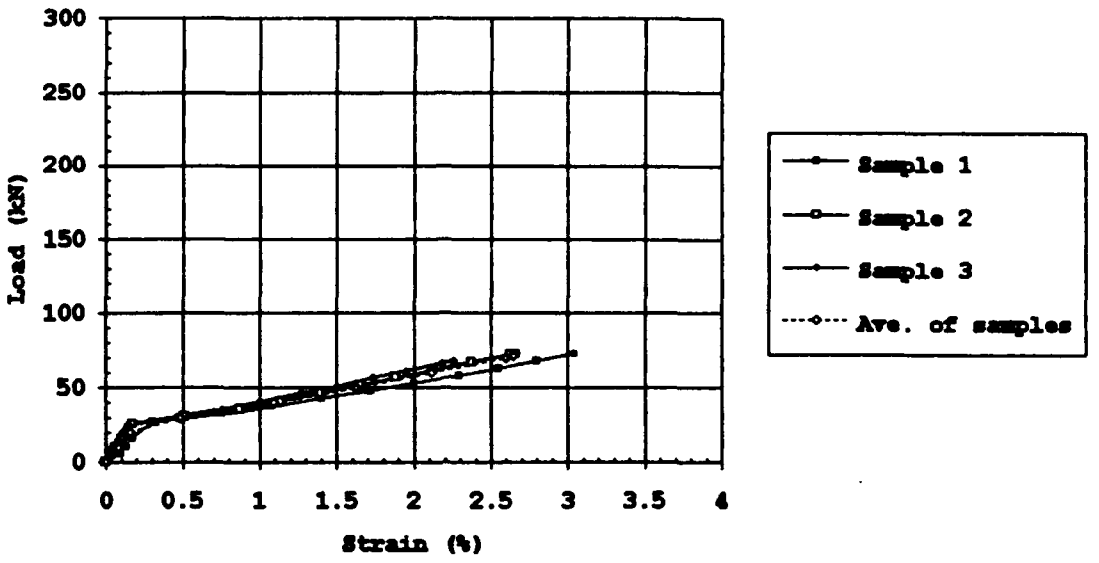


Figure A23. Load-Strain Data: K48/9.0 mm/SR24

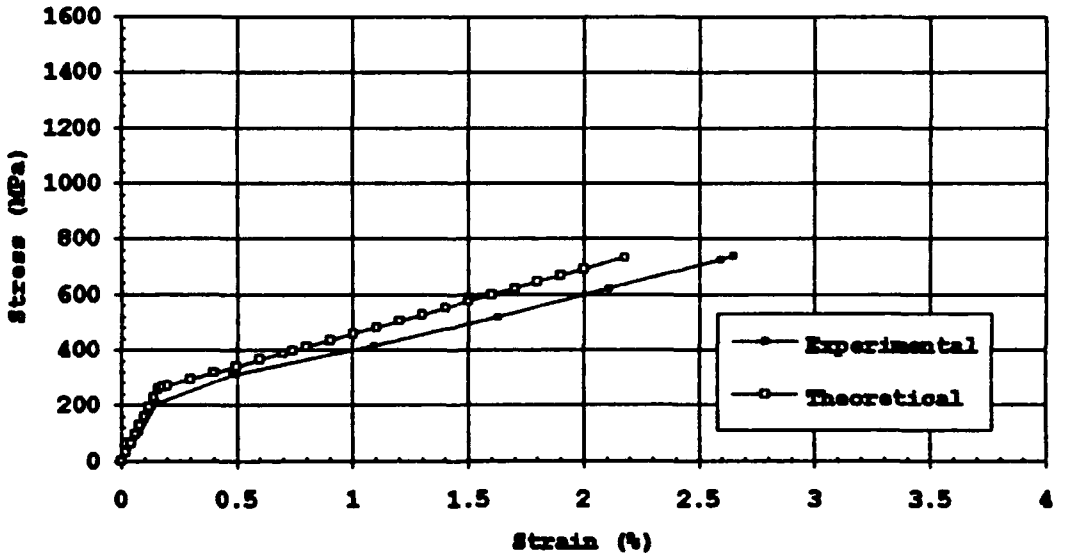


Figure A24. Stress-Strain Curve: K48/9.0 mm/SR24

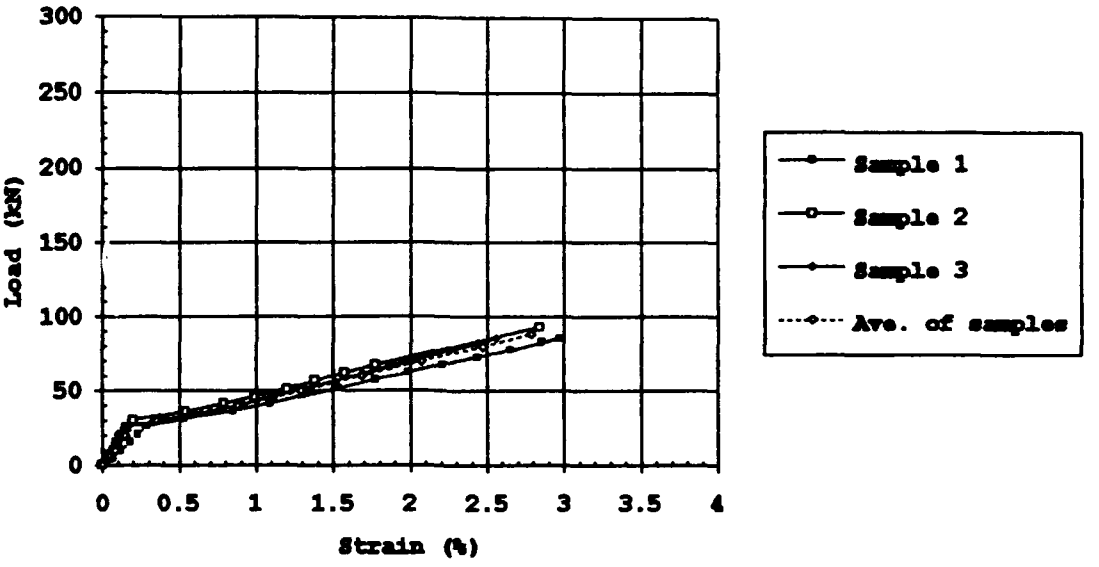


Figure A25. Load-Strain Data: K64/9.0 mm/SR24

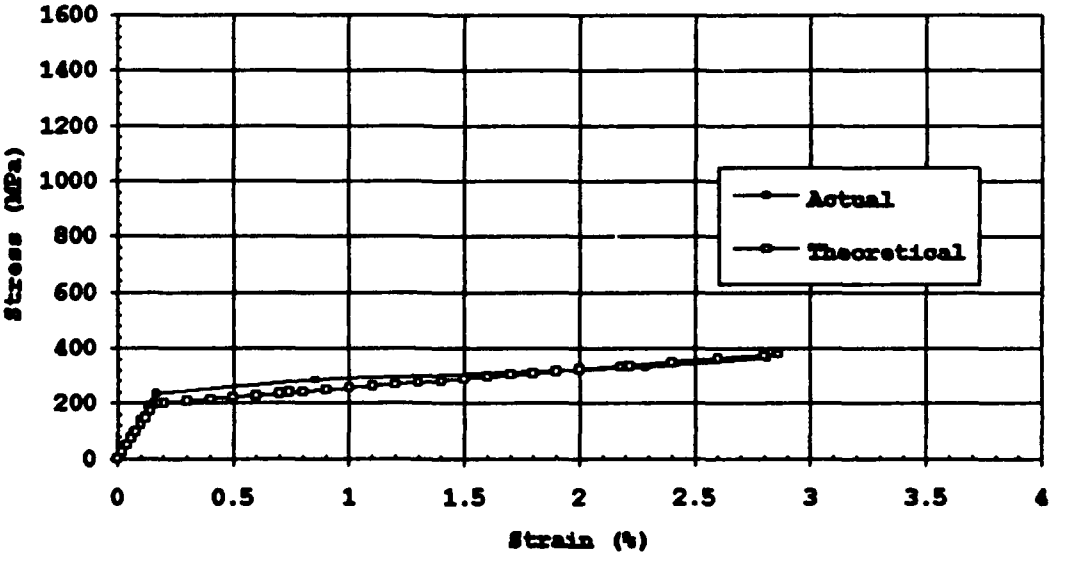


Figure A26. Stress-Strain Curve: K64/9.0 mm/SR24

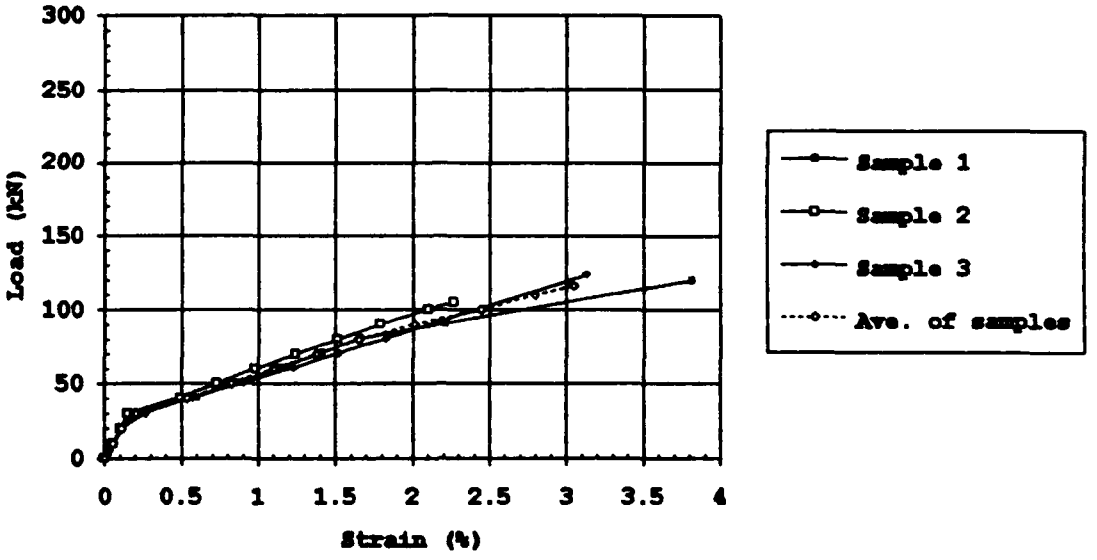


Figure A27. Load-Strain Data: K96/9.0 mm/SR24

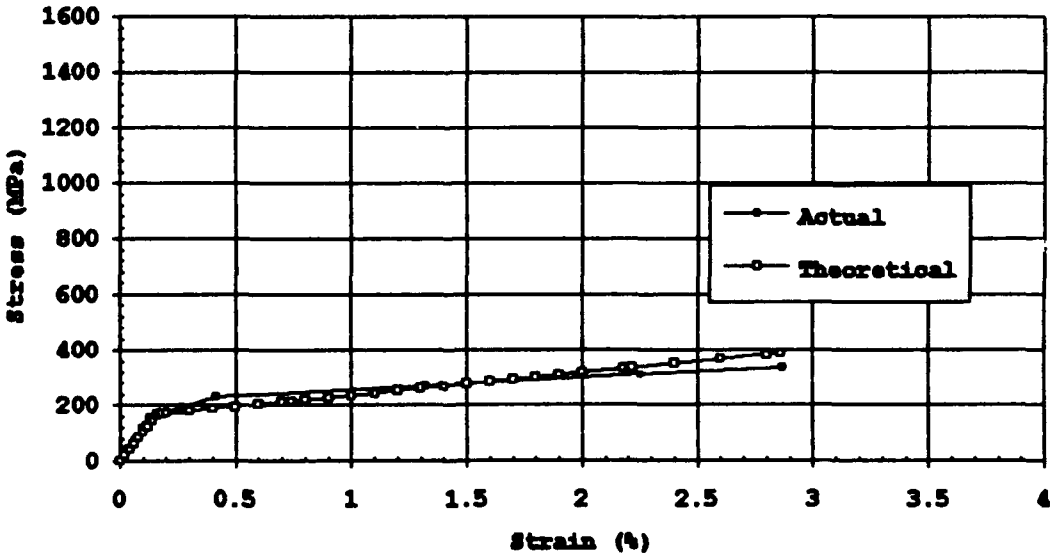


Figure A28. Stress-Strain Curve: K96/9.0 mm/SR24

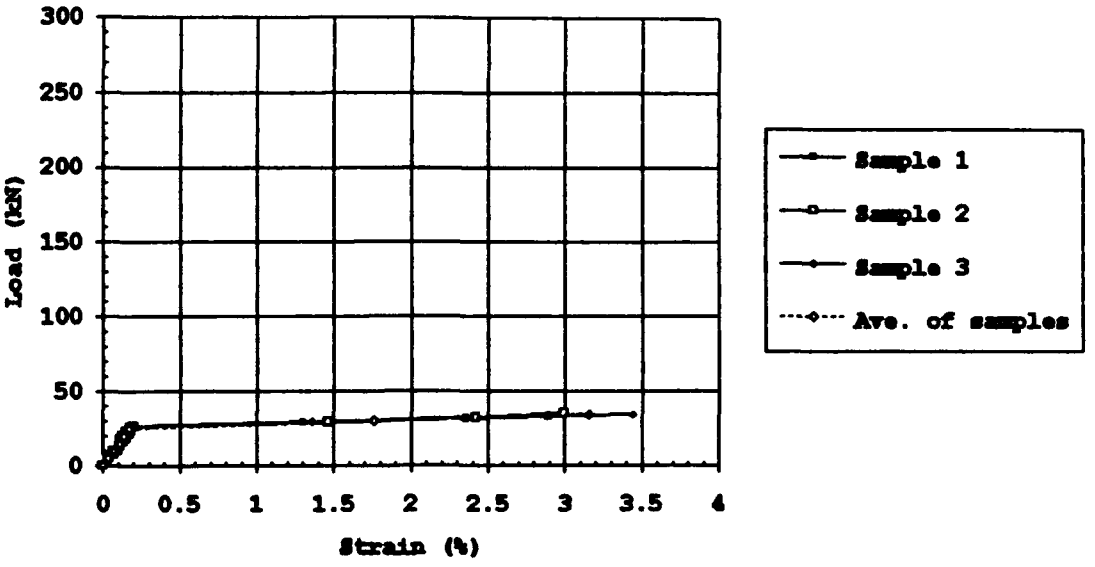


Figure A29. Load-Strain Data: V48/9.0 mm/SR24

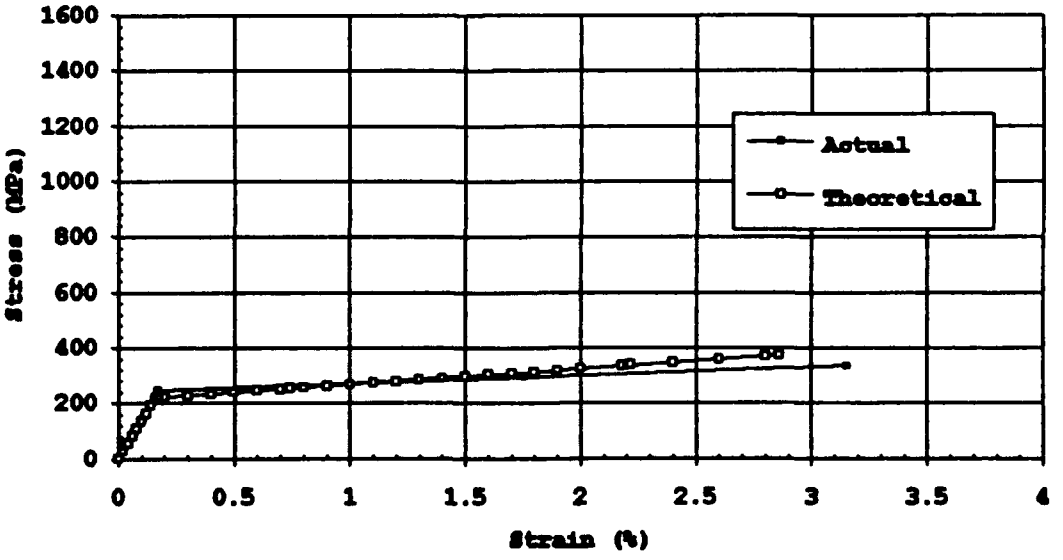


Figure A30. Stress-Strain Curve: V48/9.0 mm/SR24

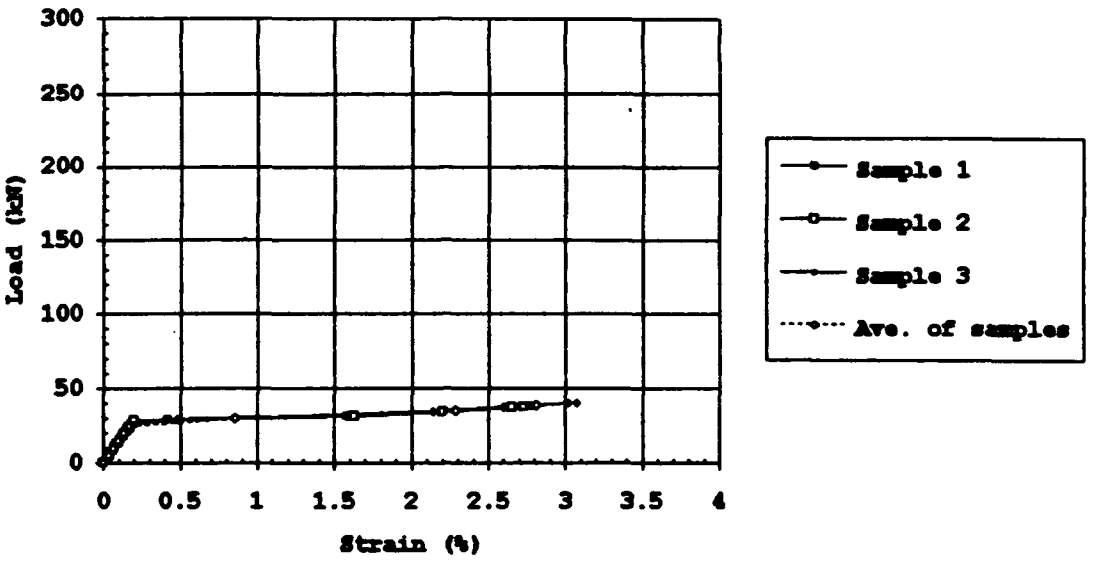


Figure A31. Load-Strain Data: V64/9.0 mm/SR24

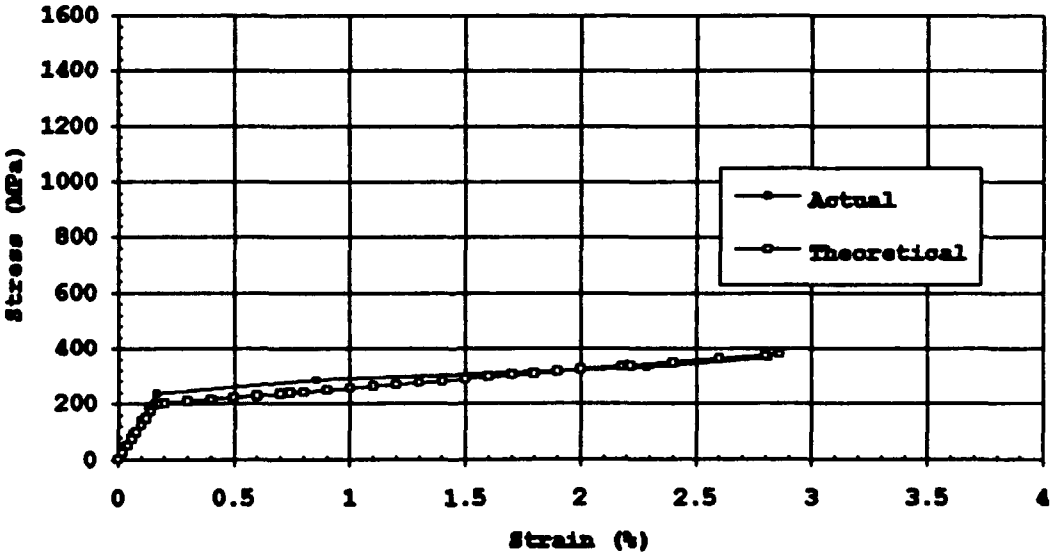


Figure A32. Stress-Strain Curve: V64/9.0 mm/SR24

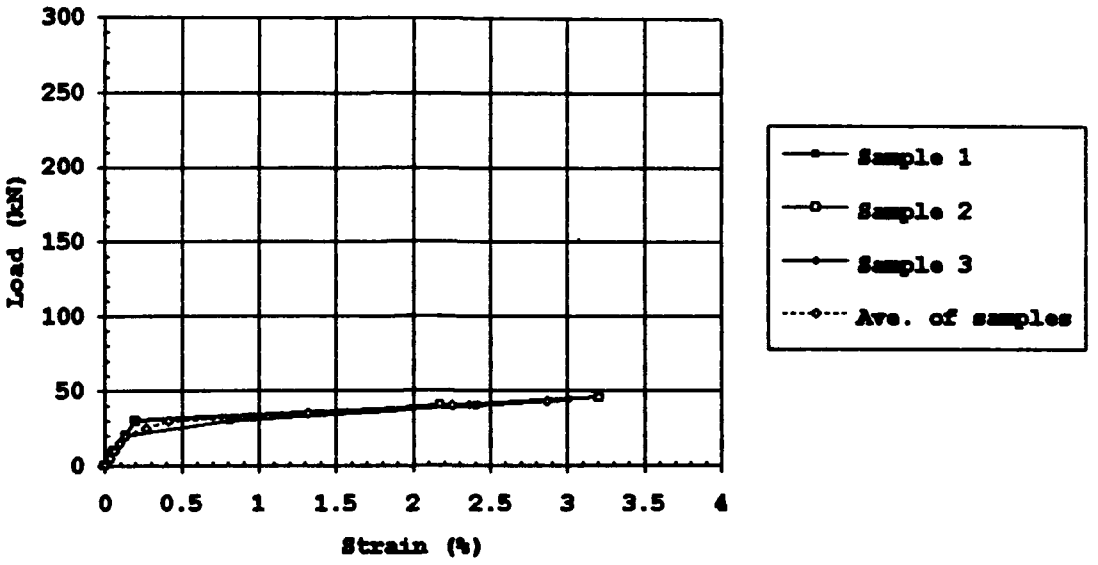


Figure A33. Load-Strain Data: V96/9.0 mm/SR24

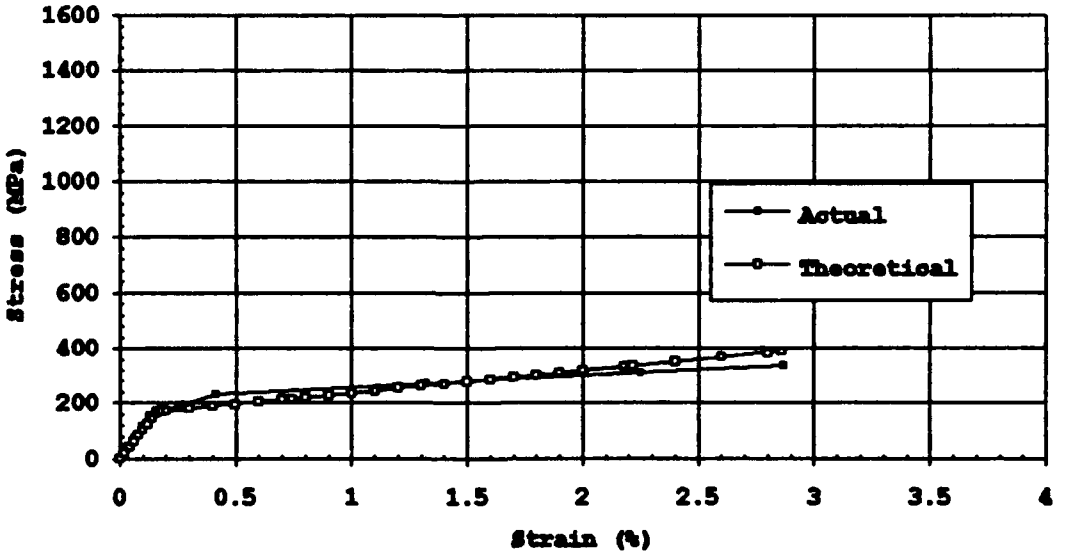


Figure A34. Stress-Strain Curve: V96/9.0 mm/SR24

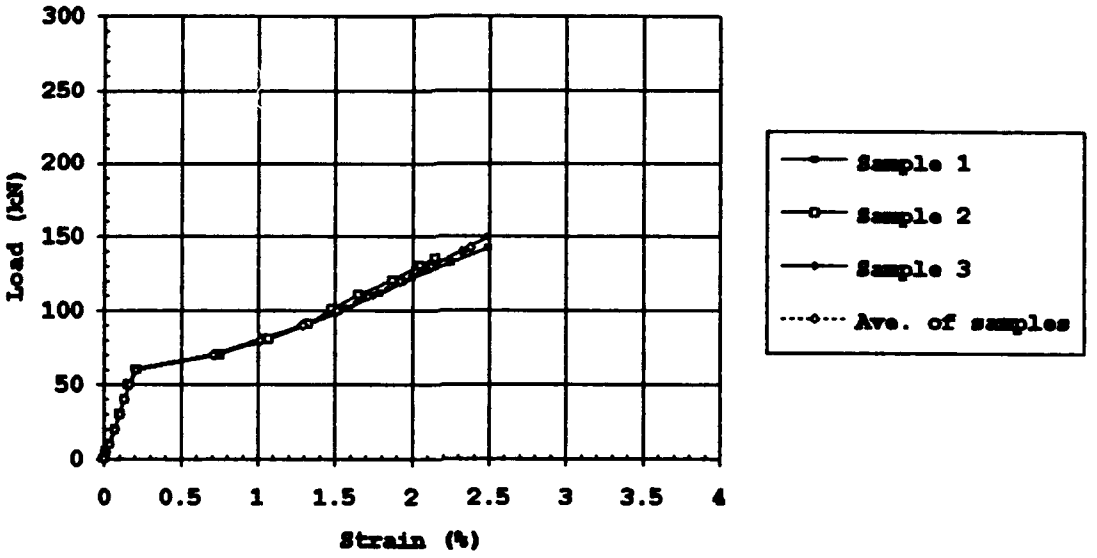


Figure A35. Load-Strain Data: K96/13.0 mm/SR24

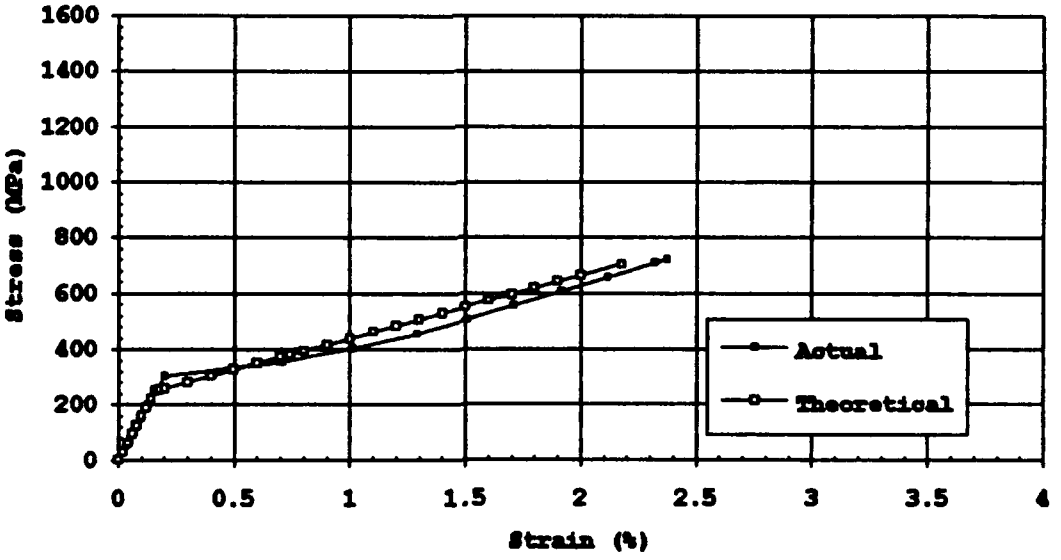


Figure A36. Stress-Strain Curve: K96/13.0 mm/SR24

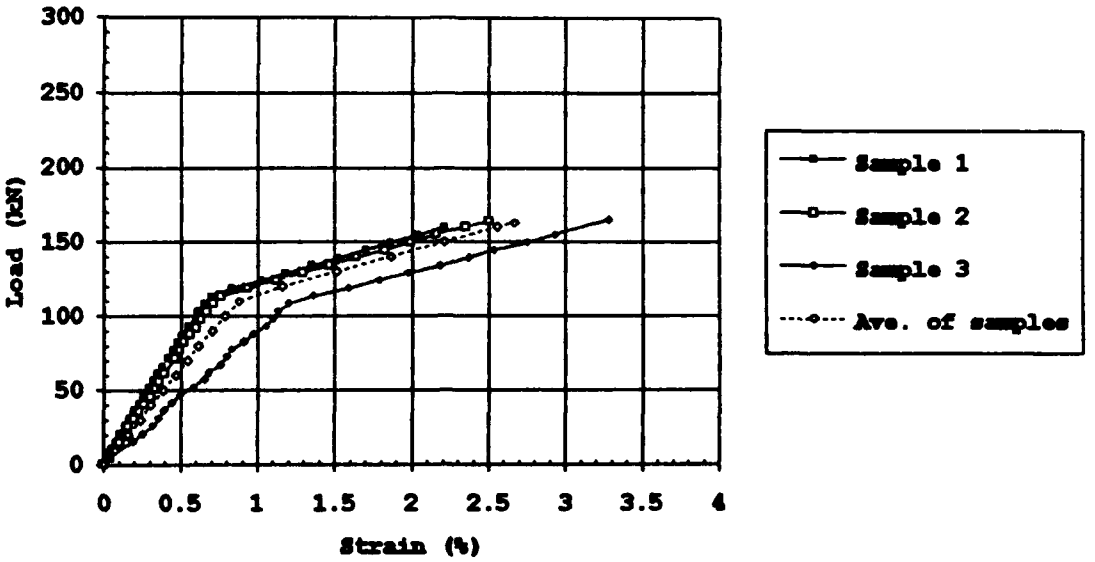


Figure A37. Load-Strain Data: K64/9.2 mm/SBPR80

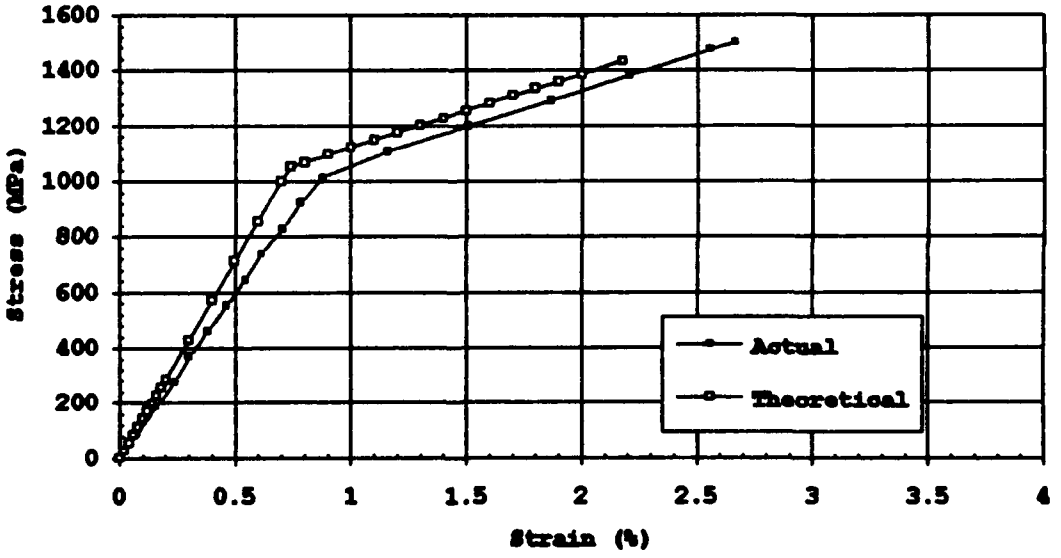


Figure A38. Stress-Strain Curve: K64/9.2 mm/SBPR80

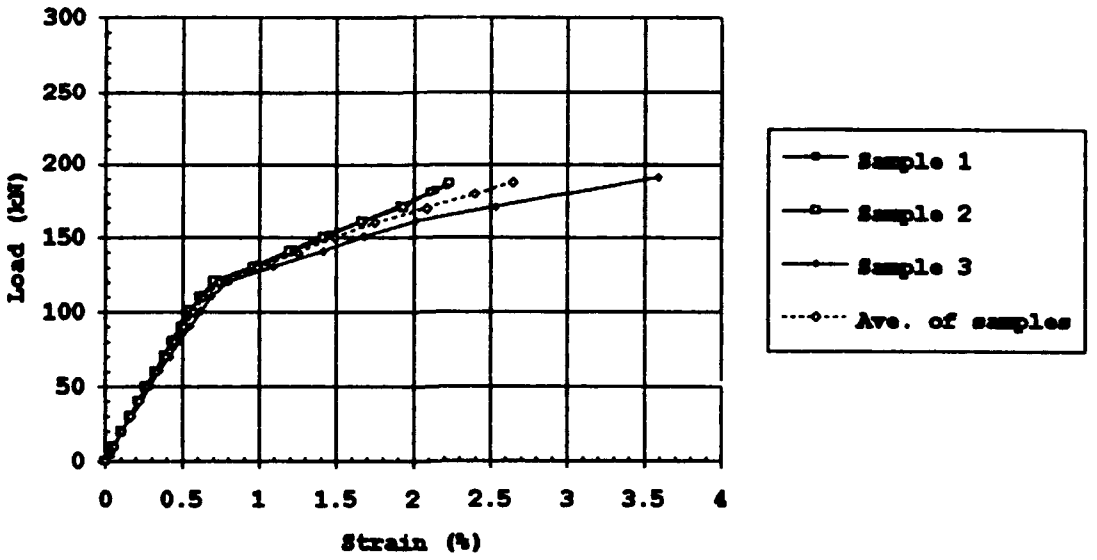


Figure A39. Load-Strain Data: K96/9.2 mm/SBPR80

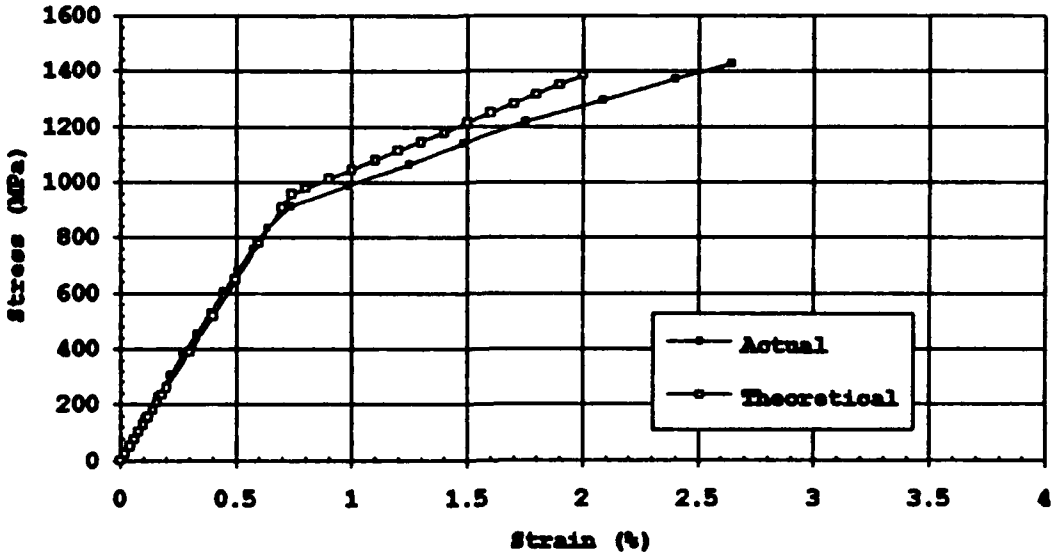


Figure A40. Stress-Strain Curve: K96/9.2 mm/SBPR80

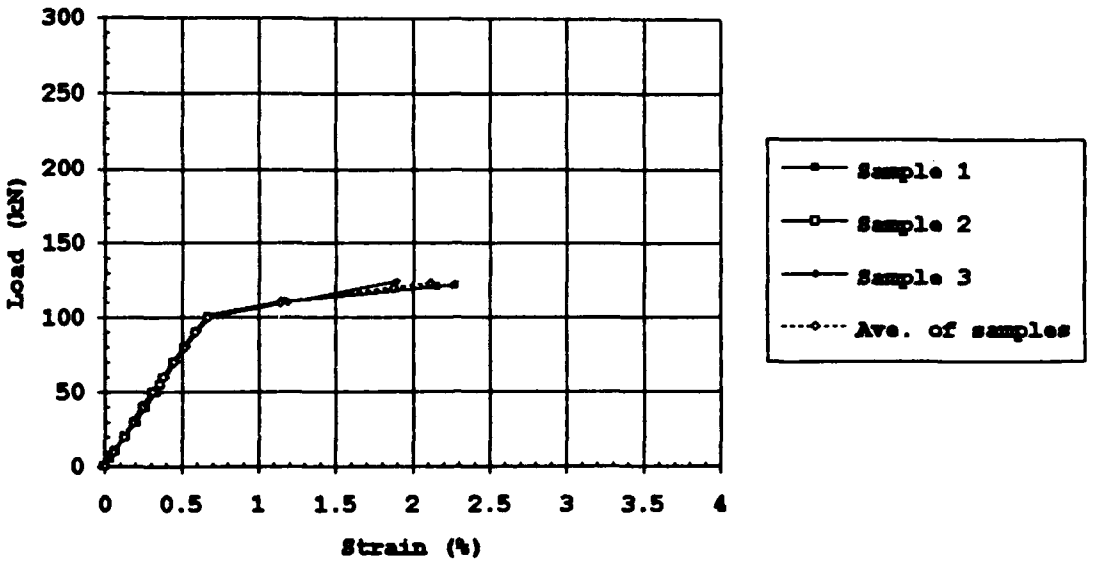


Figure A41. Load-Strain Data: V96/9.2 mm/SBPR80

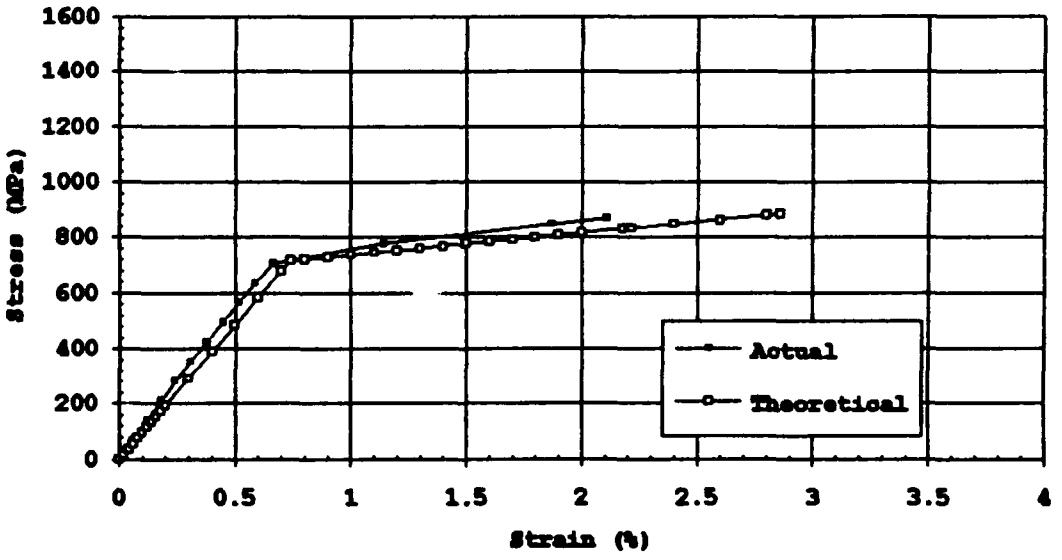


Figure A42. Stress-Strain Curve: V96/9.2 mm/SBPR80

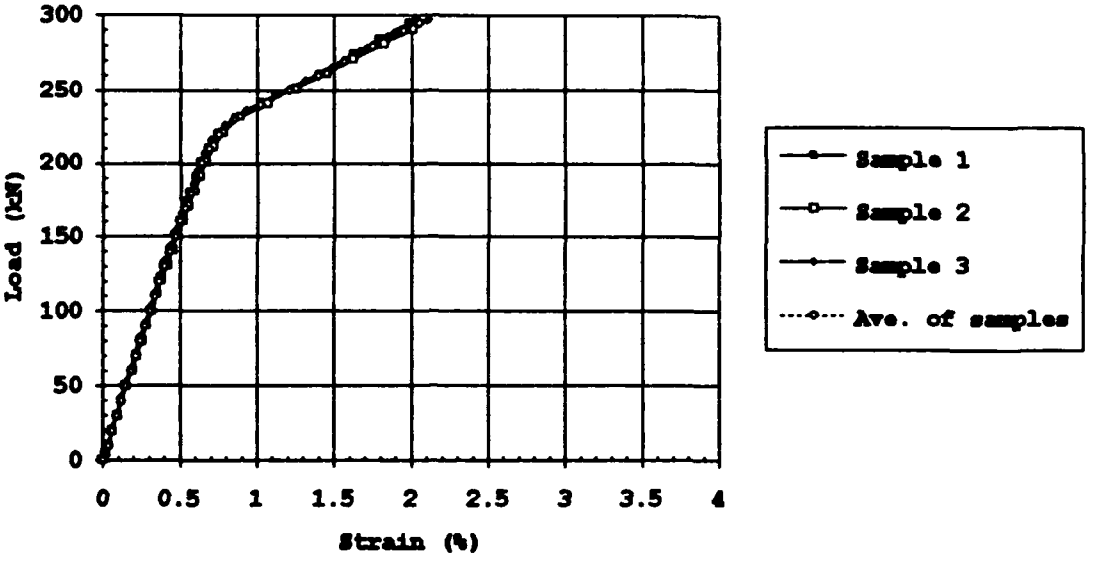


Figure A43. Load-Strain Data: K96/13.0 mm/SBPR80

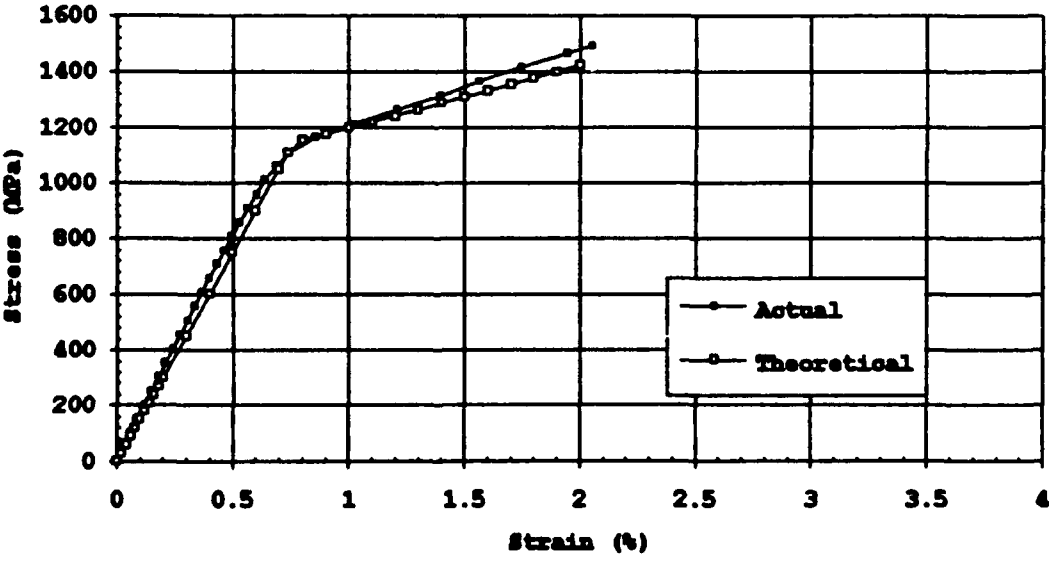


Figure A44. Stress-Strain Curve: K96/13.0 mm/SBPR80

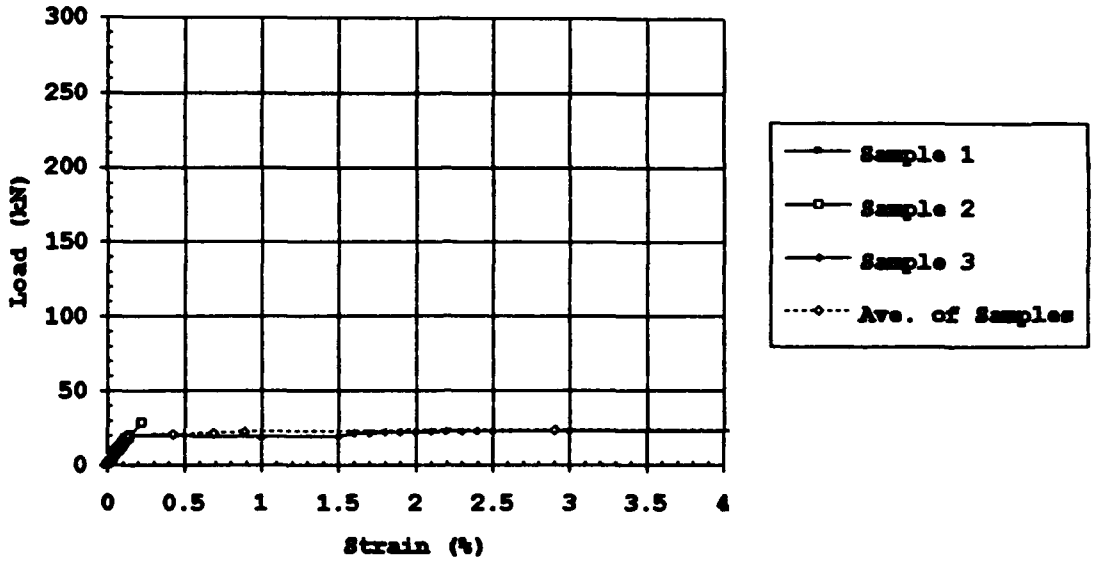


Figure A45. Load-Strain Data: 9.0 mm/SR24 Steel Core

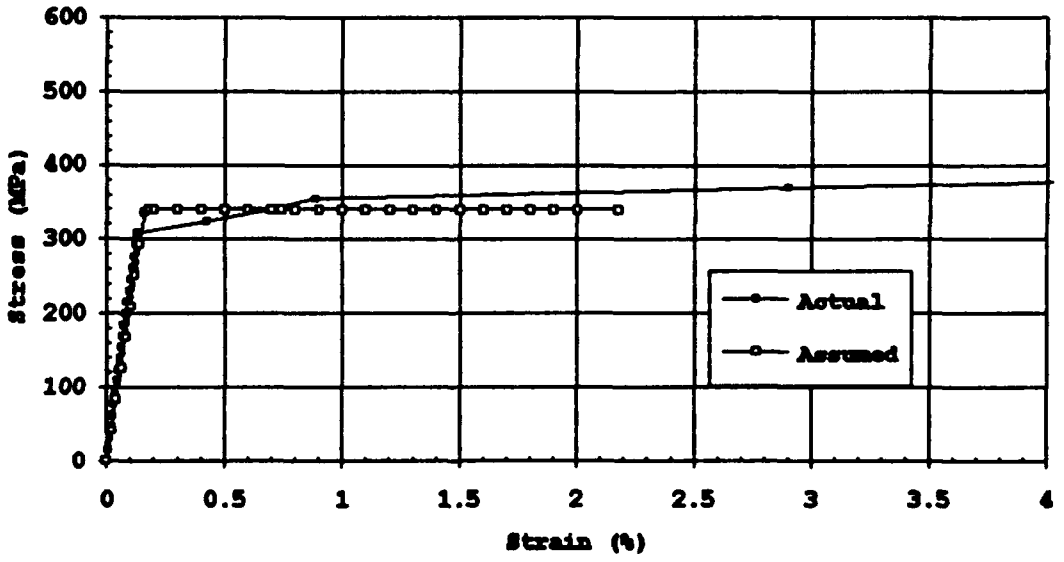


Figure A46. Stress-Strain Curve: 9.0 mm/SR24 Steel Core

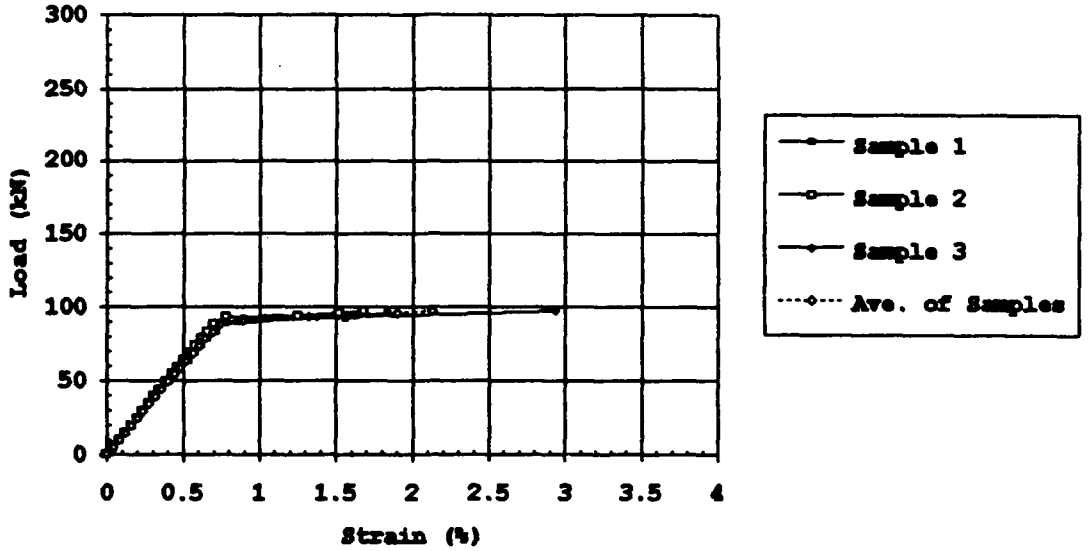


Figure A47. Load-Strain Data: 9.2 mm/SBPR80 Steel Core

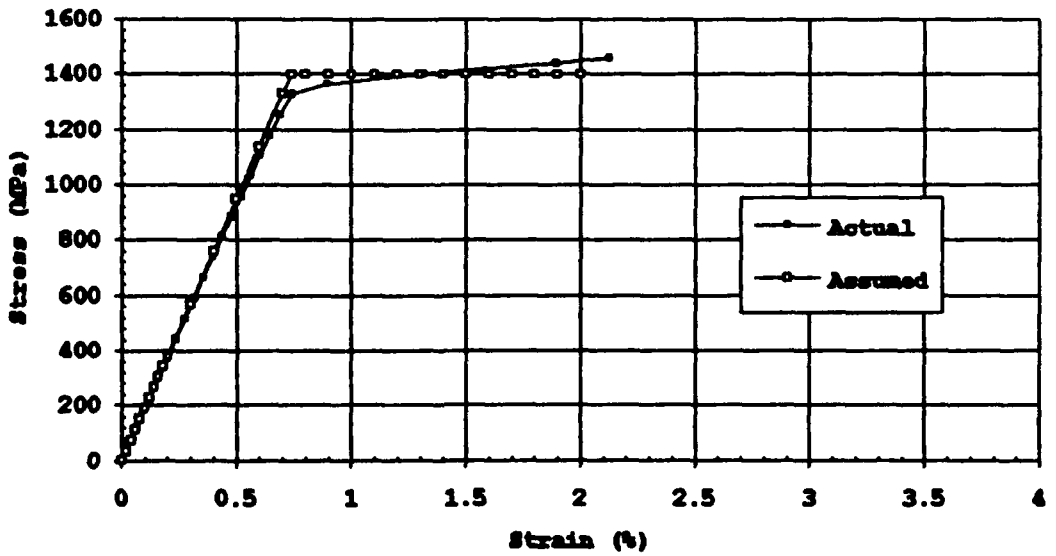


Figure A48. Stress-Strain Curve: 9.2 mm/SBPR80 Steel Core

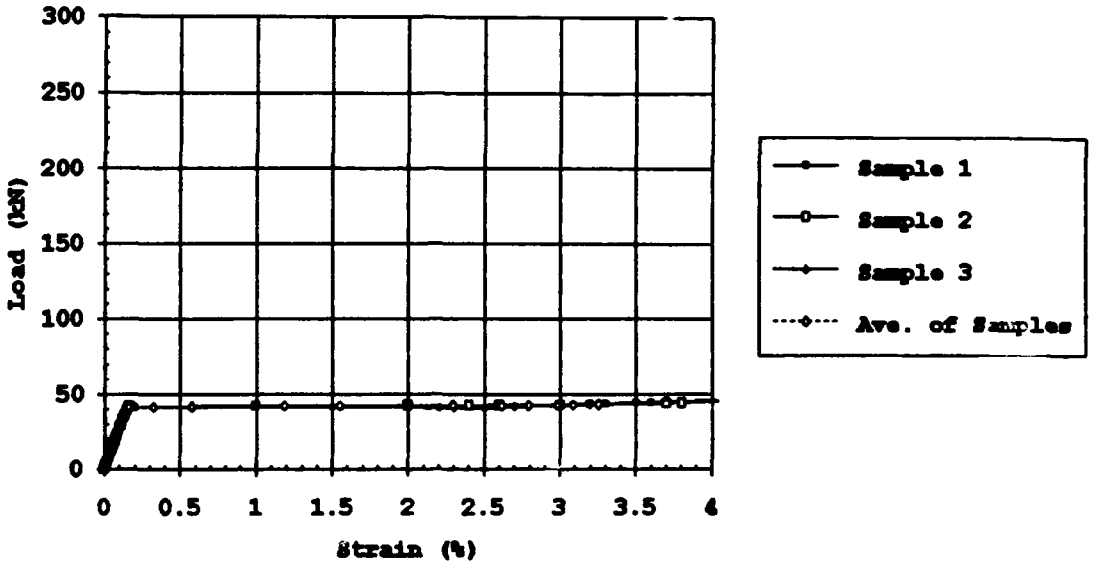


Figure A49. Load-Strain Data: 13.0 mm/SR24 Steel Core

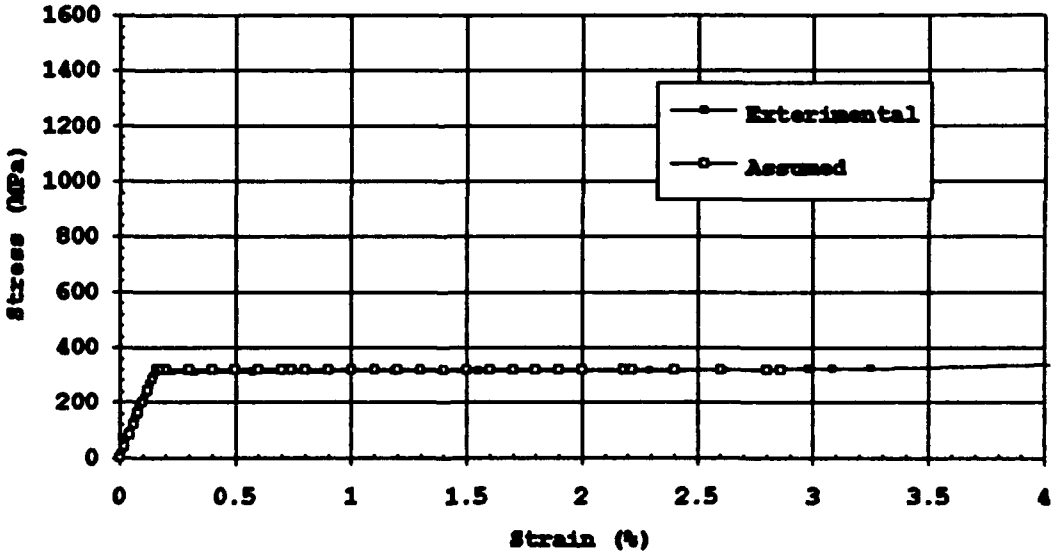


Figure A50. Stress-Strain Curve: 13.0 mm/SR24 Steel Core

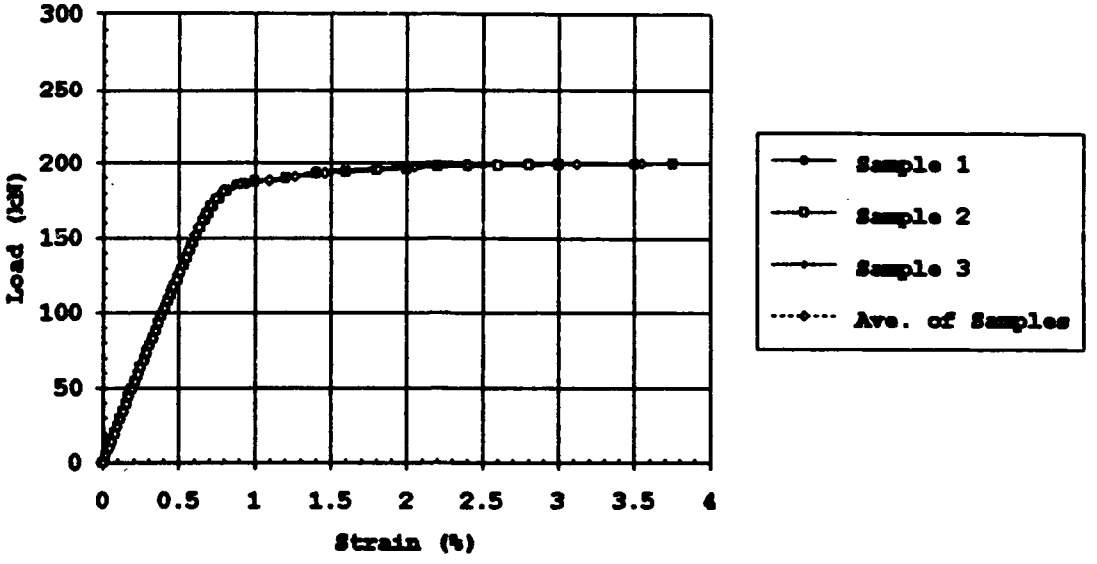


Figure A51. Load-Strain Data: 13.0 mm/SBPR80 Steel Core

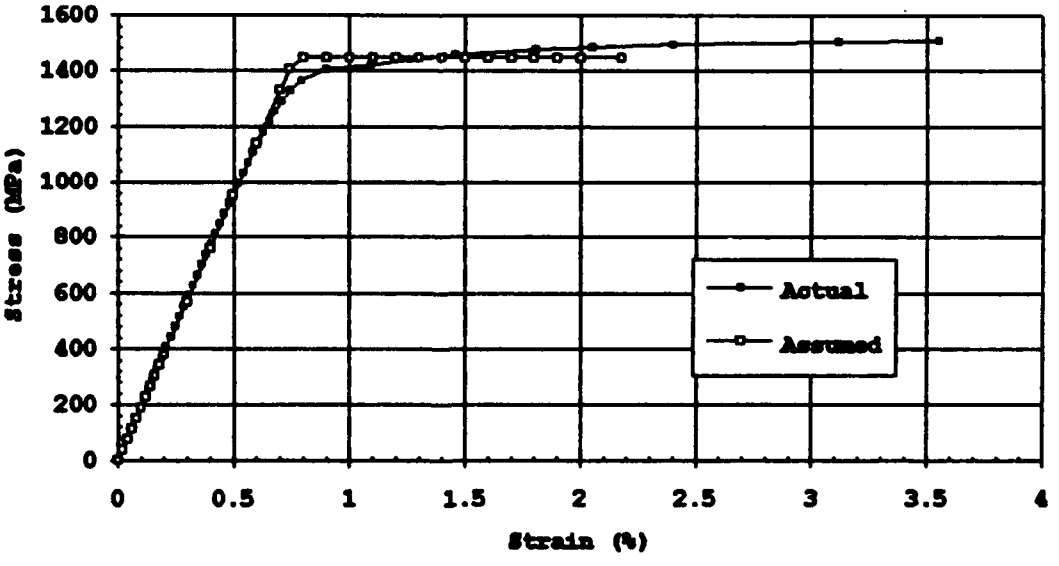


Figure A52. Stress-Strain Curve: 13.0 mm/SBPR80 Steel Core

# APPENDIX B

## BEAM TEST DATA

B-1. Photos of Test Beam Fabrication

B-2. Photos of Beam Testing

B-3. Load-Deflection Curves

B-4. Experimental and Theoretical Load Curves

B-5. Example of XY Plotter Output

B-6. Crack Pattern Tracings

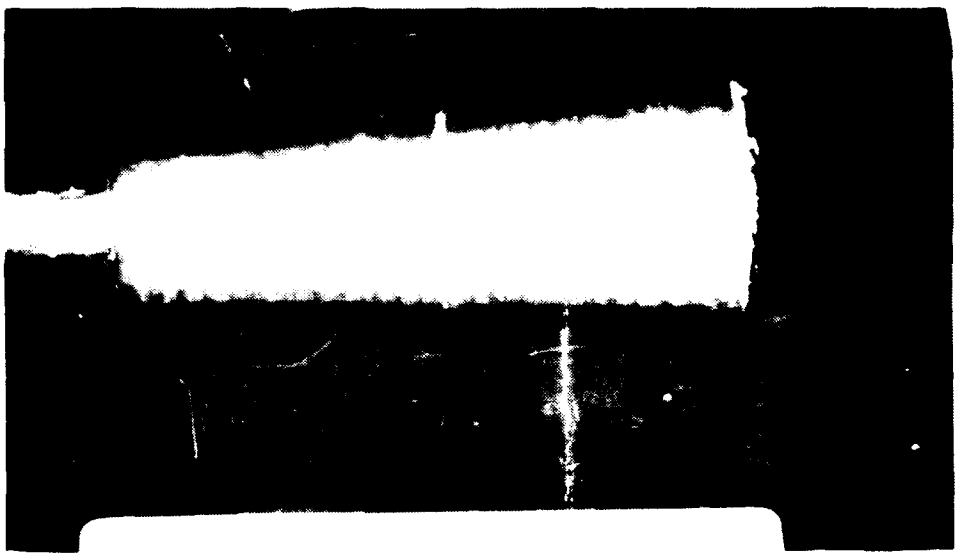

Figure B1. Hybrid Rod Anchor

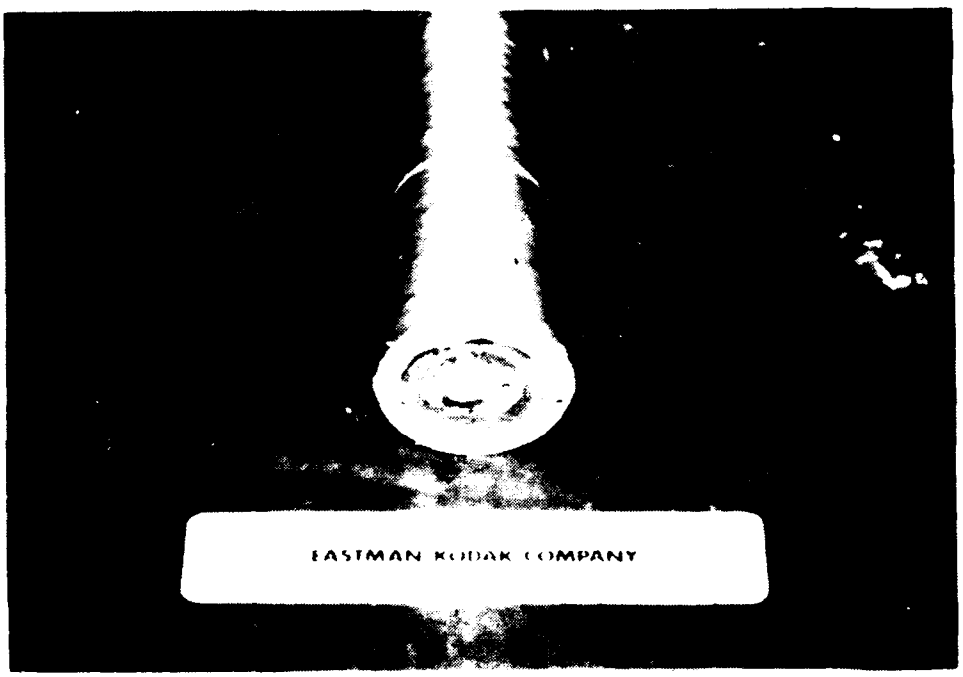


Figure B2. Hybrid Rod Anchor

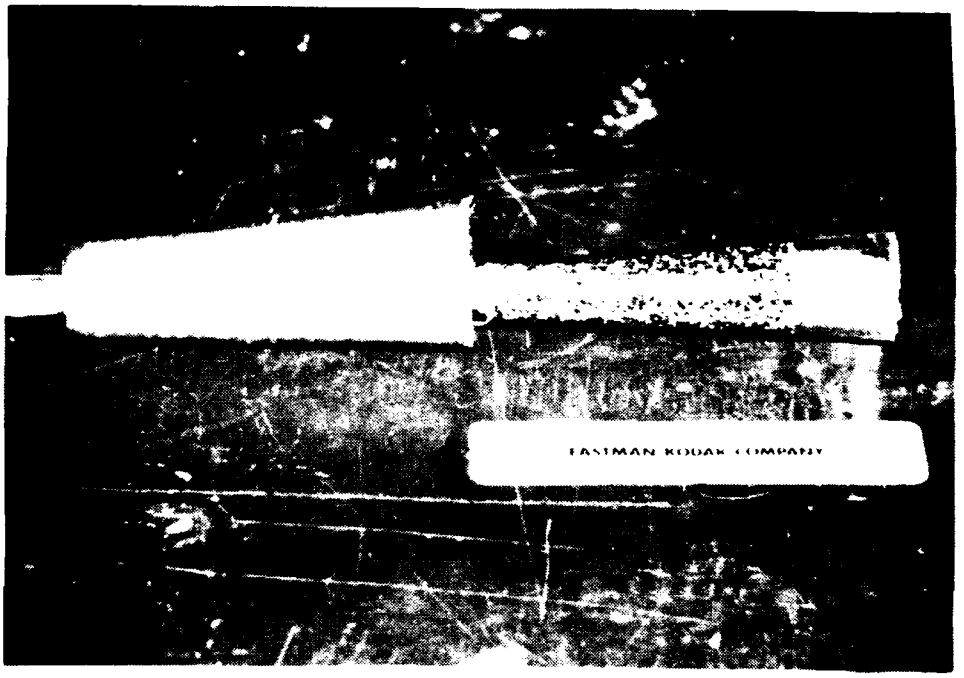

Figure B3. Hybrid Rod Anchor

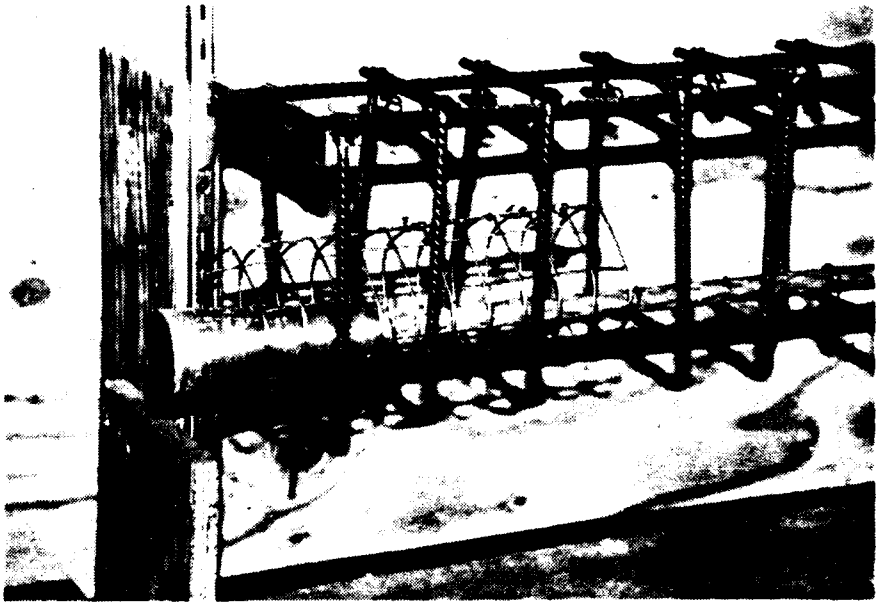

Figure B4. Rebar Cage with Hybrid Rod

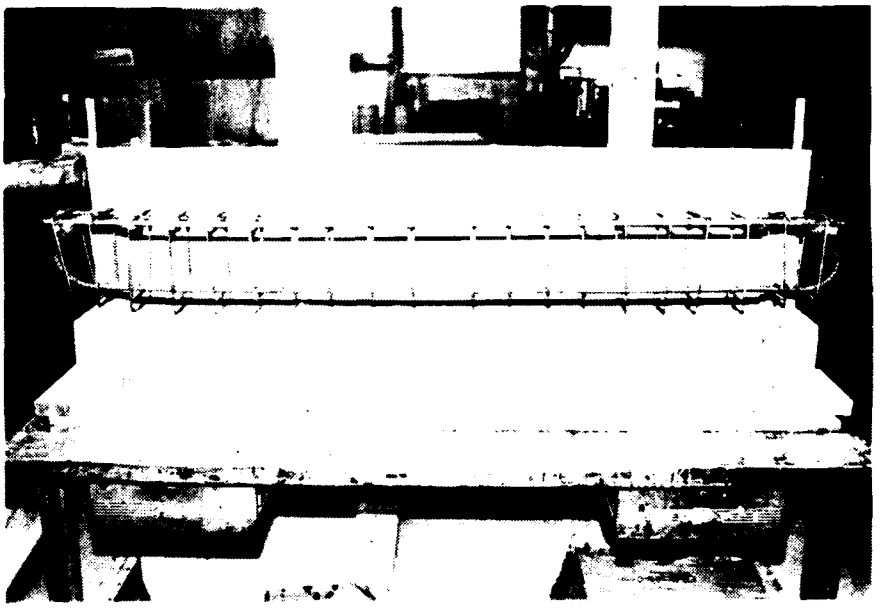

Figure B5. Rebar Cage with Conventional Rebar

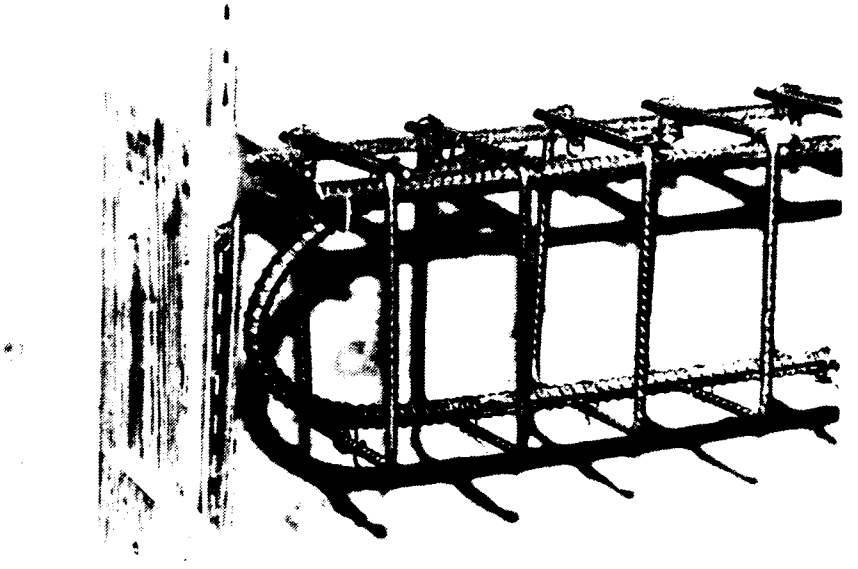

Figure B6. Closeup of Conventional Rebar Anchorage

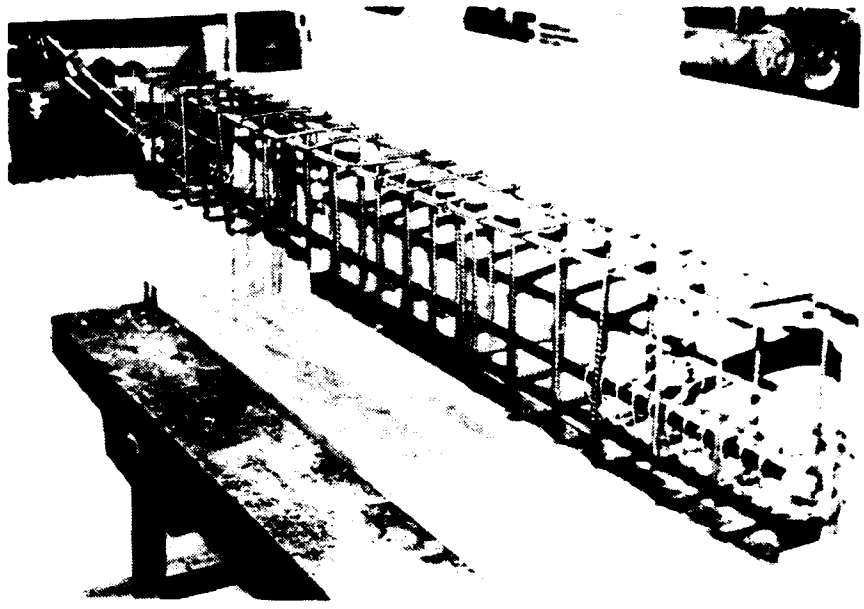

Figure B7. Rebar Cage with Smooth 13.0 mm Rod

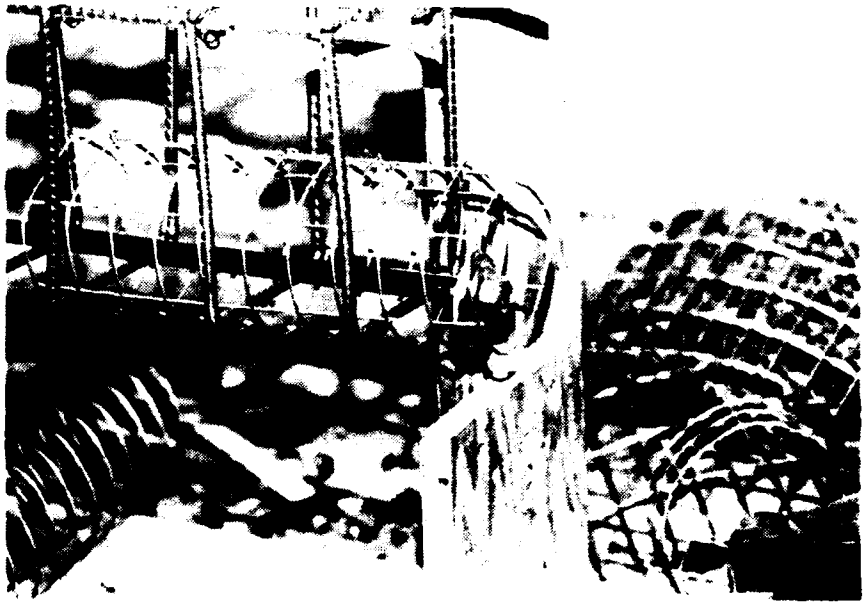

Figure B8. Closeup of Smooth Rod Anchorage

Figure B9. Forms for Test Beams

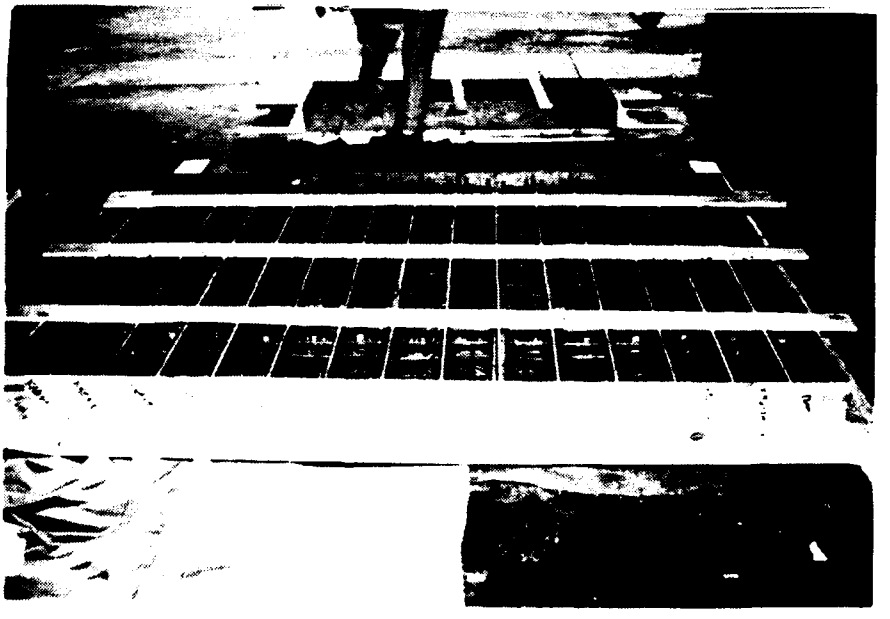

Figure B10. Large Form and Rebar Cages

Figure B11. Small Form and Rebar Cages

Figure B12. Placement and Vibration of Concrete

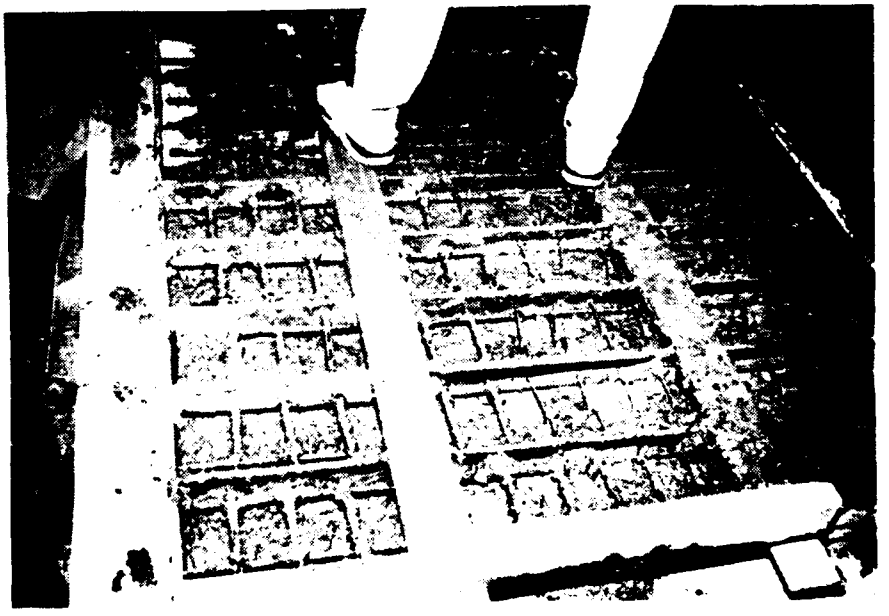

Figure B13. Placement of Concrete

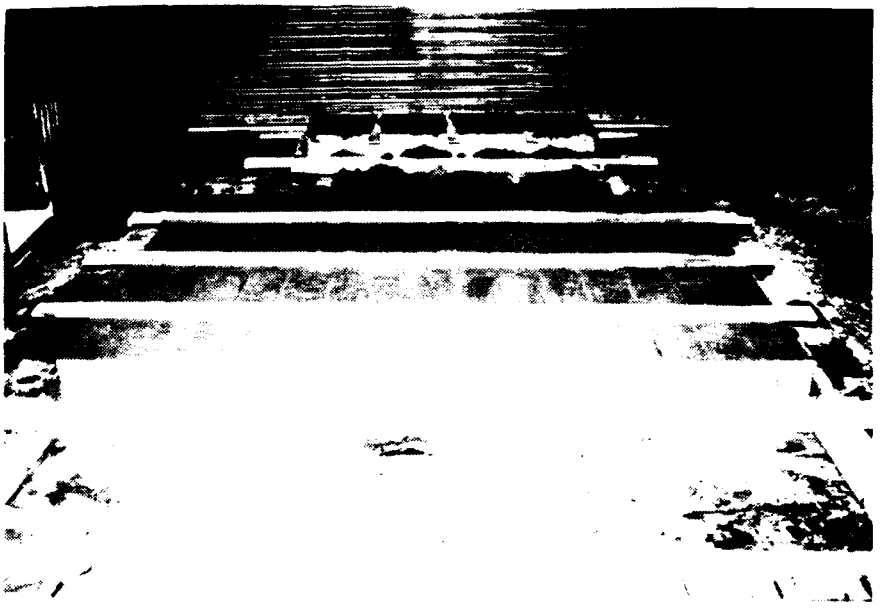

Figure B14. Curing of Test Beams

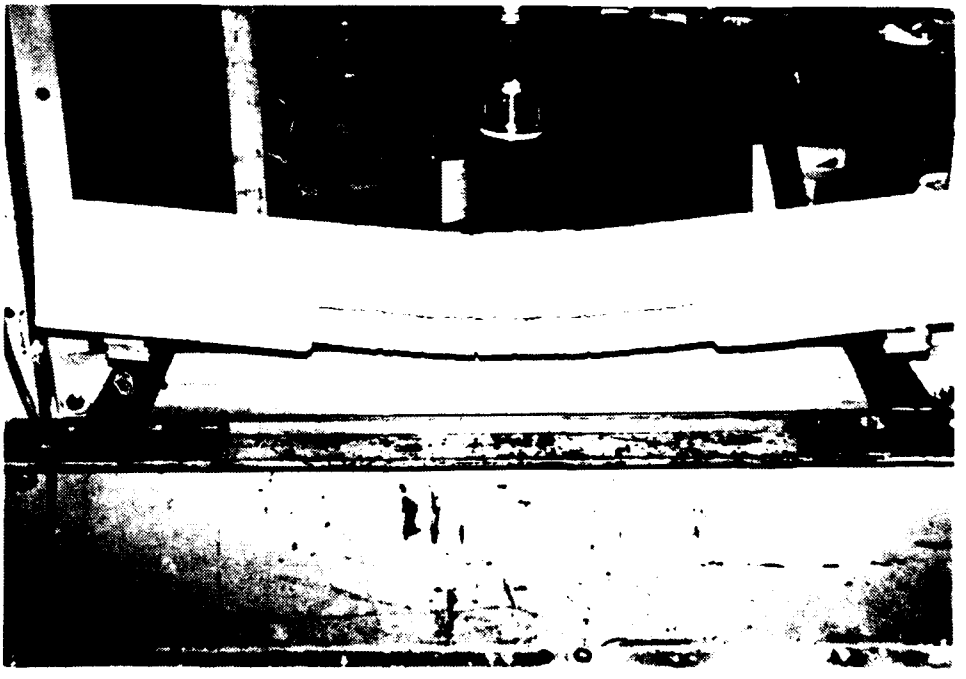

Figure B15. Test Beam #1 - #5 Rebar

Figure B16. Test Beam #3 - K48/9.0 mm/SR24

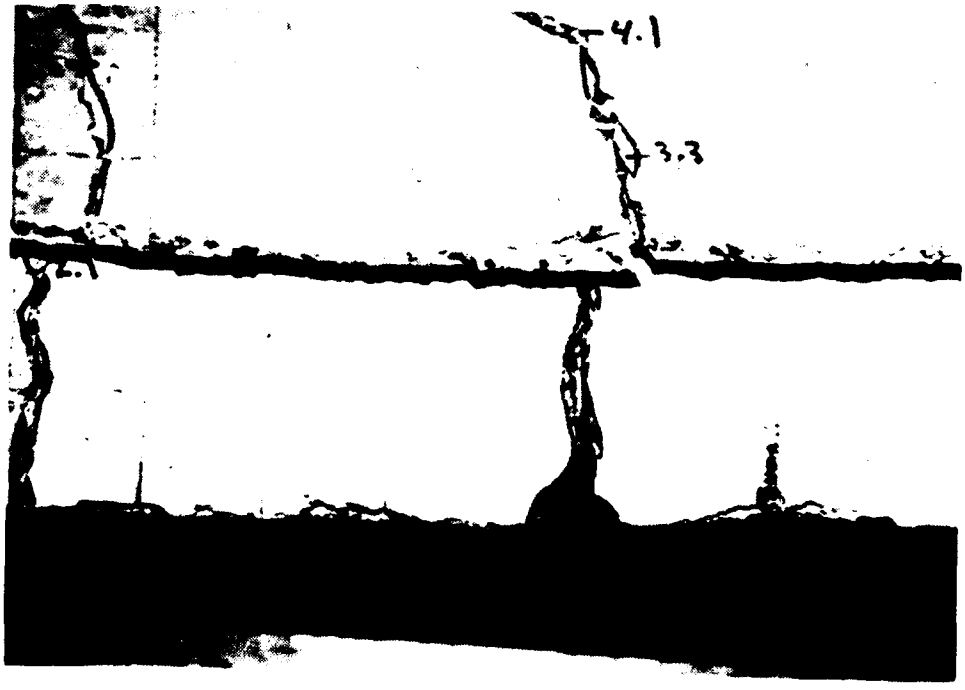


Figure B17. Test Beam #3 - Failure Crack

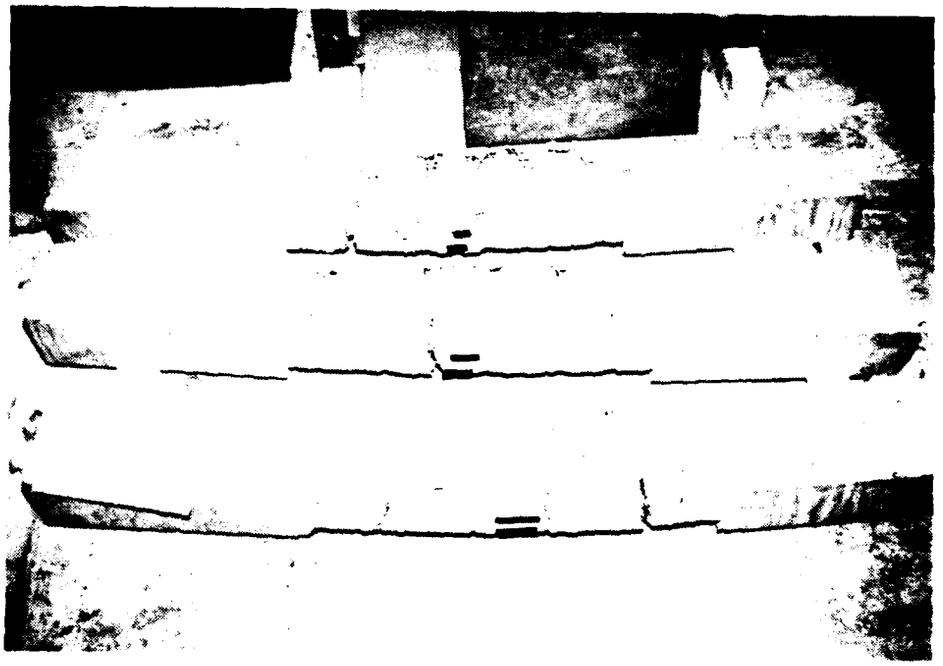

Figure B18. Test Beams #3, #4 and #5

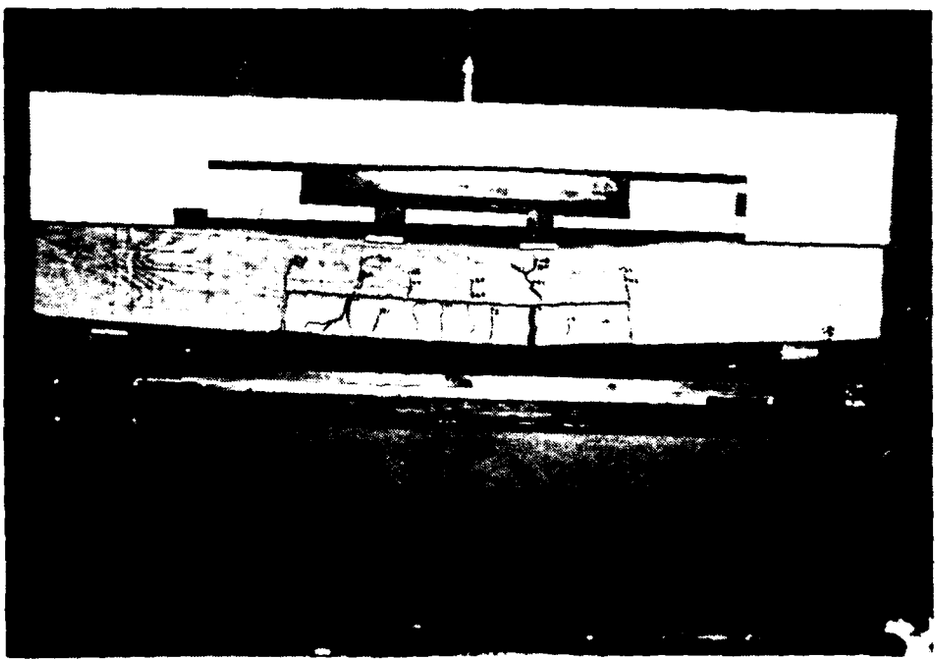

Figure B19. Test Beam #10 - Smooth 13.0 mm Rod

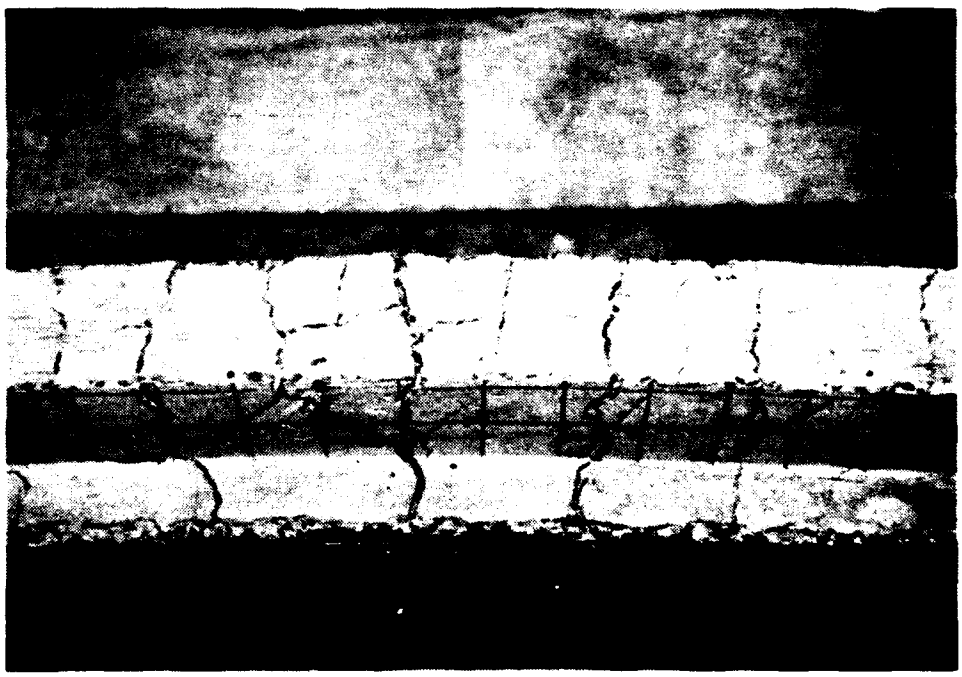

Figure B20. Test Beam #1 - #5 Rebar, Flexural Cracks

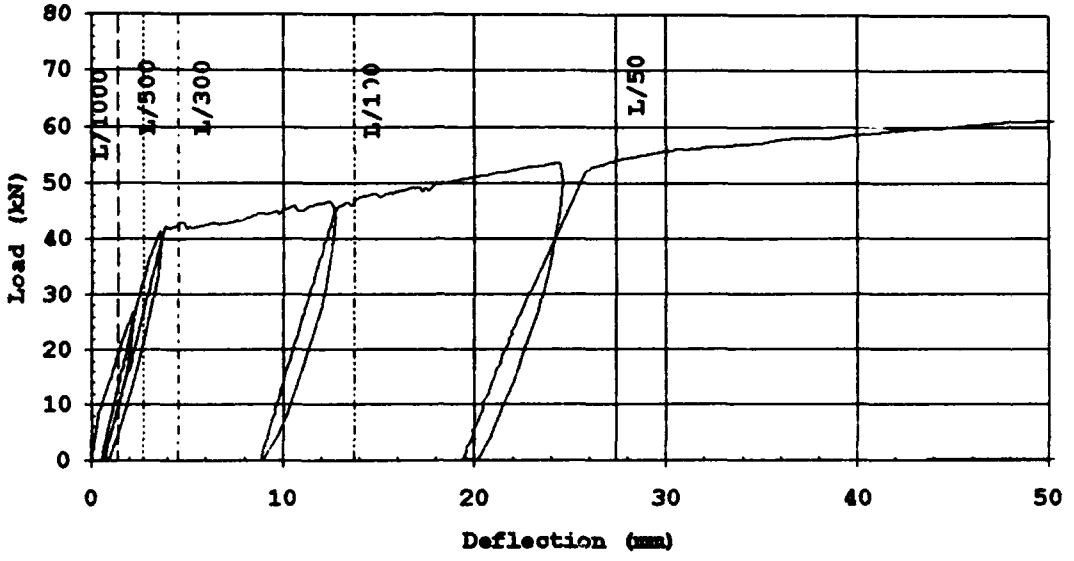


Figure B21. Load-Deflection Curve: Test Beam #1 - #5 Rebar

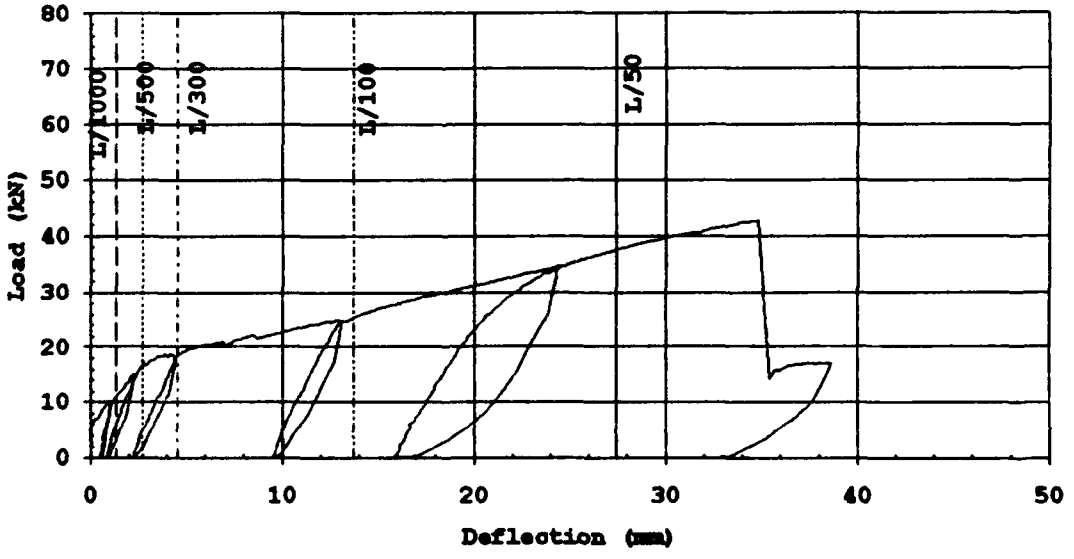


Figure B22. Load-Deflection Curve: Test Beam #3 - K48/9.0 mm/SR24

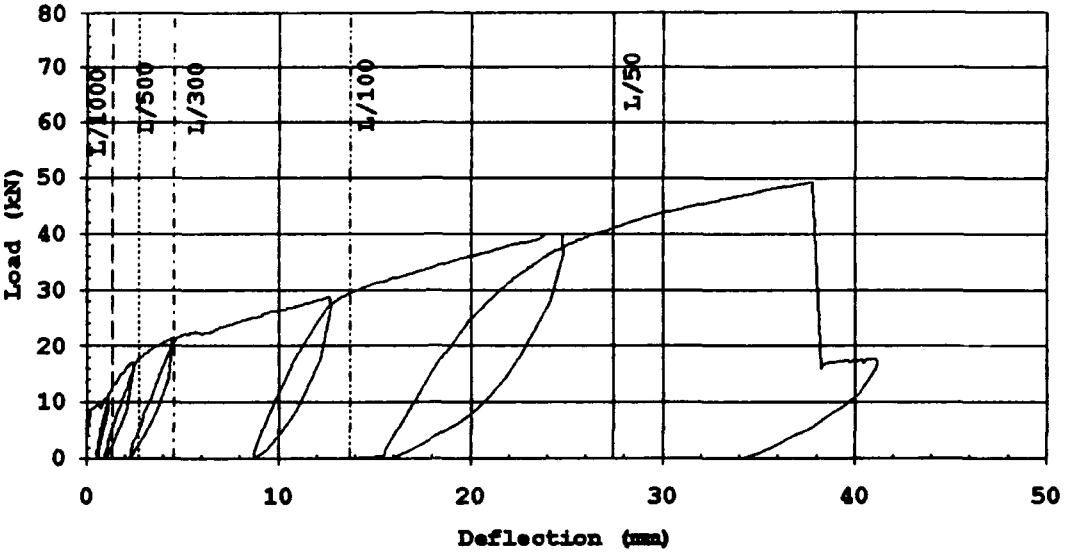


Figure B23. Load-Deflection Curve: Test Beam #4 - K64/9.0 mm/SR24

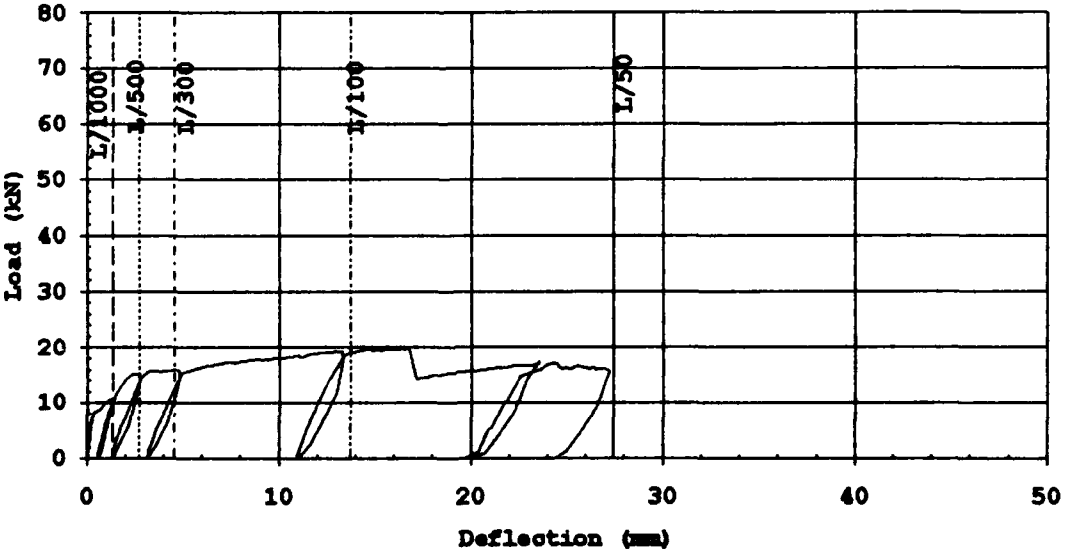


Figure B24. Load-Deflection Curve: Test Beam #5 - V48/9.0 mm/SR24

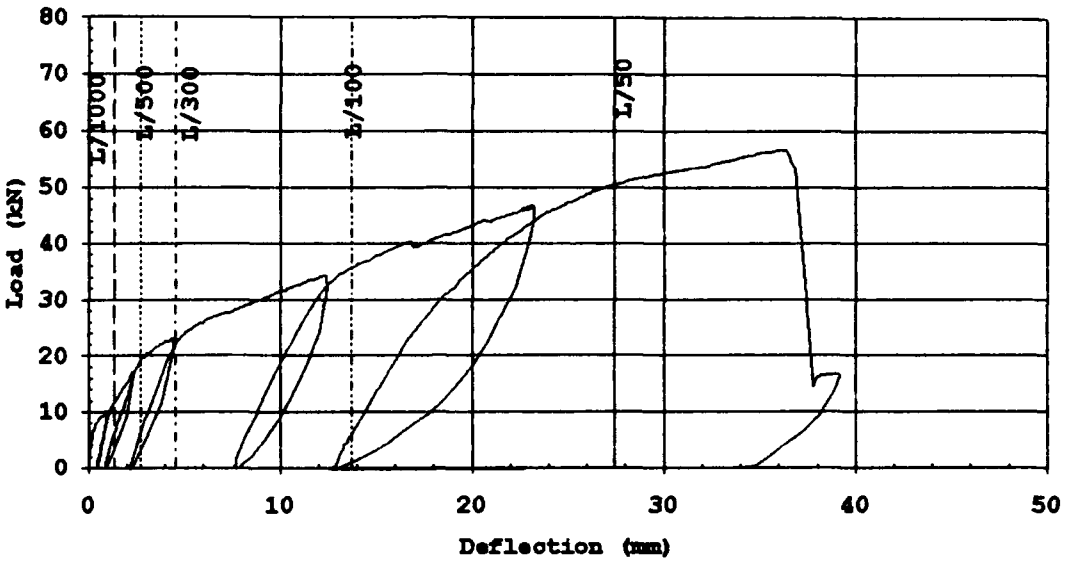


Figure B25. Load-Deflection Curve: Test Beam #6 - K96/9.0 mm/SR24

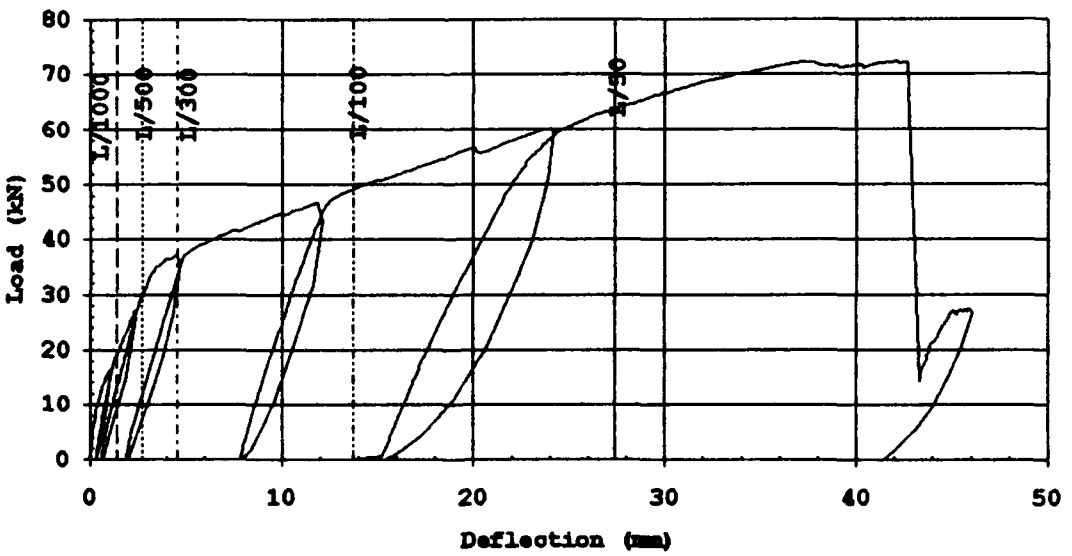


Figure B26. Load-Deflection Curve: Test Beam #7 - K96/13.0 mm/SR24

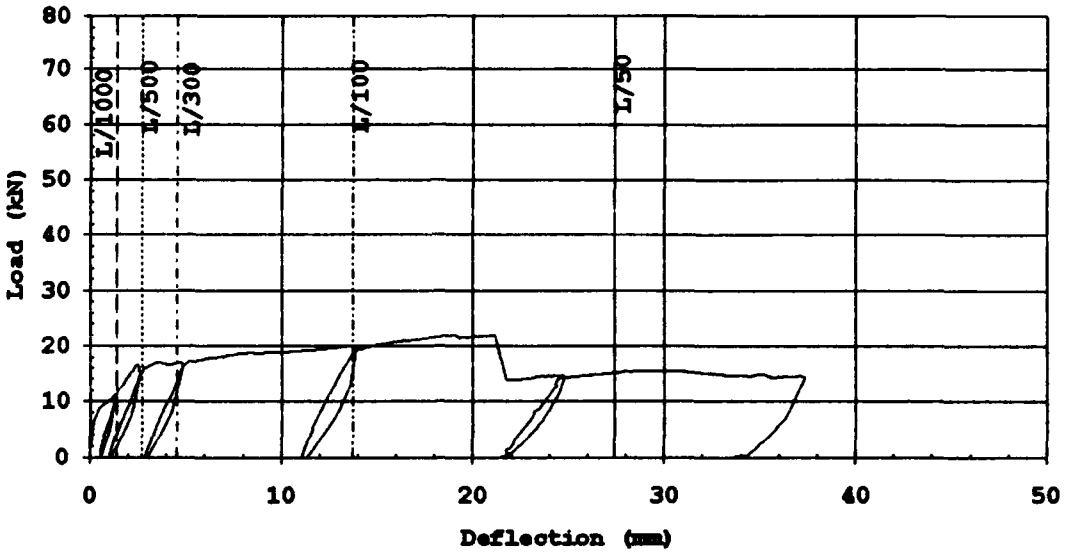


Figure B27. Load-Deflection Curve: Test Beam #8 - V64/9.0 mm/24

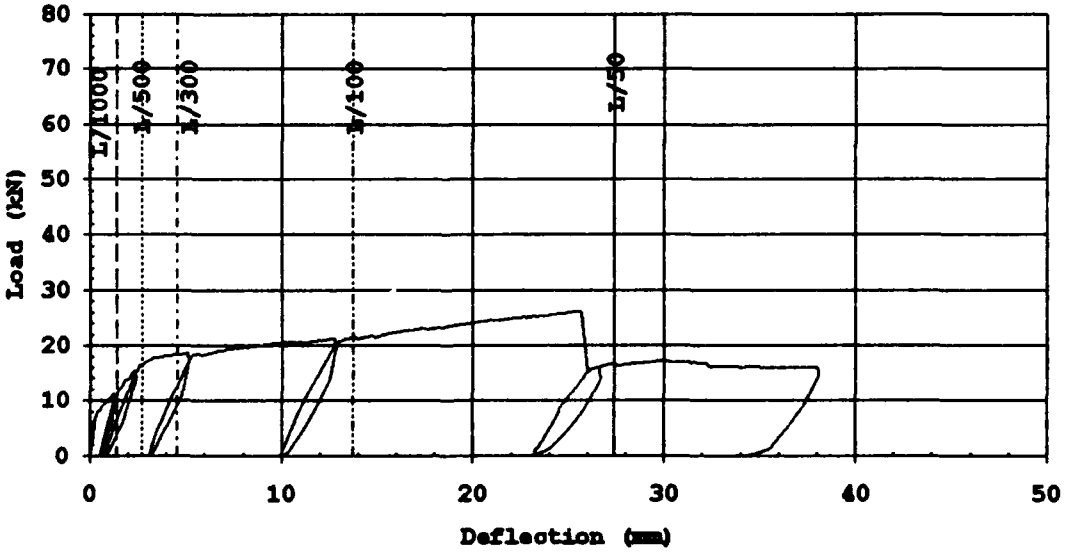


Figure B28. Load-Deflection Curve: Test Beam #9 - V96/9.0 mm/SR24

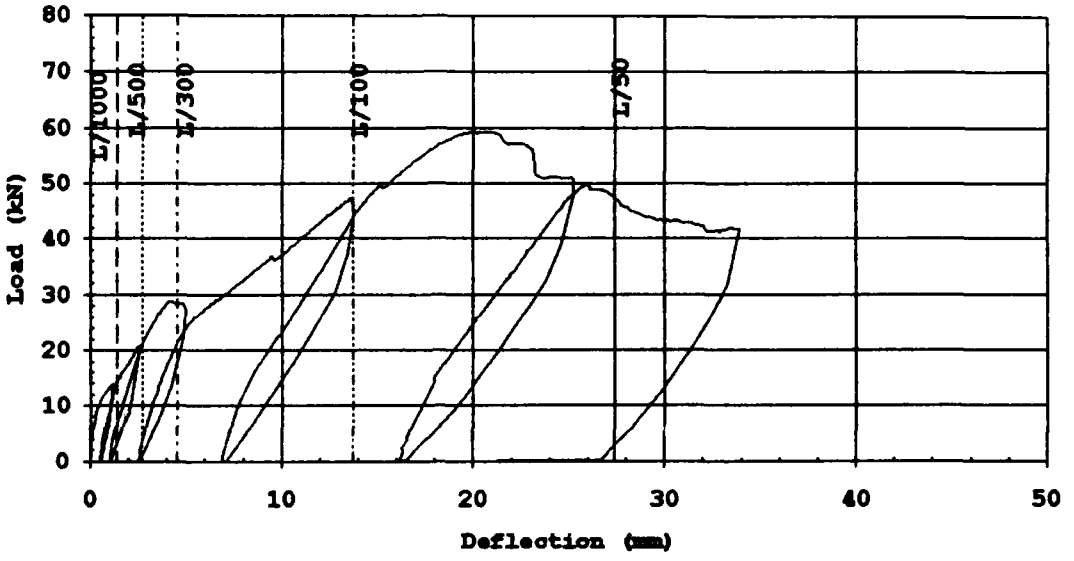


Figure B29. Load-Deflection Curve: Test Beam #10 - Smooth 13.0 mm Rod

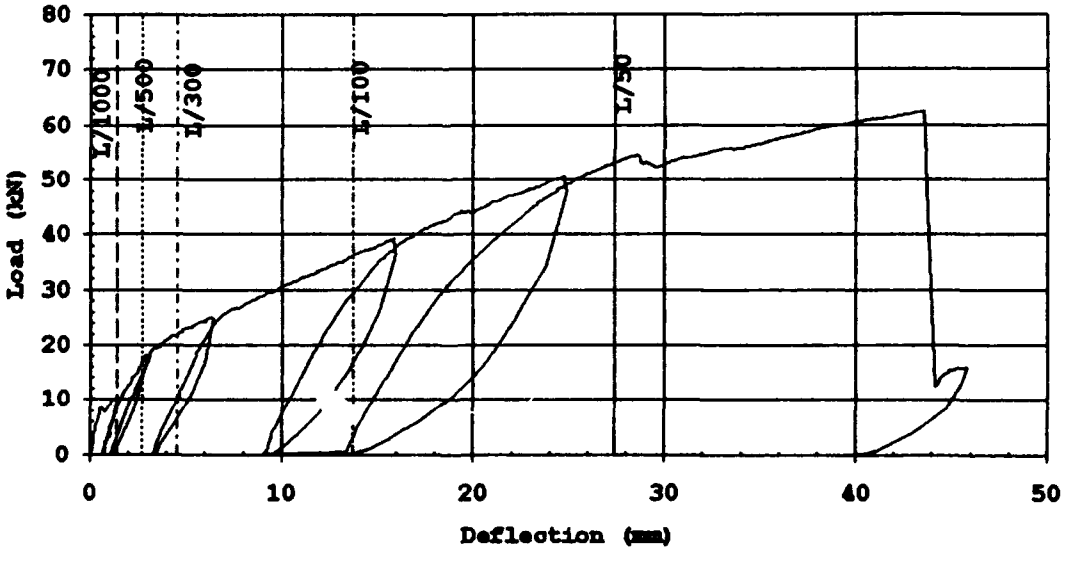


Figure B30. Load-Deflection Curve: Test Beam #11 - K96/9.0 mm/SR24

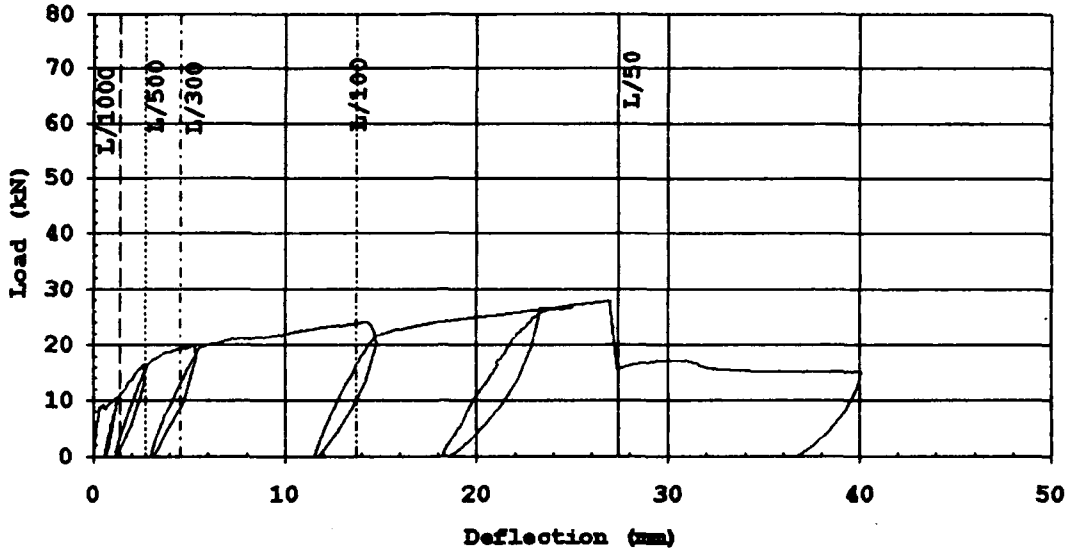


Figure B31. Load-Deflection Curve: Test Beam #12 - V96/9.0 mm/SR24

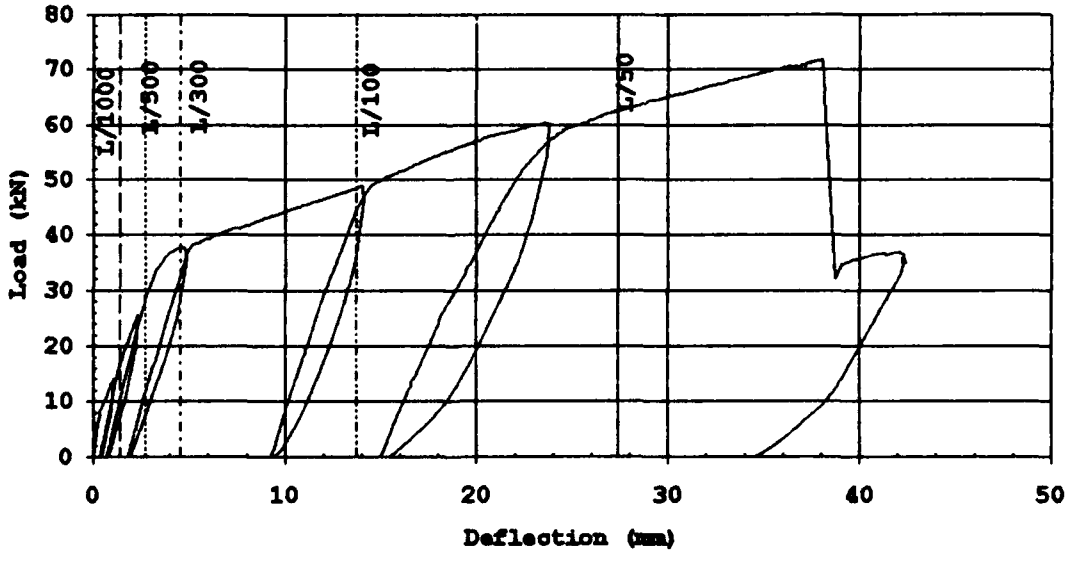


Figure B32. Load-Deflection Curve: Test Beam #13 - K96/13.0 mm/SR24

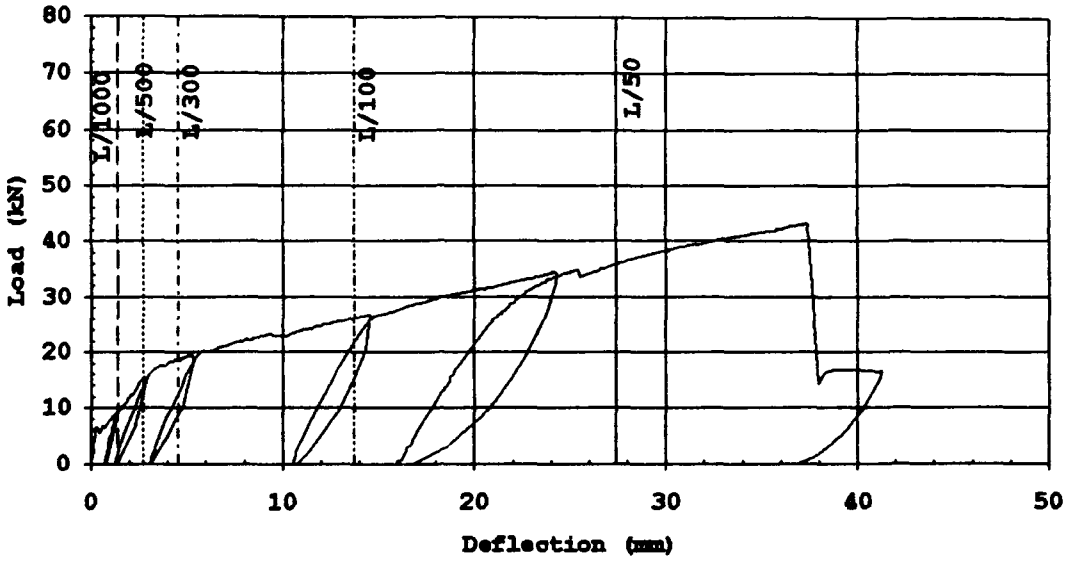


Figure B33. Load-Deflection Curve: Test Beam #14 - K48/9.0 mm/SR24

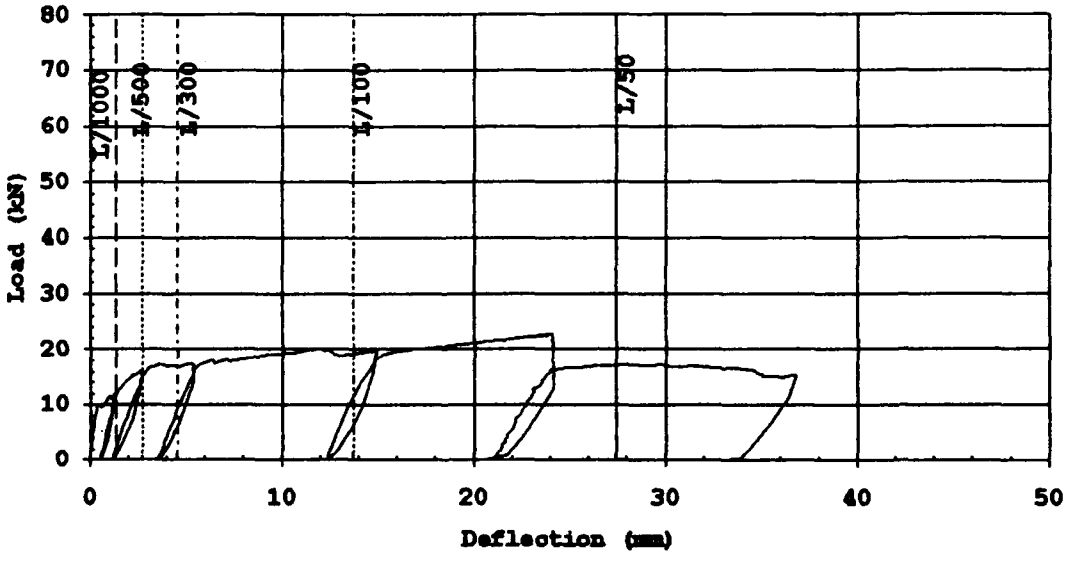


Figure B34. Load-Deflection Curve: Test Beam #15 - V64/9.0 mm/SR24

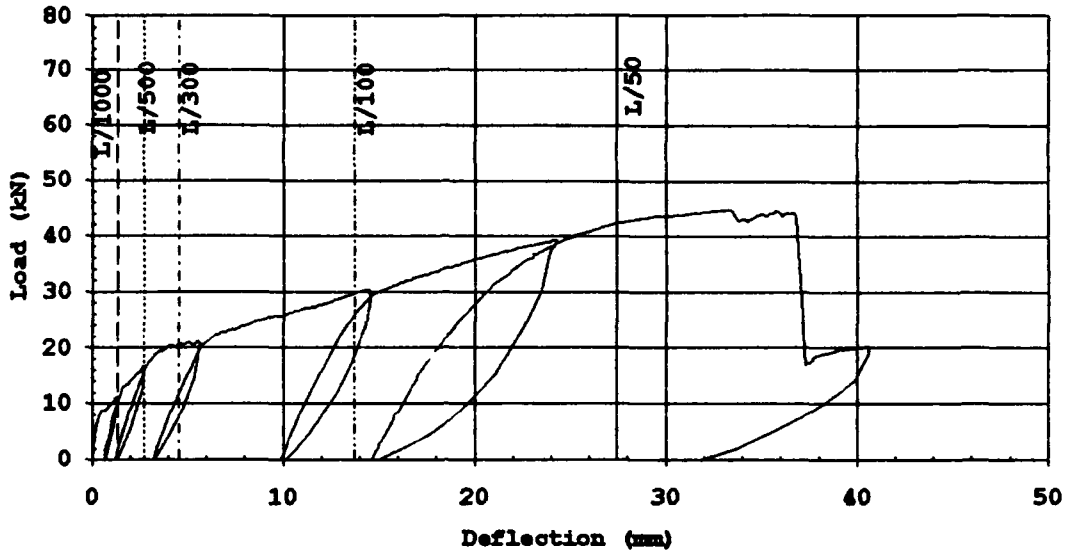


Figure B35. Load-Deflection Curve: Test Beam #16 - K64/9.0 mm/SR24

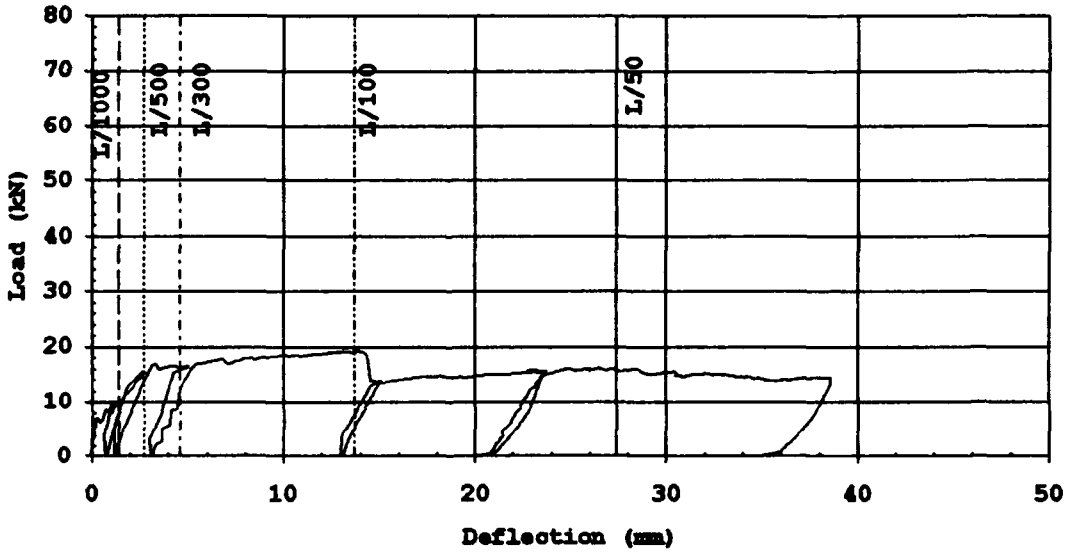


Figure B36. Load-Deflection Curve: Test Beam #17 - V48/9.0 mm/SR24

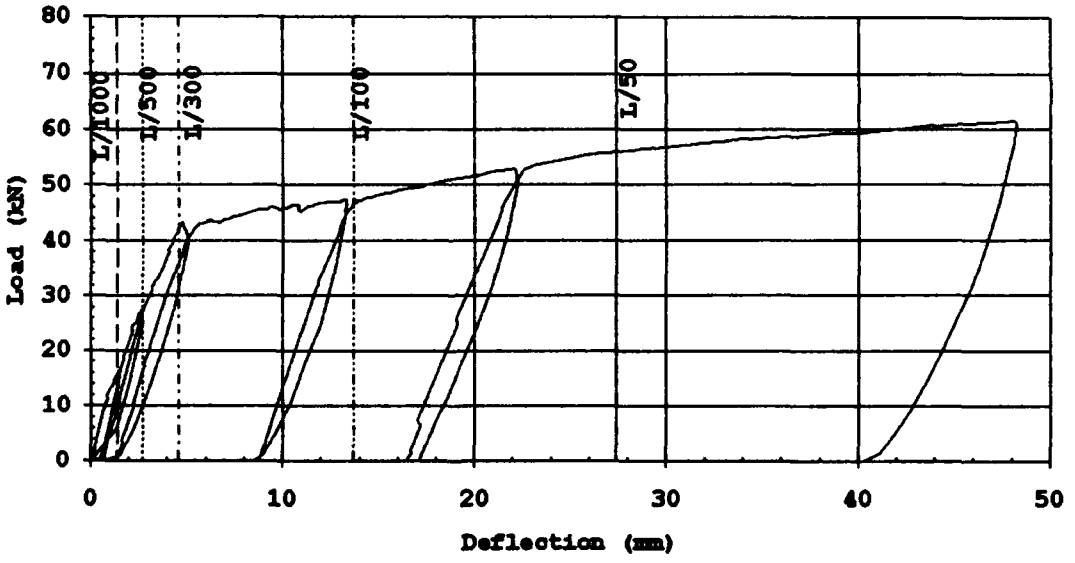


Figure B37. Load-Deflection Curve: Test Beam #18 - #5 Rebar

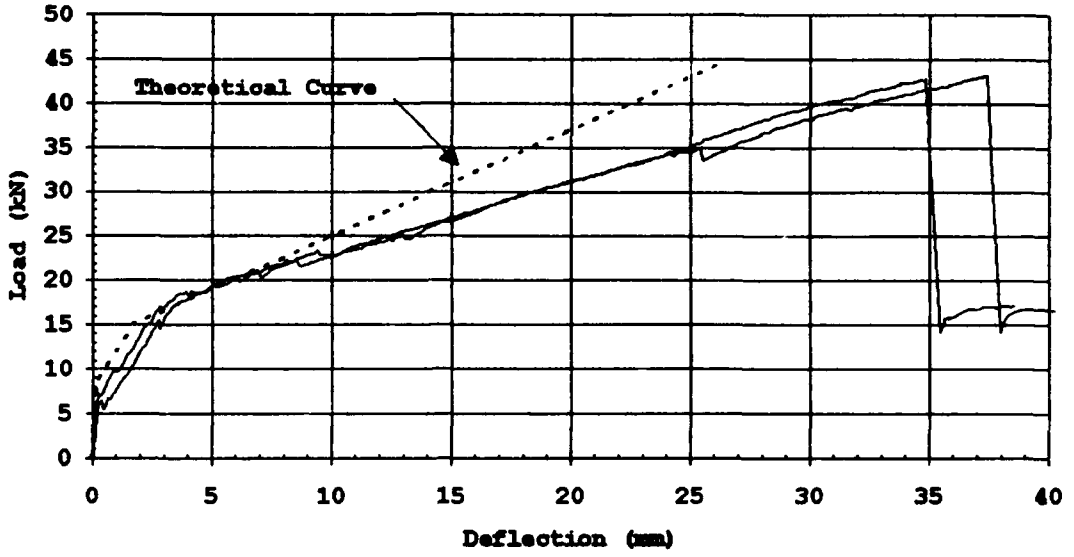


Figure B38. Experimental and Theoretical Load-Deflection Curves for Beams with K48/9.0 mm Hybrid Rod

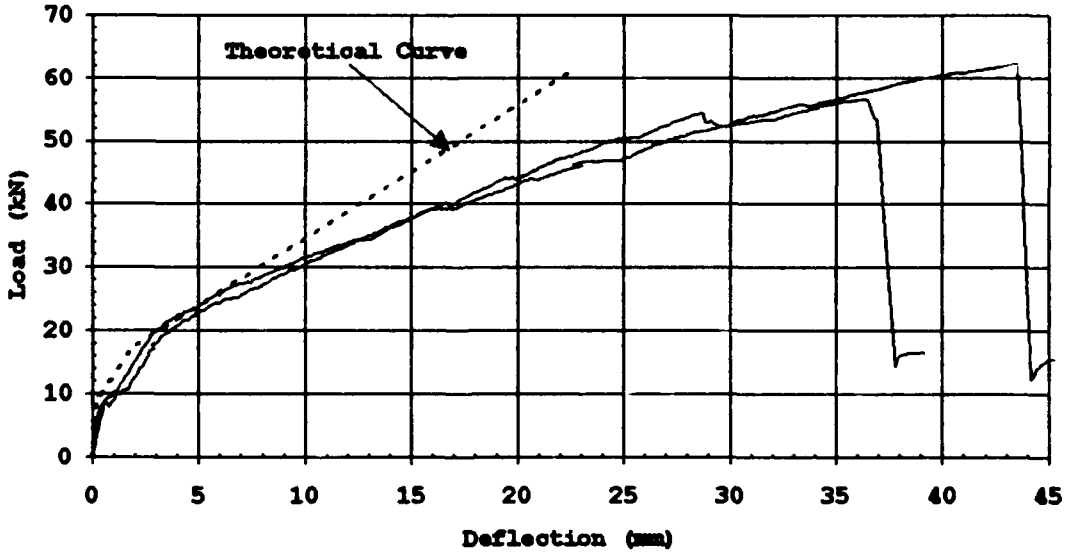


Figure B39. Experimental and Theoretical Load-Deflection Curves for Beams with K96/9.0 mm Hybrid Rod

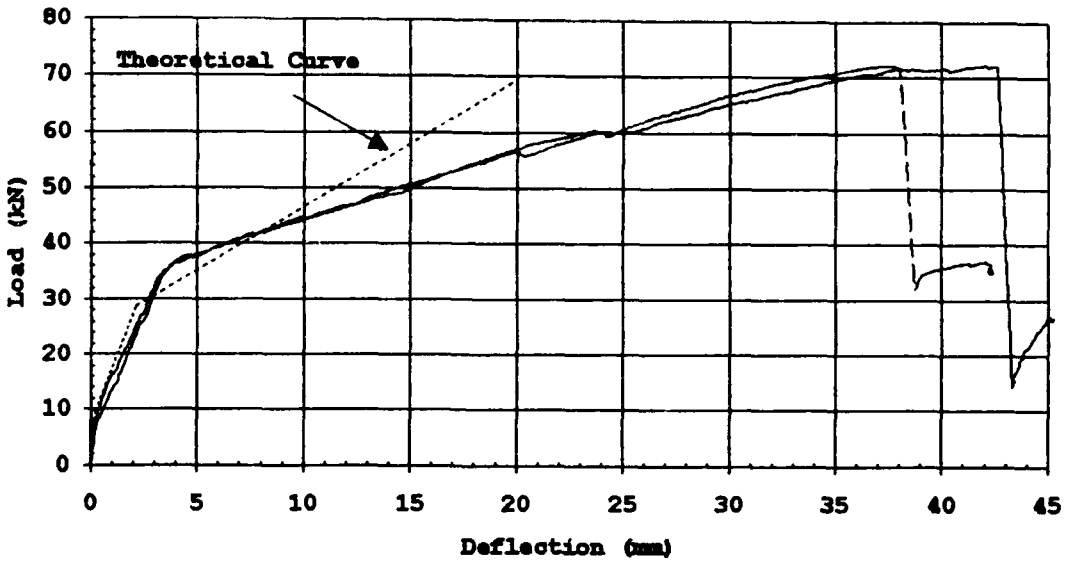


Figure B40. Experimental and Theoretical Load-Deflection Curves for Beams with K96/13.0 mm Hybrid Rod

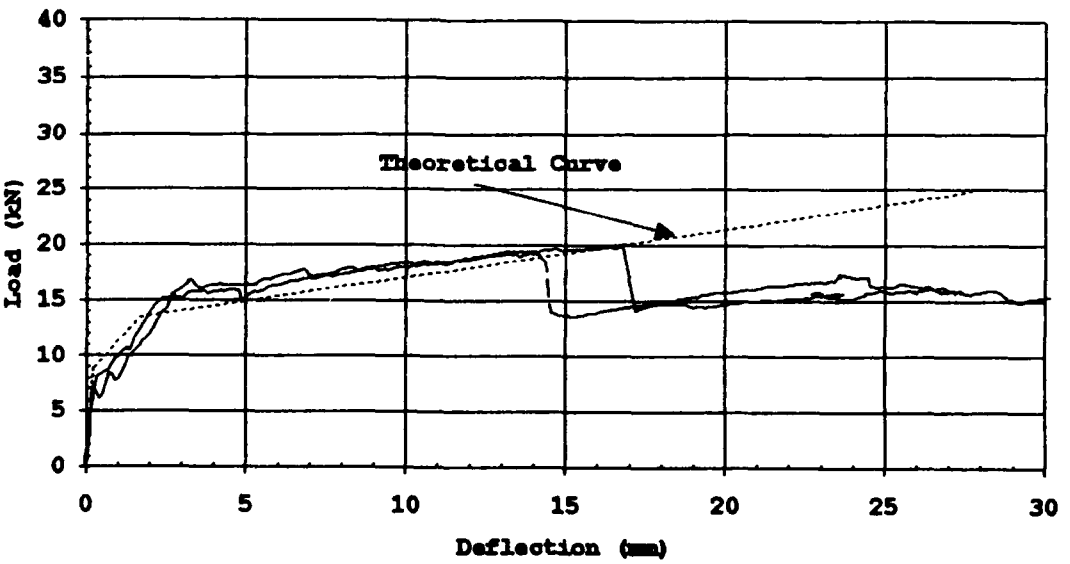


Figure B41. Experimental and Theoretical Load-Deflection Curves for Beams with V48/9.0 mm Hybrid Rod

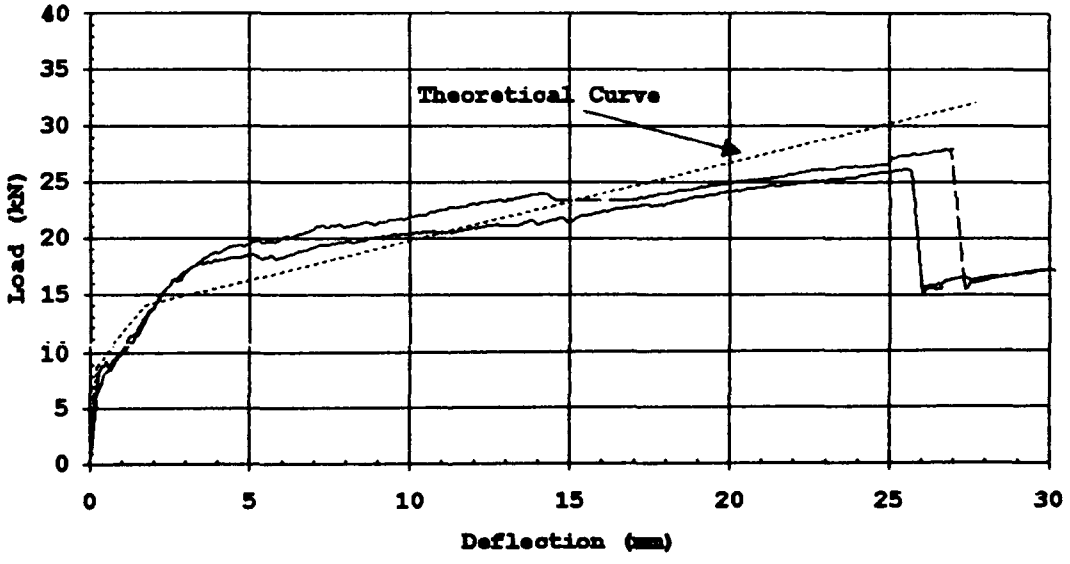


Figure B42. Experimental and Theoretical Load-Deflection Curves for Beams with V96/9.0 mm Hybrid Rod

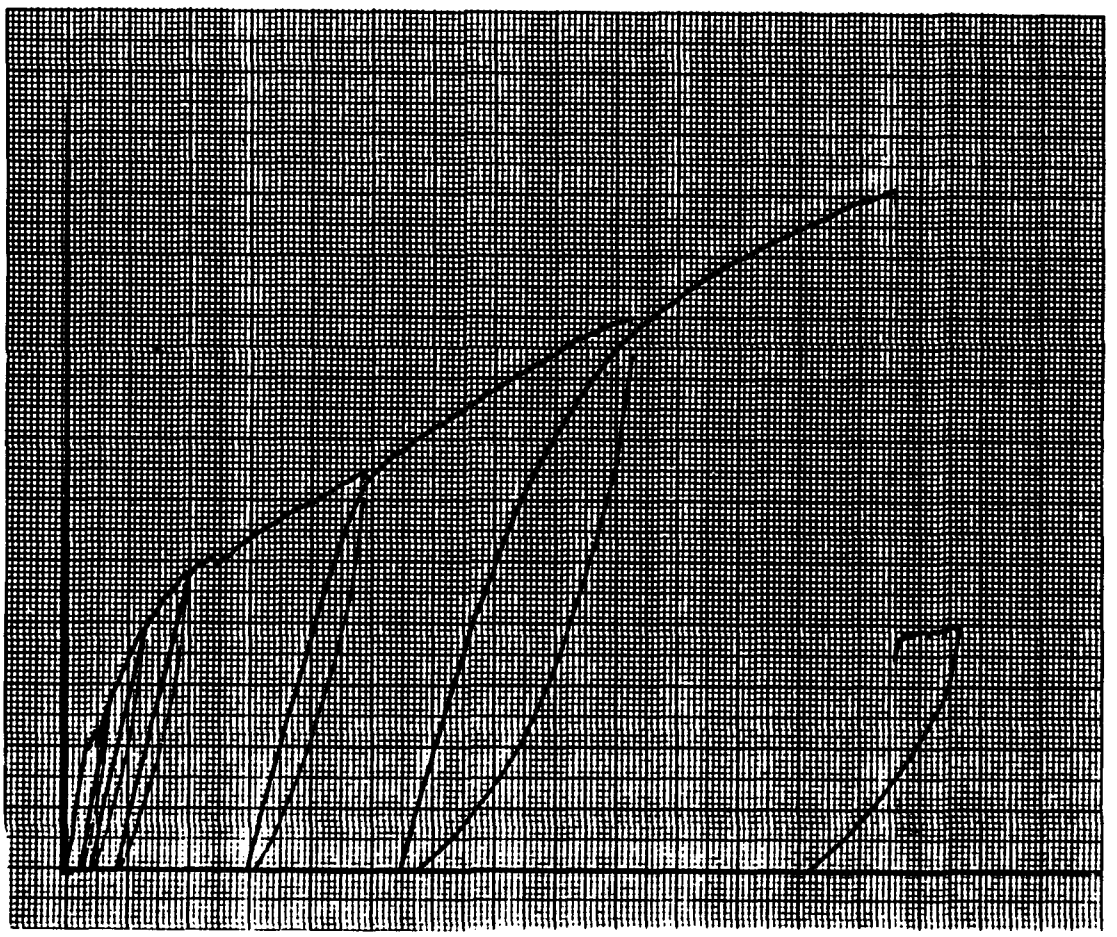

Figure B43. Sample of XY Plotter Data (Test #4 - K64/9.0 mm/ SR24)

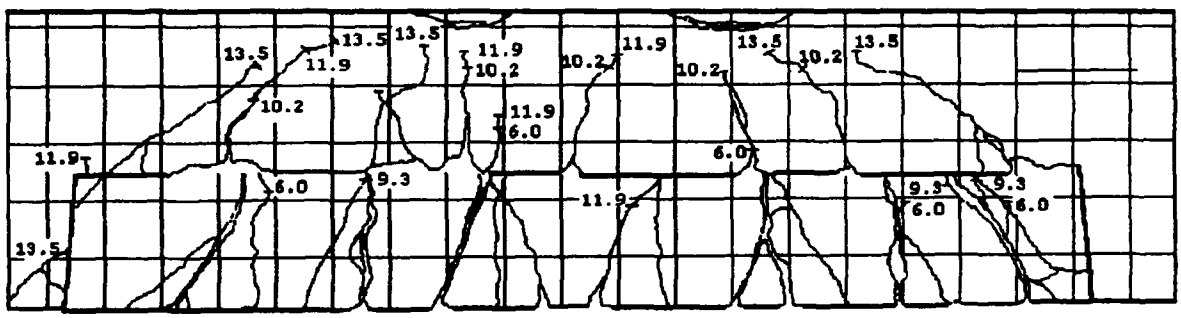


Figure B44. Crack Pattern Tracing: Test Beam #1 - #5 rebar

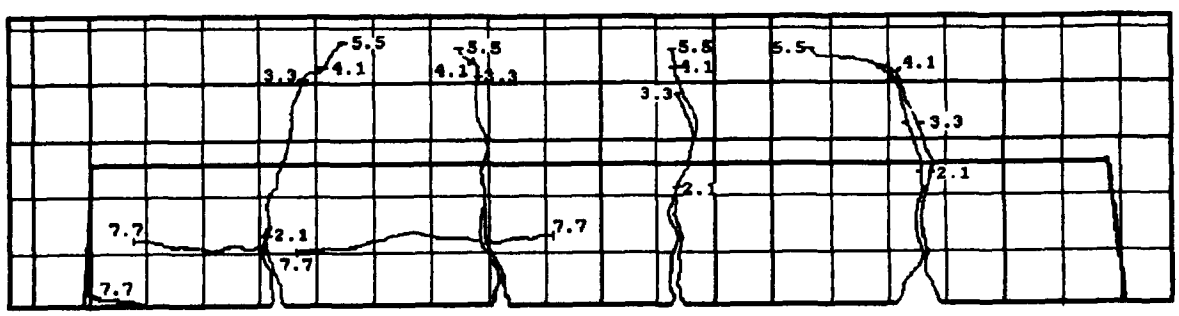


Figure B45. Crack Pattern Tracing: Test Beam #3 - K48/9.0 mm Hybrid Rod

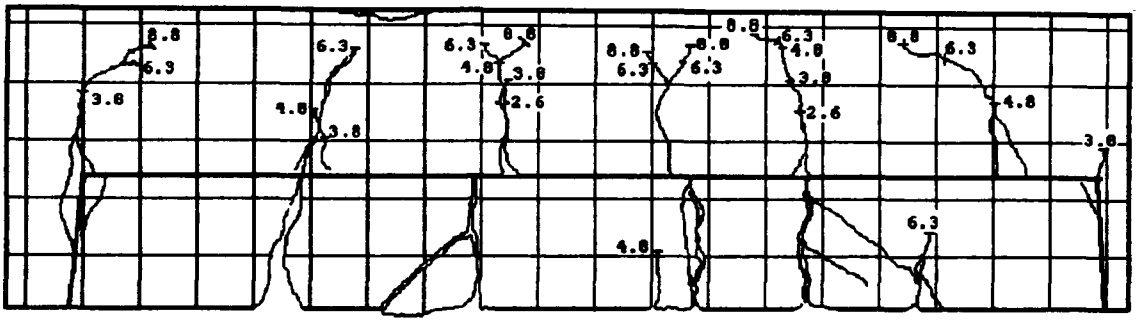


Figure B46. Crack Pattern Tracing: Test Beam #4 - K64/9.0 mm Hybrid Rod

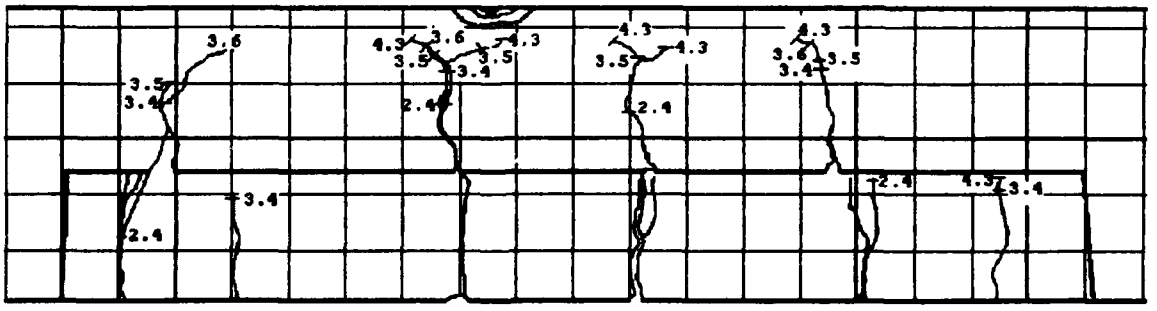


Figure B47. Crack Pattern Tracing: Test Beam #5 - V48/9.0 mm Hybrid Rod

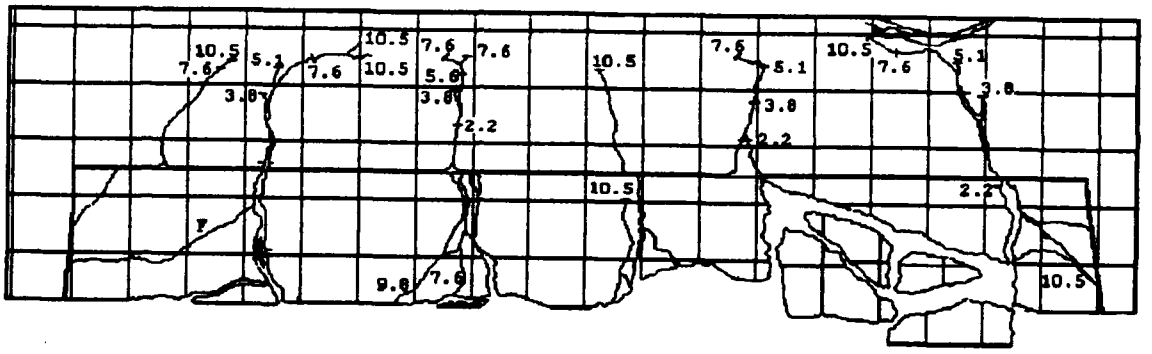


Figure B48. Crack Pattern Tracing: Test Beam #6 - K96/9.0 mm Hybrid Rod

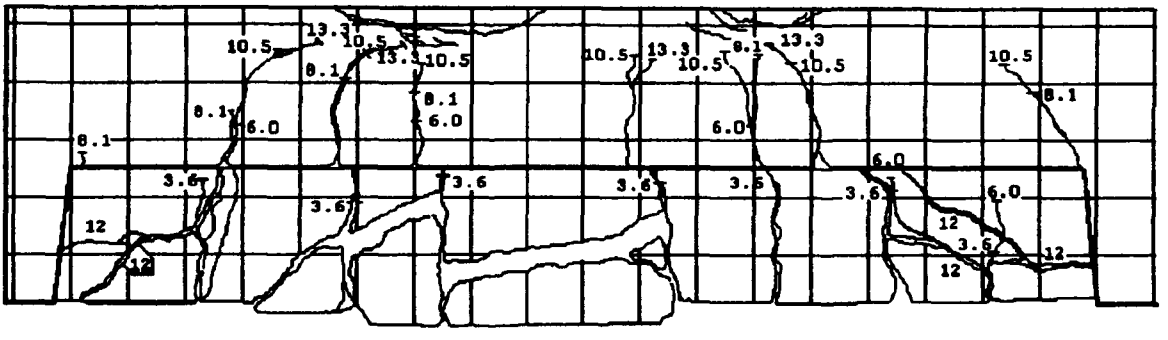


Figure B49. Crack Pattern Tracing: Test Beam #7 - K96/13.0 mm Hybrid Rod

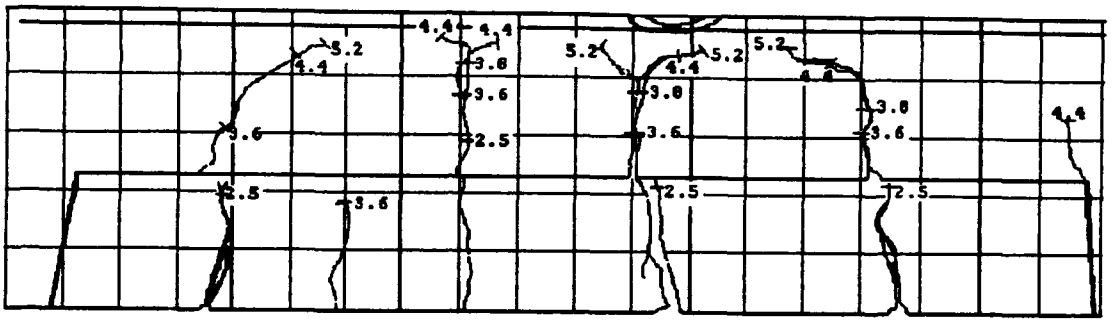


Figure B50. Crack Pattern Tracing: Test Beam # 8 - V64/9.0 mm Hybrid Rod

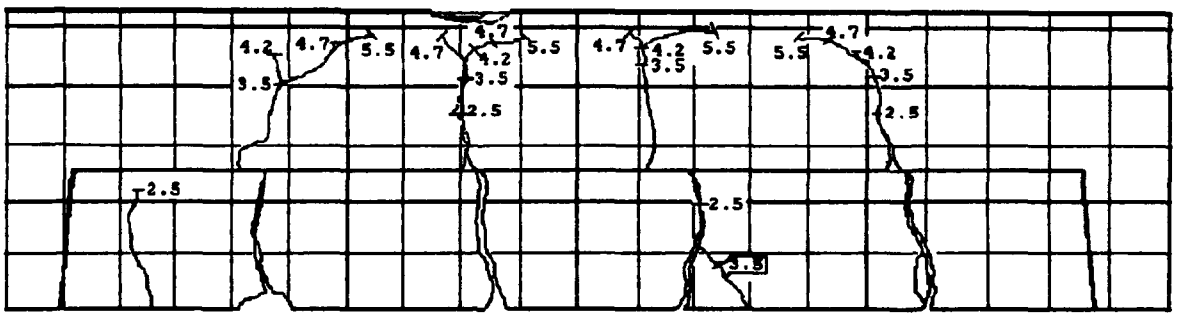


Figure B51. Crack Pattern Tracing: Test Beam #9 - V96/9.0 mm Hybrid Rod

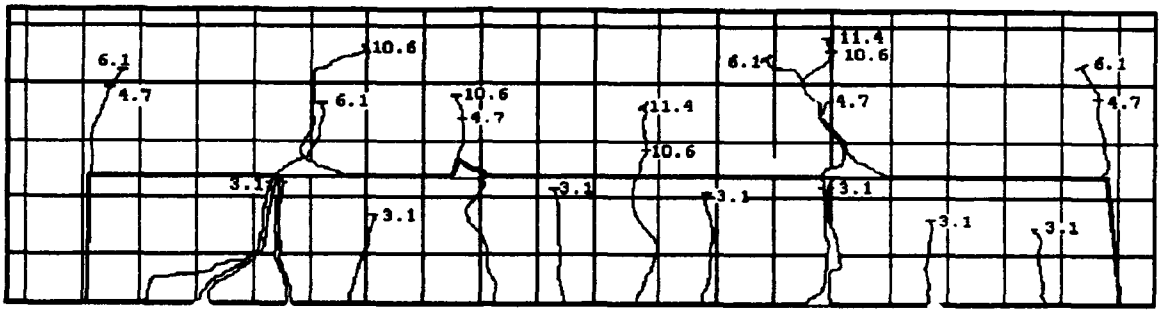


Figure B52. Crack Pattern Tracing: Test Beam #10 - Smooth 13.0 mm rod

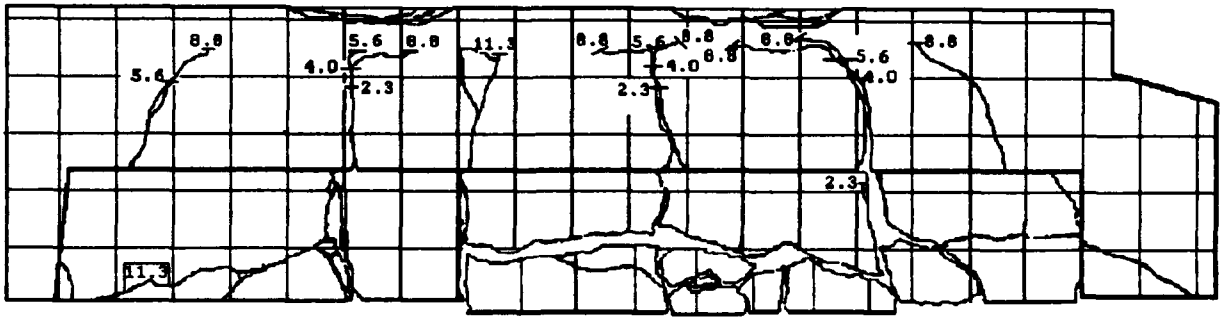


Figure B53. Crack Pattern Tracing: Test Beam #11 - K96/9.0 mm Hybrid Rod

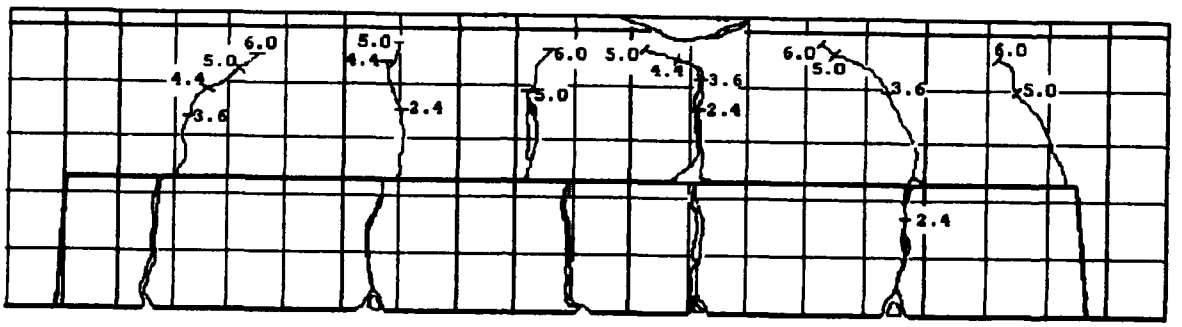


Figure B54. Crack Pattern Tracing: Test Beam #12 - V96/9.0 mm Hybrid Rod

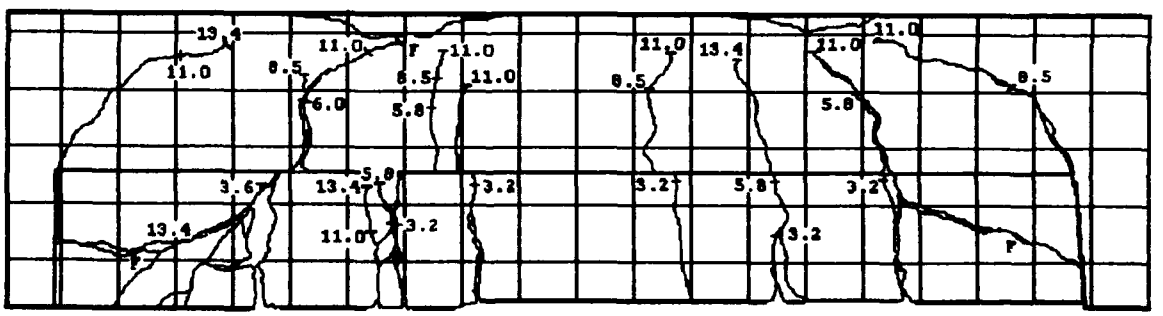


Figure B55. Crack Pattern Tracing: Test Beam # 13 - K96/13.0 mm Hybrid Rod

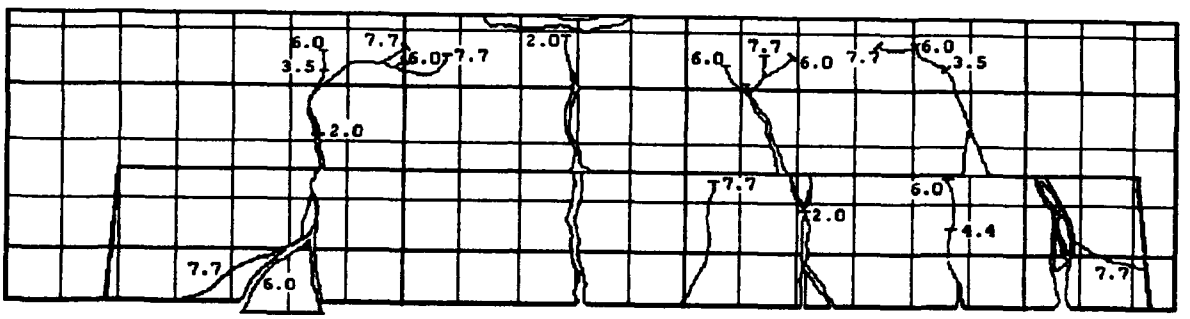


Figure B56. Crack Pattern Tracing: Test Beam #14 - K48/9.0 mm Hybrid Rod

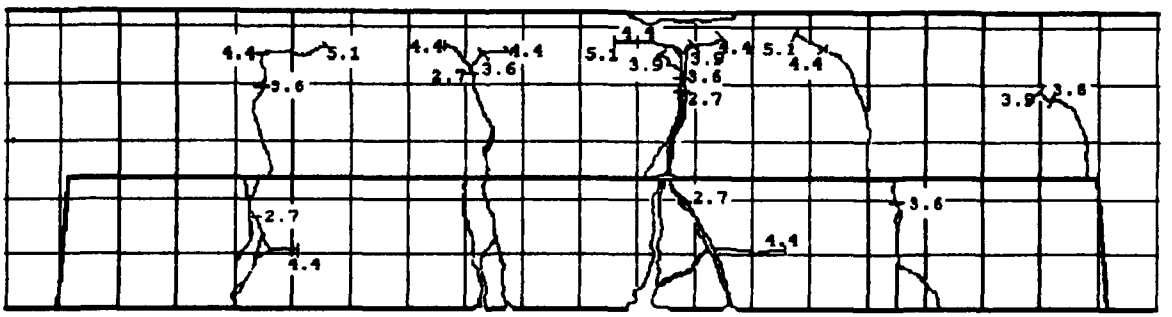


Figure B57. Crack Pattern Tracing: Test Beam #15 - V64/9.0 mm Hybrid Rod

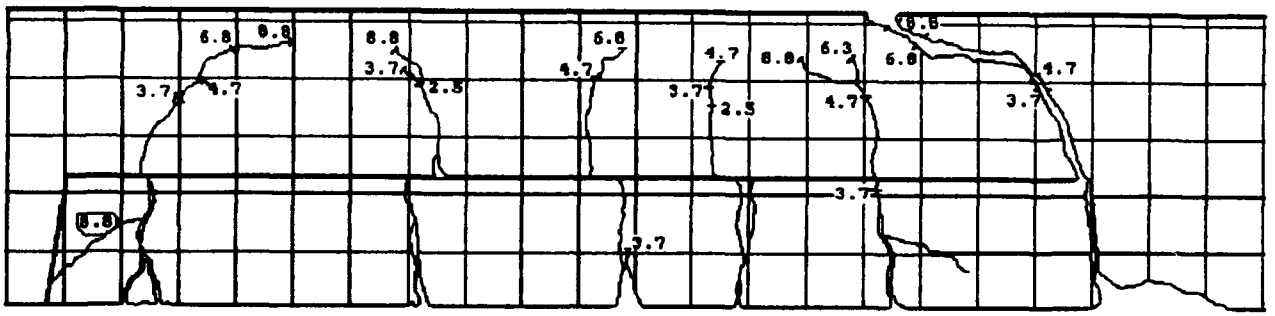


Figure B58. Crack Pattern Tracing: Test Beam #16 - K64/9.0 mm Hybrid Rod

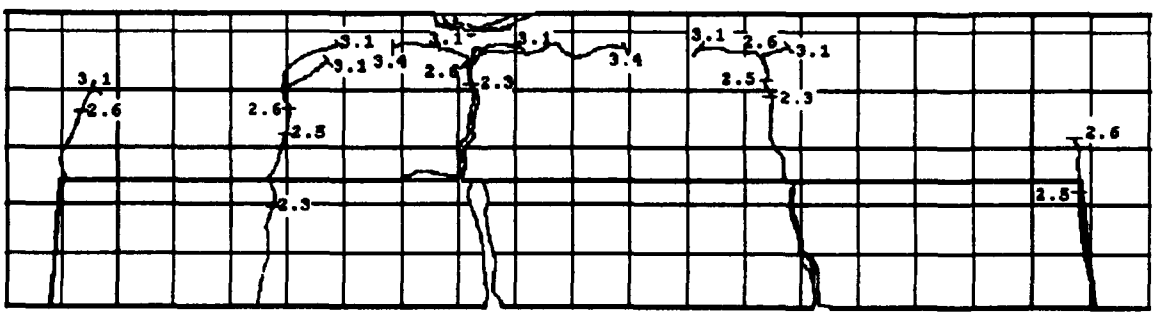


Figure B59. Crack Pattern Tracing: Test Beam #17 - V48/9.0 mm Hybrid Rod

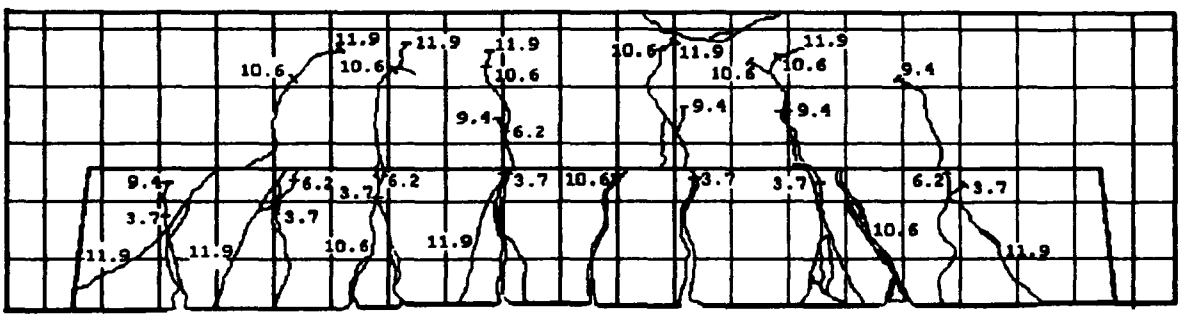


Figure B60. Crack Pattern Tracing: Test Beam #18 - #5 Rebar

# APPENDIX C

# SAMPLE CALCULATIONS

The calculations are based on the following assumptions for flexure (Nilson and Winter 1986);

- Perfect bond between concrete and hybrid rod.
- A cross section which was plane before loading remains plane under load.
- Bending stress at any point depends on the strain at that point given by the stress-strain diagram of the material.
- When stresses in the outer areas are smaller than the proportional limit, the beam behaves elastically.

The following sample calculation is done for a beam reinforced with a K48/9.0 mm/SR24 hybrid rod using the software package Mathcad 3.1.

Cross section dimensions are given in Chapter 4, Figure 15.

$b := 150 \cdot mm$

$h := 200 \cdot mm$

$d := 170 \cdot mm$

$d' := 25 \cdot mm$

$l := 1370 \cdot mm$

$q := 535 \cdot mm$

**ASSUMPTIONS: (Calculations are done in SI units)**

Properties of the concrete used;

Compressive strength,

$f'_c = 5200 \cdot psi$

$$f'_c = 35.853 \cdot \frac{newton}{mm^2}$$

$$\beta := 0.85 - 0.05 \cdot \left[ \frac{\frac{f'_c}{\left(\frac{newton}{mm^2}\right)} - 27.6}{6.89} \right]$$

$\beta_1 := if(\beta \geq 0.85, 0.85, if(\beta \leq 0.65, 0.65, \beta))$

$\beta_1 = 0.79$

Elastic Modulus of Concrete,

$$E_c := 4700 \cdot \sqrt{f'_c \cdot \frac{mm^2}{newton}} \cdot \frac{newton}{mm^2}$$

$$E_c = 2.814 \cdot 10^4 \cdot \frac{newton}{mm^2}$$

Modulus of rupture of Concrete;

$$f_r := 0.62 \cdot \sqrt{f'_c \cdot \frac{mm^2}{newton}} \cdot \frac{newton}{mm^2}$$

$$f_r = 3.71 \cdot \frac{newton}{mm^2}$$

Ultimate Concrete Strain

$\varepsilon_{cu} := 0.0035$

Properties of Hybrid Rod

Yield stress and elastic modulus of steel core,

$f_{yH} := 340 \cdot \frac{newton}{mm^2}$ This is the yield stress determined from the tensile testing.

$E_{sH} := 206000 \cdot \frac{newton}{mm^2}$ This is the elastic modulus determined from the tenile testing.

Ultimate stress and elastic modulus of FRP skin

$f_{uK} := 1489 \cdot \frac{newton}{mm^2}$

$E_{K} := 68400 \cdot \frac{newton}{mm^2}$

**Calculations for: K48/9/SR24**

Diameter and area of steel core;

$\phi := 9 \cdot mm$

$A_{\phi} := \pi \cdot \frac{(\phi)^2}{4}$

$A_{\phi} = 63.617 \cdot mm^2$

Area of FRP skin,

$A_{K48} := 33 \cdot mm^2$

Total area of hybrid rod,

$A_{H} := A_{\phi} + A_{K48}$

$A_{H} = 96.617 \cdot mm^2$

Volume percentage of steel in hybrid rod;

$V_{s} := \frac{A_{\phi}}{A_{H}}$

$V_{s} = 0.658$

Strain in hybrid rod at steel core yield;

$\varepsilon_{H} := \frac{f_{yH}}{E_{sH}}$

$\varepsilon_{H} = 0.00165$

Using the law of mixtures, the stress in the hybrid rod is found at the yield point of the steel core;

$$f_H := \left[\left(\frac{A_\phi}{A_H}\cdot E_{sH}\right) + \left(\frac{A_{K48}}{A_H}\cdot E_K\right)\right]\cdot \varepsilon_H$$

$$f_H = 262.4\cdot\frac{newton}{mm^2}$$

From the theoretical stress, $f_H$, an elastic modulus is calculated;

$$E_H := \frac{f_H}{\varepsilon_H}$$

$$E_H = 159002.2\cdot\frac{newton}{mm^2}$$

Properties of the compression steel, 2 - #3 rebar;

$$A'_s := 142\cdot mm^2$$

$$E_s := 200000\cdot\frac{newton}{mm^2}$$

$$fy_{compsteel} := 60000\cdot psi$$

$$fy_{compsteel} = 413.686\cdot\frac{newton}{mm^2}$$

**PART A - Calculation of Cracking Moment (using transformed section):**

Properties of T-section of beam (see Chapter 4, Figure ):

$$h_2 := 3.5\cdot in$$

$$h_1 := h - h_2$$

$$h_1 = 111.1\cdot mm$$

$$b_1 := b - (1.5\cdot in)\cdot 2$$

$$b_1 = 73.8\cdot mm$$

Modular Ratio of the hybrid rod and compression steel;

$$n_H := \frac{E_H}{E_c} \qquad n_H = 5.65 \qquad \text{Hybrid Rod}$$

$$n_s := \frac{E_s}{E_c} \qquad n_s = 7.107 \qquad \text{Compression Steel}$$

Using the First Moment of Area, the centroid and the gross moment of inertia is found;

$$y' := \frac{b \cdot h_1 \cdot \frac{h_1}{2} + b_1 \cdot h_2 \cdot \left(h - \frac{h_2}{2}\right) + (n_H - 1) \cdot A_H \cdot d + (n_s - 1) \cdot A'_s \cdot d'}{b \cdot h_1 + b_1 \cdot h_2 + (n_H - 1) \cdot A_H + (n_s - 1) \cdot A'_s}$$

$$y' = 83.298 \cdot mm$$

$$I_{A1} := \frac{b \cdot h_1^3}{12} + b \cdot h_1 \cdot \left(\frac{h_1}{2} - y'\right)^2$$

$$I_{A2} := \frac{b_1 \cdot h_2^3}{12} + b_1 \cdot h_2 \cdot \left(h - \frac{h_2}{2} - y'\right)^2$$

$$I_{As} := (n_H - 1) \cdot A_H \cdot (d - y')^2$$

$$I_{A's} := (n_s - 1) \cdot A'_s \cdot (d' - y')^2$$

$$I_{Gt} := I_{A1} + I_{A2} + I_{As} + I_{A's}$$

$$I_{Gt} = 7.487 \cdot 10^7 \cdot mm^4$$

Distance from the extreme fiber in tension and the center of gravity of the transformed section;

$$y_t := h - y'$$

$$y_t = 116.702 \cdot mm$$

Cracking Moment;

$$M_{cr} := \frac{I_{Gt} \cdot f_r}{y_t}$$

$$M_{cr} = 2.382 \cdot 10^6 \cdot newton \cdot mm$$

Load at cracking;

$$Cracking_Force := 2 \cdot \frac{M_{cr}}{q}$$

$$Cracking_Force = 8903.25 \cdot newton$$

**PART B - Moment and Load at Steel Core Yield**

Using strain compatibility and assuming concrete is still elastic, solve for location of neutral axis, c ;

$$C_c = 0.5 \cdot f_c \cdot b \cdot c \qquad \text{where} \qquad f_c = \varepsilon_c \cdot E_c$$

$$\varepsilon_c = \frac{\varepsilon_H \cdot c}{d - c}$$

$$C_{cs} = E_s \cdot A'_s \cdot \varepsilon'_s - A'_s \cdot f_{css}$$

where $\varepsilon'_s = \varepsilon_H \cdot \frac{c - d'}{d - c}$

$$f_{css} = \frac{f_c \cdot (c - d')}{c}$$

$$T = A_H \cdot \left[ V_s \cdot f_{yH} + (1 - V_s) \cdot E_K \cdot \varepsilon_H \right]$$

Using the equilibrium equation and solving in terms of c;

$$C_c + C_{cs} - T = 0$$

$$\frac{0.5 \cdot \varepsilon_H \cdot b \cdot c^2 \cdot E_c}{d - c} + E_s \cdot A'_s \cdot \varepsilon_H \cdot \frac{c - d'}{d - c} - \frac{A'_s \cdot E_c \cdot \varepsilon_H \cdot (c - d')}{d - c}$$

$$- A_H \cdot \left[ V_s \cdot f_{yH} + (1 - V_s) \cdot E_V \cdot \varepsilon_H \right] = 0$$

A quadratic expressions is formed with the following coeffecients;

$x := 0.5 \cdot \varepsilon_H \cdot b \cdot E_c$

$y := E_s \cdot A'_s \cdot \varepsilon_H - A'_s \cdot E_c \cdot \varepsilon_H + A_H \cdot \left[ V_s \cdot f_{yH} + (1 - V_s) \cdot E_K \cdot \varepsilon_H \right]$

$z := A'_s \cdot \varepsilon_H \cdot d' \cdot (E_c - E_s) - A_H \cdot d \cdot \left[ V_s \cdot f_{yH} + (1 - V_s) \cdot E_K \cdot \varepsilon_H \right]$

Location of neutral axis (N.A)

$discrim := y^2 - 4 \cdot x \cdot z$

$$c_y := \frac{-y + \sqrt{discrim}}{2 \cdot x}$$

$c_y = 30.768 \cdot mm$

Strain in concrete;

$$\varepsilon_{cy} := \frac{\varepsilon_H \cdot c_y}{d - c_y}$$

$\varepsilon_{cy} = 0.00036$

Strain in Compression Steel;

$$\varepsilon'_s := \varepsilon_H \cdot \frac{c_y - d'}{d - c_y}$$

$\varepsilon'_s = 0.00007$

Now, calculating the Moment at Steel Yield;

$$C_c := 0.5 \cdot \varepsilon_{cy} \cdot E_c \cdot b \cdot c_y$$

$$C_{cs} := E_s \cdot A'_s \cdot \varepsilon'_s - A'_s \cdot E_c \cdot \varepsilon_H \cdot \frac{c_y - d'}{d - c_y}$$

$$M_y := C_c \cdot \left(d - \frac{c_y}{3}\right) + C_{cs} \cdot (d - d')$$

$$M_y = 4.03 \cdot 10^6 \cdot \text{newton} \cdot \text{mm}$$

$$\text{Yield_Force} := 2 \cdot \frac{M_y}{q}$$

$$\text{Yield_Force} = 15049.56 \cdot \text{newton}$$

**PART C - Calculating the Ultimate Moment:**

Using strain compatibility and stress block, solve for neutral axis;

Assume d' > c, with top steel in tension;

$$C_c = 0.85 \cdot f'_c \cdot b \cdot \beta_1 \cdot c$$

$$T_{cs} = E_s \cdot A'_s \cdot \varepsilon'_s \qquad \text{where} \qquad \varepsilon'_s = \varepsilon_{cu} \cdot \frac{d' - c}{c}$$

$$T = A_H \cdot \left[V_s \cdot f_{yH} + \left(1 - V_s\right) \cdot E_K \cdot \varepsilon_H\right] \qquad \text{where} \qquad \varepsilon_H = \varepsilon_{cu} \cdot \frac{d - c}{c}$$

Using the equilibrium equation and solving in terms of c;

$$C_c - T_{cs} - T = 0$$

$$0.85 \cdot f'_c \cdot b \cdot \beta_1 \cdot c - E_s \cdot A'_s \cdot \varepsilon_{cu} \cdot \frac{d' - c}{c} - A_H \cdot \left[V_s \cdot f_{yH} + \left(1 - V_s\right) \cdot E_K \cdot \varepsilon_{cu} \cdot \frac{d - c}{c}\right] = 0$$

A quadratic expressions is formed with the following coeffecients;

$$x := 0.85 \cdot f'_c \cdot b \cdot \beta_1$$

$$y := E_s \cdot A'_s \cdot \varepsilon_{cu} - A_H \cdot V_s \cdot f_{yH} + A_H \cdot \left(1 - V_s\right) \cdot E_K \cdot \varepsilon_{cu}$$

$$z := \varepsilon_{cu} \cdot \left[-E_s \cdot A'_s \cdot d' - A_H \cdot \left(1 - V_s\right) \cdot E_K \cdot d\right]$$

Location of neutral axia,

$$\text{discrim} := y^2 - 4 \cdot x \cdot z$$

$$c := \frac{-y + \sqrt{\text{discrim}}}{2 \cdot x}$$

$$c = 22.789 \cdot \text{mm}$$

$$a := \beta_1 \cdot c$$

$$a = 18.006 \cdot mm$$

Strain in the hybrid rod

$$\varepsilon_h := \frac{\varepsilon_{cu}}{c} \cdot (d - c)$$

$$\varepsilon_h = 0.0226$$

Strain in Compression steel;

(steel is actually in tension)

$$\varepsilon'_s := \varepsilon_{cu} \cdot \frac{d' - c}{c}$$

$$\varepsilon'_s = 0.00034$$

Calculating the Ultimate Moment;

$$C_c := 0.85 \cdot f'_c \cdot b \cdot a \qquad T_{cs} := E_s \cdot \varepsilon'_s \cdot A'_s$$

$$M_U := \left[ C_c \cdot \left( d - \frac{a}{2} \right) - T_{cs} \cdot (d - d') \right]$$

$$M_U = 1.19 \cdot 10^7 \cdot newton \cdot mm$$

Load at ultimate failure

$$Ultimate_Force := 2 \cdot \frac{M_U}{q}$$

$$Ultimate_Force = 44309.93 \cdot newton$$

**PART D - Deflection at Cracking, Steel Yield and Ultimate:**

An increment method is used for deflection calculations.

Increment for deflection calculation;

$N := 20$ # of increments from support to center of beam.

$i := 1..N$

$$x_i := \frac{1}{2 \cdot N} \cdot i$$

Stress and strain in concrete at cracking load

$$f_{c_cr} := \frac{f_r \cdot y'}{y_t} \qquad \varepsilon_{c_cr} := \frac{f_{c_cr}}{E_c}$$

$$f_{c_cr} = 2.65 \cdot \frac{newton}{mm^2} \qquad \varepsilon_{c_cr} = 0.000094$$

Rotation at cracking load

$$\phi_{cr} := \frac{\varepsilon_{c_cr}}{y'}$$

$$\phi_{cr} = 1.13 \cdot 10^{-6} \cdot \frac{rad}{mm}$$

Slope of Moment-Rotation curve up to cracking

$$eq_slope_{cr} := \frac{M_{cr}}{\phi_{cr}}$$

$$eq_slope_{cr} = 2.107 \cdot 10^{12} \cdot newton \cdot mm^2$$

Rotation at steel core yield

$$\phi_y := \frac{\varepsilon_{cy}}{c_y}$$

$$\phi_y = 1.185 \cdot 10^{-5} \cdot \frac{rad}{mm}$$

Slope of Moment-Rotation curve from cracking to steel core yield

$$eq_slope_y := \frac{M_y - M_{cr}}{\phi_y - \phi_{cr}}$$

$$eq_slope_y = 1.533 \cdot 10^{11} \cdot newton \cdot mm^2$$

$$b_y := M_y - eq_slope_y \cdot \phi_y$$

$$b_y = 2.208 \cdot 10^{6} \cdot newton \cdot mm$$

Rotation at ultimate

$$\phi_u := \frac{\varepsilon_{cu}}{c}$$

$$\phi_u = 1.536 \cdot 10^{-4} \cdot \frac{rad}{mm}$$

Slope of Moment-Rotation curve from steel core yield to ultimate load

$$eq_slope_u := \frac{M_U - M_y}{\phi_u - \phi_y}$$

$$eq_slope_u = 5.523 \cdot 10^{10} \cdot newton \cdot mm^2$$

$$b_u := M_U - eq_slope_u \cdot \phi_u$$

$$b_u = 3.371 \cdot 10^{6} \cdot newton \cdot mm$$

DEFLECTION AT CRACKING

$$P := \frac{Cracking_Force}{2}$$ Shear Force along the length of the beam from support to load.

Moment equation in terms of an x distance along the length of the beam;

$$M(x) := if(x \le q, P \cdot x, P \cdot q)$$

Curvature equation in terms of an x distance along the length of the beam;

$$curvature(x) := if\left(M(x) \le M_{cr}, \frac{M(x)}{eq_slope_{cr}}, if\left(M(x) \le M_y, \frac{M(x) - b_y}{eq_slope_y}, \frac{M(x) - b_u}{eq_slope_u}\right)\right)$$

Calculation of the area underneath the curvature equation at each increment;

$$curvature_area_i := \frac{curvature\left(x_{i-1}\right) + curvature\left(x_i\right)}{2} \cdot \left(x_i - x_{i-1}\right)$$

Slope at each increment;

$$\theta_i := curvature_area_{(N+1)-i}$$

$$\theta_i := \theta_{i-1} + curvature_area_{(N+1)-i}$$

Area underneath the slope equation at each increment;

$$slope_area_i := \frac{\theta_{(N+1)-i} + \theta_{N-i}}{2} \cdot \left(x_i - x_{i-1}\right)$$

Finally, the deflection is found at each increment, with the last increment being the maximum deflection at the center;

$$deflection_i := slope_area_i$$

$$deflection_i := deflection_{i-1} + slope_area_i$$

$$\Delta_at_Cracking := deflection_N$$

$$\Delta_at_Cracking = 0.21 \cdot mm$$

To determine if the increment deflection calculation procedure is correct, an exact solution for deflection can be used to check the cracking deflection value, since the concrete beam is still in the elastic region;

$$\Delta_{cr} := \frac{\frac{Cracking_Force}{2} \cdot q}{24 \cdot E_c \cdot I_{Gt}} \cdot \left(3 \cdot l^2 - 4 \cdot q^2\right)$$

$$\Delta_{cr} = 0.21 \cdot mm$$

The increment method deflection matches the exact solution deflection, therefore, the procedure is used to compute the deflections at steel core yield and ultimate.

DEFLECTION AT STEEL CORE YIELD

$$P := \frac{Yield_Force}{2}$$

$$M(x) := if(x \le q, P \cdot x, P \cdot q)$$

$$curvature(x) := if\left(M(x) \le M_{cr}, \frac{M(x)}{eq_slope_{cr}}, if\left(M(x) \le M_{y}, \frac{M(x) - b_{y}}{eq_slope_{y}}, \frac{M(x) - b_{u}}{eq_slope_{u}}\right)\right)$$

$$curvature_area_i := \frac{curvature(x_{i-1}) + curvature(x_i)}{2} \cdot (x_i - x_{i-1})$$

$$\theta_i := curvature_area_{(N+1)-i}$$

$$\theta_i := \theta_{i-1} + curvature_area_{(N+1)-i}$$

$$slope_area_i := \frac{\theta_{(N+1)-i} + \theta_{N-i}}{2} \cdot (x_i - x_{i-1})$$

$$deflection_i := slope_area_i$$

$$deflection_i := deflection_{i-1} + slope_area_i$$

$$\Delta_at_Yield := deflection_N \qquad \Delta_at_Yield = 1.77 \cdot mm$$

DEFLECTION AT ULTIMATE

$$P := \frac{Ultimate_Force}{2}$$

$$M(x) := if(x \le q, P \cdot x, P \cdot q)$$

$$curvature(x) := if\left(M(x) \le M_{cr}, \frac{M(x)}{eq_slope_{cr}}, if\left(M(x) \le M_{y}, \frac{M(x) - b_{y}}{eq_slope_{y}}, \frac{M(x) - b_{u}}{eq_slope_{u}}\right)\right)$$

$$curvature_area_i := \frac{curvature(x_{i-1}) + curvature(x_i)}{2} \cdot (x_i - x_{i-1})$$

$$\theta_i := curvature_area_{(N+1)-i}$$

$$\theta_i := \theta_{i-1} + curvature_area_{(N+1)-i}$$

$$slope_area_i := \frac{\theta_{(N+1)-i} + \theta_{N-i}}{2} \cdot (x_i - x_{i-1})$$

$$deflection_i := slope_area_i$$

$$deflection_i := deflection_{i-1} + slope_area_i$$

$$\Delta_at_Ultimate := deflection_N \qquad \Delta_at_Ultimate = 26.04 \cdot mm$$

# BIBLIOGRAPHY

Abrishami, A., and Mitchel, D. (March-April 1992), "Uniform Bond Stress," ACI Materials Journel, Vol. 89, No. 2, pp. 161-168.

ASM International (1989), "Composites," Engineering Materials Handbook, Vol 1, Metals Park, OH.

Bresler, B. and Watstein, D. (1974), "Bond and Cracking in Reinforced Concrete," Reinforced Concrete Engineering; Materials, Structural Elements, Safety, Vol 1, Wiley and Sons, New York.

Budelmann, H., Rostasy, F. (1993), "Creep Rupture Behavior of FRP Elements for Prestressed Concrete," International Symposium on FRP Reinforcement for Concrete Structures, ACI SP 138.

Burgoyne, C.J. (1993), "Should FRP be Bonded to Concrete?," International Symposium on FRP Reinforcement for Concrete Structures, ACI SP 138.

Chaallal, O., Benmokrane, B. (1992), "Glass-Fiber Reinforcing Rod: Characterization and Application to Concrete Structures and Grouted Anchors," Materials: Performance and Prevention of Deficiencies and Failures, Proceedings of the Materials Engineering Congress, ASCE, New York, pp. 606-617.

Cook, R. and Young, W. (1989), Advanced Mechanics of Materials, Macmillan Publishing Co., New York, pp. 53.

Daniali, S. (1990), "Bond Strength of Fiber REinforced Plasitc Bars in Concrete,"Serviceability and Durability of Construction Materials, Proceedings of the First Materials Engineering Congress, ASCE, New York, pp. 1182-1191.

Faza, S. and GangaRao, H. (1991), Bending and Bond Behavior and Design of Concrete Beams Reinforced with Fiber Reinforced Plastic Rebars, Doctoral Dissertation, West Virginia University, Morgontown, WV.

Flory, P. (1984), "Molecular Theory of Liquid Crystals," Advances in Polymer Science, Vol 59, Springer-Verlag, pp. 1-36.

Gerritse, A. and Schurhoff, H.(1986), "Aramid Reinforced Concrete," Proceedings of III Rilem Symposium, Developments in Fibre Cement and Concrete, University of Sheffield, U.K.

Gerritse, A. (May 1990), "Applications and Design Criteria for Aramid Fibrous Tensile Elements," Proceedings, Composite Materials in Building: State-of-the-Art, Research, and Prospects, Coonsiglio Nazionale Recerche, Milan, Italy, pp.317-333.

Gerritse, A. and Werner, J. (1991), "ARAPREE, a non-metallic tendon," Advanced Composites Materials in Civil Engineering Structures, Proceedings of the Specialty Conference, ASCE, New York, pp. 143-154.

Herale, J., Lomas, B., Cooke, W., Duerden, I. (1989), Fiber Failure and Wear of Materials: An atlas of fracture, fatigue and durability, Market Cross House, Chichester, England.

Iyer, S., Sen, R., Editors (1991), "Advanced Composites Materials in Civil Engineering Structures", Proceedings of a Specialty Conference, ASCE, New York, pp. 443.

Iyer, S., Khubchandani, A. (1992), "Evaluation of Graphite Composite Cables for Prestressing Concrete," Advanced Composite Materials in Bridges and Structures, 1st International Conference, Canadian Society for Civil Engineering, Canada, pp. 73-78.

Kaci, S. (1992), "Cables Composites pour la Precontrainte: Etude de la Relaxation," Advanced Composite Materials in Bridges and Structures, 1st International Conference, Canadian Society for Civil Engineering, Canada, pp. 89-100.

Kanakubo, T., Yonemaru, K., Fukuyama, H., Fujisawa, M. (1993), "Bond Performance of Concrete Members Reinforced with FRP Bars," International Symposium on FRP Reinforcement for Concrete Structures, ACI SP 138.

Katawaki, K., Nishizaki, I., Sasaki, I. (1992), "Evaluation of the Durability of Advanced Composites for Applications to Prestressed Concrete Bridges," Advanced Composite Materials in Bridges and Structures, 1st International Conference, Canadian Society for Civil Engineering, Canada, pp. 119-127.

Larralde, J., Renbaum L., Morsi, A. (1989), "Fiberglass Reinforced Plastic Rebars in Lieu of Steel Rebars," Proceedings of the Sessions Related to Structural Materials at Structures Congress, ASCE, New York, pp. 261-269.

Larralde, J. and Silva, R. (1990), "Bond Stress-Slip Relationships of FRP Rebars in Concrete," Serviceability and Durability of Construction Materials, Proceedings of the First Materials Engineering Congress, ASCE, New York, pp. 1134-1141.

Makitani, E., Irisawa, I., Nishiura, N. (1993), "Investigation of Bond in Concrete Member with Fiber Reinforced Plastic Bars," International Symposium on FRP Reinforcement for Concrete Structures, ACI SP 138.

Mashima, M. and Iwamoto, K. (1993), "Bond Characteristics of FRP Rod and Concrete after Freezing and Thawing Deterioration," International Symposium on FRP Reinforcement for Concrete Structures, , ACI SP 138.

Mukae, K., Kamagai, S., Nakai, H., Asai, H. (1993), "Characticistics of Aramid FRP Rods," International Symposium on FRP Reinforcement for Concrete Structures, ACI SP 138.

Nanni, A (1992a), "Flexural Behavior and Design Reinforced Concrete Members Using FRP Reinforcement," (in press).

Nanni, A., Matsubara, S., Hasuo, K. (1992b), "Durability of Braided Epoxy-Impregnated Aramid FRP Rods," Advanced Composite Materials in Bridges and Structures, 1st International Conference, Canadian Society for Civil Engineering, Canada, pp. 101-109.

Nanni, A., T. Okamoto, M. Tanigaki, and S. Osakada (1992c), "Tensile Properties of Braided FRP rods for Concrete Reinforcement," Cement and Concrete Composites, (in press).

Nanni A., Utsunomiya, T., Yonekura, H., Tanigaki, M. (May-June 1992d), "Transmission of Prestressing Force to Concrete by Bonded Fiber Reinforced Plastic Tendons," ACI Structural Journal, V. 89, No. 3, pp. 335-344.

Nilson, A. and Winter, G. (1986), Design of Concrete Structures, McGraw-Hill, New York, 10th edition, pp. 65-67.

Noritake, K., Mukae, K., Kumagai, S., Mizutani, J. (1993), "Practical Applications of Aramid FRP Rods to Prestressed Concrete Structures," International Symposium on FRP Reinforcement for Concrete Structures, ACI SP 138.

Pfeifer, D., Landgren, J., Zoob, A. (April 1991), "Protective Systems for New Prestressed and Substructure Concrete," Report FHWA/RD-86/193, U.S. Dept. of Transportation, Washington, D.C., pp. 133.

Pleimann, L. (1991), "Strength, Modulus of Elasticity, and Bond of Deformed FRP Rods," Advanced Composites Materials in Civil Engineering Structures, Proceedings of the Specialty Conference, ASCE, New York, pp. 99-110.

Porter, M. and Barnes, B. (1991), "Tensile Testing of Glass Fiber Composite Rod," Advanced Composites Materials in Civil Engineering Structures, Proceedings of the Specialty Conference, ASCE, New York, pp. 123-131.

Rasheeduzzafar, Dakhil, F., Bader, M., Khan, M. (Sept - Oct 1992), "Performance of Corrosion Resisting Steels in Chloride-Bearing Concrete," ACI Materials Journel, Vol 89, No. 5, pp. 439-448

Reinold de Sitter, W. and Vonk, R. (1993), "Splitting Forces in FRPR Pretensioned Concrete," International Symposium on FRP Reinforcement for Concrete Structures, ACI SP 138.

Rostasy, F.S. (1993), "FRP Tensile Elements for Prestressed Concrete - State of the Art, Potentials and Limits," International Symposium on FRP Reinforcement for Concrete Structures, ACI SP 138.

Saadatmanesh, H. and Ehsani, M. (1989), "Application of Fiber-Composites in Civil Engineering," Proceedings of the Sessions Related to Structural Materials at Structures Congress, ASCE, New York, pp. 526-535.

Sakurada, I. (1985), Polyninyl Alcohol Fibers, Marcel Dekker Inc., New York.

Tanigaki, M. (1991), Flexural Behavior of Concrete Beams Reinforced with High Strength, Doctoral Thesis, Waseda University, Tokyo, pp. 124.

Tao, S., Ehansi, M., Saadatmanesh, H. (1992), "Bond Strength of Straight GFRP Rebars," Materials: Performance and Prevention of Deficiencies and Failures, Proceedings of the Materials Engineering Congress, ASCE, New York, pp. 598-605.

Uomoto, T., Hodhod, H. (1993), "Properties of Fiber Reinforced Plastic Rods for Prestressing Tendons," International Symposium on FRP Reinforcement for Concrete Structures, ACI SP 138.

Yamasaki, Y., Masuda, Y., Tanano, H., Shimizu, A. (1993), "Fundemental Properties of Continuous Fiber Bars," International Symposium on FRP Reinforcement for Concrete Structures, ACI SP 138.